INVERSION OF ELECTROMAGNETIC INDUCTION MEASUREMENTS

Inversion of data from rigid boom single-frequency multi-configuration instruments



Maria Eugenia
CARRIZO MASCARELL

Propositions
accompanying the dissertation
INVERSION OF ELECTROMAGNETIC INDUCTION MEASUREMENTS
Inversion of data from rigid boom single-frequency multi-configuration instruments
by
Maria Eugenia Carrizo Mascarell

1. Using only quadrature data in FDEM inversions is an underutilization of information and should no longer be standard practice. (Chapter 2 of this thesis)

   This proposition pertains to this dissertation

2. Improvements in inversion algorithms cannot compensate for the poorly posed problem of electromagnetic induction inversions. (Chapter 3 of this thesis)

   This proposition pertains to this dissertation

3. In FDEM methods, improving inversion methodologies will be successful only if fast forward modeling of complex subsurface structures becomes the primary research focus. (Chapter 4 of this thesis)

   This proposition pertains to this dissertation

4. Properly trained gradient boosted decision trees algorithms can learn the optimal sensitivity footprint of the combination of measurements from different FDEM coil-coil configurations (Chapter 5 of this thesis)

   This proposition pertains to this dissertation

5. Overemphasizing computational efficiency over geophysical modeling results in biased estimation results.

6. An experiment that exposes flawed assumptions helps scientific progress.

7. Most geophysical instruments are ultimately used for purposes their designers did not anticipate. Therefore, instruments should not be treated as finished products; their design choices must be continually questioned, and improvement should be regarded as an integral part of responsible scientific practice.

8. Geophysical methods will play a decisive role in the global water crisis, but only if the results are communicated in a responsible and transparent manner with their respective uncertainties.

9. Effective preventive health care should be the norm since it saves time, financial resources, and professionals capacity by avoiding or delaying the need for more intensive treatment.

10. The use of European child-protection criteria in indigenous communities is a discriminative action that undermines indigenous parental rights and should be replaced by frameworks developed by native communities.

These propositions are regarded as opposable and defendable, and have been approved as such by the promotor Prof.dr.ir. E.C. Slob and the copromotor Dr. D. Werthmüller.

INVERSION OF ELECTROMAGNETIC INDUCTION MEASUREMENTS

INVERSION OF DATA FROM RIGID BOOM SINGLE-FREQUENCY MULTI-CONFIGURATION INSTRUMENTS

INVERSION OF ELECTROMAGNETIC INDUCTION MEASUREMENTS

INVERSION OF DATA FROM RIGID BOOM SINGLE-FREQUENCY MULTI-CONFIGURATION INSTRUMENTS

Dissertation

for the purpose of obtaining the degree of
doctor at Delft University of Technology,
by the authority of the Rector Magnificus prof. dr. ir. H. Bijl,
chair of the Board for Doctorates,
to be defended publicly on
Friday, September 4th at 12:30

by

Maria Eugenia CARRIZO MASCARELL

This dissertation has been approved by the (co)promotors

Composition of the doctoral committee:

Rector Magnificus	chairperson
Prof. dr. ir. E.C. Slob	Delft University of Technology, *promotor*
Dr. D. Werthmüller	Delft University of Technology / ETH Zurich, *copromotor*
Independent Members:	
Prof. dr. P.J. Vardon	Delft University of Technology
Prof. dr. F.M. Wagner	RWTH Aachen University, Germany
Dr. ir. G.G. Drijkoningen	Delft University of Technology
Dr. P. Rulff	Delft University of Technology
Dr. D.V. Voskov	Delft University of Technology
Prof. dr. H. Hajibeygi	Delft University of Technology, *reserve member*

This project was carried out as part of the WarmingUP Innovation Plan, made possible partially by a subsidy from the Rijksdienst voor Ondernemend Nederland (RVO) in the context of the Meerjarige Missiegedreven Innovatie Programma's (MMIP) subsidy scheme (RVO project number TEUE819001)







Keywords: Electromagnetic induction, electromagnetic modeling, FDEM, EMI, LCI, geophysical inversion, XGBoost

Printed by: ProefschriftMaken

Cover by: Luis J. Puente

Copyright © 2026 by M.E. Carrizo Mascarell

ISBN 978-94-6518-358-9

An electronic version of this dissertation is available at
http://repository.tudelft.nl/.

For Carlos, Carmen, Teresa and Cenia

CONTENTS

Summary 9

Samenvatting 11

1 Introduction 13
- 1.1 Electromagnetic induction . . . 13
- 1.2 Principles of the FDEM method . . . 14
- 1.3 Estimation of electrical conductivity models . . . 16
- 1.4 Thesis objectives . . . 18
- 1.5 Outline . . . 18

2 Exploiting the information in FDEM measurements 25
- 2.1 Introduction . . . 26
- 2.2 Methodology . . . 27
- 2.3 Numerical example . . . 30
- 2.4 Case study: Ackerdijkse Plassen . . . 35
- 2.5 Conclusions . . . 36

3 Estimation of electrical conductivity models 43
- 3.1 Introduction . . . 43
- 3.2 Background . . . 44
- 3.3 Methodology . . . 45
- 3.4 Results and Discussion . . . 47
- 3.5 Conclusions . . . 64

4 Impact of 3D distribution of electrical conductivity 69
- 4.1 Introduction . . . 70
- 4.2 Methodology . . . 71
- 4.3 Error analysis on measurements due to 3D effects . . . 73
- 4.4 Robustness of the Inversion Methods . . . 76
- 4.5 Discussion of results . . . 91
- 4.6 Conclusions . . . 95

5 Predicting 1D models using XGBoost 99
- 5.1 Introduction . . . 100
- 5.2 Methodology . . . 101
- 5.3 Results and discussion . . . 104
- 5.4 Conclusions . . . 111

6 Conclusions and Recommendations **117**
6.1 Conclusions 118
6.2 Recommendations 119
6.3 Future research 120

Acknowledgements **125**

Curriculum Vitæ **131**

List of Publications **133**

SUMMARY

Frequency-domain electromagnetic induction measurements are acquired to understand the distribution of electrical properties in the subsurface. Because the electromagnetic induction method is widely used in geophysical applications to reveal information about the subsurface, the algorithms for converting measurements into electrical conductivity distributions, or other petrophysical parameters are numerous. This geophysical method is widely applied since it is easily deployable and can cover large survey areas in a relatively small amount of time. A wide range of approaches, from simple linear relationships to sophisticated inversion methods, have been used to transform measurements into subsurface parameters. However, many of these methods depend on additional geological or geophysical information to constrain and validate the inversion result.

Near-surface applications of electromagnetic geophysical methods are crucial for society because they provide cost-effective non-invasive ways to investigate the subsurface for water management, natural resources exploration, and environmental hazards. Therefore, the appropriate use and accuracy of the estimations using this measurements is vital for resource assessment, effective hazard mitigation, and reliable engineering projects by providing a precise understanding of subsurface conditions. In general, this geophysical method has been studied exhaustively, but is still challenging to understand the uncertainties associated.

This thesis presents a comprehensive study of inversion methodologies for frequency-domain electromagnetic induction surveys, addressing both computational efficiency and model reliability. We start by studying the sensitivity of the measurements to the electrical conductivity of the subsurface. We analyze the impact of using linear approximations and compare them to a global search strategy using precomputed lookup tables of semi-analytic forward responses. The global search method enables rapid electrical conductivity model estimation, without iterative forward modeling. This approach is validated with synthetic and field datasets, demonstrating fast convergence and reliable recovery of horizontally 2-layered earth models. Furthermore, the study demonstrates the added value of using both quadrature and in-phase components of the measurements. Numerical experiments demonstrate that incorporating the in-phase response enhances sensitivity to conductivity and, as a result, improves result accuracy compared with quadrature-only inversions, providing new insights into subsurface structure.

Moreover, this thesis investigates the well-posedness of frequency-domain electromagnetic induction data inversion. This analysis demonstrates that the uniqueness of one-dimensional subsurface models with two layers is ensured only when both quadrature and in-phase measurements are incorporated, for multi-coil single frequency configurations. On the contrary, for three-layer models the solution remains underdetermined without additional prior constraints. These findings highlight the fundamental limits of the inversion problem and the importance of exploiting the full information

contained in the data.

Additionally, the limitations of piecewise inversion (subdividing the subsurface into one-dimensional datasets) and laterally constrained inversion are assessed under realistic three-dimensional conditions. Simulations reveal that lateral conductivity variations, topographic effects, and instrument tilt introduce significant distortions, even for small deviations from ideal assumptions. Numerical examples and field applications demonstrate that, while laterally constrained inversion provides smoother results than piecewise inversion, both methods remain vulnerable to error propagation in complex environments.

Finally, this thesis proposes a novel approach based on machine learning inversion via gradient boosted decision trees to estimate layered subsurface electrical conductivity distributions from the measurements. This prediction algorithm provides three clear advantages: Firstly, the ability of the decision trees to provide individual influence weights to different measurement parameters allows for a better understanding of the sensitivity of the individual data values to the subsurface properties. Secondly, this machine learning algorithm learns the physical system's non-linearity by understanding how the different data parameters interact. Finally, predictions from the electrical conductivity model are generated without prior knowledge of the subsurface. Compared to optimization-based estimations, the machine learning resulting predictions more closely match the true models.

Together, these contributions advance the knowledge about the inversion of electromagnetic induction measurements by evaluating estimation methodologies, analyzing data utilization, and critically evaluating their application into electrical conductivity distribution of the subsurface. The results emphasize both the potential and the limitations of current inversion strategies, and they motivate the development of forward modelling and inversion methodologies for realistic frequency-domain electromagnetic induction survey conditions. The main contribution of this study is an easily applicable machine learning estimation method without additional information of the subsurface.

SAMENVATTING

Metingen van elektromagnetische inductie in het frequentie-domein worden uitgevoerd om de verdeling van elektrische eigenschappen in de ondergrond te begrijpen. Omdat de elektromagnetische inductie methode veelvuldig wordt gebruikt in geofysische toepassingen om informatie over de ondergrond te onthullen, bestaan er talloze algoritmen voor het omzetten van metingen in elektrische geleidbaarheidsverdelingen of andere petrofysische parameters. Deze geofysische methode wordt veel toegepast omdat deze eenvoudig inzetbaar is en grote onderzoeksgebieden in relatief korte tijd kan bestrijken. Een breed scala aan benaderingen, van eenvoudige lineaire verbanden tot geavanceerde inversiemethoden, is gebruikt om metingen om te zetten in ondergrondse parameters. Veel van deze methoden zijn echter afhankelijk van aanvullende geologische of geofysische informatie om het inversieresultaat te beperken en te valideren.

Toepassingen van elektromagnetische geofysische methoden in de nabije ondergrond zijn cruciaal voor de samenleving, omdat ze kosteneffectieve, niet-invasieve manieren bieden om de ondergrond te onderzoeken voor waterbeheer, exploratie van natuurlijke hulpbronnen en milieugevaren.

Daarom is het juiste gebruik en de nauwkeurigheid van de schattingen met behulp van deze metingen van vitaal belang voor de beoordeling van hulpbronnen, effectieve risicobeperking en betrouwbare technische projecten, door een nauwkeurig inzicht te verschaffen in de omstandigheden in de ondergrond. Over het algemeen is deze geofysische methode uitvoerig bestudeerd, maar het blijft een uitdaging om de bijbehorende onzekerheden te begrijpen.

Deze thesis presenteert een uitgebreide studie van inversiemethoden voor elektromagnetische inductiemetingen in het frequentie-domein, waarbij zowel de computationele efficiëntie als de modelbetrouwbaarheid aan bod komen. We beginnen met het bestuderen van de gevoeligheid van de metingen voor de elektrische geleidbaarheid van de ondergrond. We analyseren de impact van het gebruik van lineaire benaderingen en vergelijken deze met een globale zoekstrategie met behulp van vooraf berekende opzoektabelen van semi-analytische voorwaartse responsen. De globale zoekmethode maakt een snelle schatting van het elektrische geleidbaarheidsmodel mogelijk, zonder iteratieve voorwaartse modellering. Deze aanpak wordt gevalideerd met synthetische en veldgegevens, waarbij een snelle convergentie en betrouwbare reconstructie van horizontaal 2-laags aardmodellen wordt aangetoond. Bovendien toont de studie de toegevoegde waarde aan van het gebruik van zowel kwadratuur- als in-fasecomponenten van de metingen.

Numerieke experimenten tonen aan dat het incorporeren van de in-faserespons de gevoeligheid voor geleidbaarheid vergroot en daardoor de nauwkeurigheid van de resultaten verbetert in vergelijking met inversies die alleen gebruikmaken van kwadratuur, wat nieuwe inzichten oplevert in de structuur van de ondergrond.

Verder onderzoekt dit proefschrift de welgedefinieerdheid van frequentie-domein elektromagnetische inductie data inversie. Deze analyse toont aan dat de uniciteit van eendimensionale ondergrondmodellen met twee lagen alleen gegarandeerd is wanneer zowel kwadratuur- als in-fasemetingen worden opgenomen, voor configuraties met meerdere spoelen en één frequentie. Integendeel, voor drielaagse modellen blijft de oplossing onderbepaald zonder aanvullende voorafgaande beperkingen. Deze bevindingen benadrukken de fundamentele beperkingen van het inversieprobleem en het belang van het benutten van alle informatie in de data.

Daarnaast worden de beperkingen van stuksgewijze inversie (het onderverdelen van de ondergrond in eendimensionale datasets) en lateraal beperkte inversie beoordeeld onder realistische driedimensionale omstandigheden. Simulaties laten zien dat laterale geleidbaarheidsvariaties, topografische effecten en instrumenthelling aanzienlijke vertekeningen introduceren, zelfs bij kleine afwijkingen van ideale aannames. Numerieke voorbeelden en veldtoepassingen tonen aan dat, hoewel lateraal beperkte inversie vloeiendere resultaten oplevert dan stuksgewijze inversie, beide methoden kwetsbaar blijven voor foutpropagatie in complexe omgevingen.

Ten slotte stelt dit proefschrift een nieuwe benadering voor, gebaseerd op machine learning-inversie via gradient boosted decision trees, om gelaagde elektrische geleidbaarheidsverdelingen in de ondergrond te schatten op basis van de metingen. Dit voorspellingsalgoritme biedt drie duidelijke voordelen: Ten eerste maakt de mogelijkheid van beslissingsbomen om individuele invloedsgewichten toe te kennen aan verschillende meetparameters een beter begrip mogelijk van de gevoeligheid van de individuele datawaarden voor de eigenschappen van de ondergrond. Ten tweede leert dit machine learning-algoritme de niet-lineariteit van het fysieke systeem door te begrijpen hoe de verschillende dataparameters op elkaar inwerken. Ten slotte worden voorspellingen op basis van het elektrische geleidbaarheidsmodel gegenereerd zonder voorafgaande kennis van de ondergrond. In vergelijking met op optimalisatie gebaseerde schattingen komen de voorspellingen van machine learning beter overeen met de werkelijke modellen.

Samen bevorderen deze bijdragen de kennis over de inversie van elektromagnetische inductiemetingen door schattingsmethoden te evalueren, datagebruik te analyseren en de toepassing ervan op de elektrische geleidbaarheidsverdeling van de ondergrond kritisch te beoordelen. De resultaten benadrukken zowel de mogelijkheden als de beperkingen van de huidige inversiestrategieën en stimuleren de ontwikkeling van voorwaartse modellering en inversiemethoden voor realistische elektromagnetische inductiemetingen in het frequentiedomein. De belangrijkste bijdrage van deze studie is een eenvoudig toepasbare machine learning-schattingsmethode die geen aanvullende informatie over de ondergrond vereist.

1

INTRODUCTION

Nothing is too wonderful to be true,
if it be consistent with the laws of nature.

Michael Faraday

1.1. ELECTROMAGNETIC INDUCTION

Electromagnetic induction (EMI) is a geophysical method used to map physical properties of the subsurface, in which a voltage difference is measured between the terminals of a loop antenna that is connected to a receiver unit. In the EMI instrument, the electrical signal frequencies are low enough that the source-receiver offset is less than the free-space wavelength, called quasi-static range (Nabighian and Corbett, 1991). In this case, the voltage difference can be understood as an electric field. These voltage difference measurements are used to infer the distribution of the electrical conductivity of the Earth. Numerous EMI methods exist, depending on the transmitter-receiver configurations (e.g., ground-based, drone-based, airborne) and the signal type (e.g., time domain [TDEM], frequency domain [FDEM], very low frequency [VLF]). In EMI soundings, a loop source generates the electromagnetic field.

The principles underlying the EMI geophysical method date back to the discovery of electromagnetic induction by Michael Faraday in 1831. Faraday's Law states that a changing magnetic field induces an electric current in a nearby conductor. In the late 19th century, James Clerk Maxwell formalized the equations governing electromagnetic fields, paving the way for practical applications (Nabighian and Corbett, 1991). Early applications of EMI were largely confined to electrical engineering and communications, but geophysicists soon recognized its potential for subsurface exploration. The first systematic application of electromagnetic induction for geophysical exploration began in the 1920s and 1930s, particularly for mineral prospecting (Blau, 1933; Eklund et al., 1923).

Since then, EMI soundings have been used for exploration of resources such as oil and gas (Davydycheva, 2010; Kaufman and Itskovich, 2017; Sainson, 2017), groundwater

(Goldstein et al., 1990; McNeill et al., 1990; Mitsuhata et al., 2006), geothermal energy (Berktold, 1983; Martinez-Garcia, 1992), and minerals (Duckworth, 1970; Eadie, 1987; Witherly, 2000). Other applications are Earth's crust studies, lithology mapping, hazardous waste investigation, and many more.

This thesis focuses on the frequency domain electromagnetic induction method with a loop-loop configuration (abbreviated as FDEM). This method was initially developed by Sture Werner and Alfred Holm, who contributed with the creation of the first instrument in 1936 and the Slingram method, a precursor to modern loop-loop FDEM techniques (Påsse and Kim-Andersson, 1948). After World War II, technological advancements led to more sophisticated FDEM instruments and increased interest in electromagnetic methods for various geophysical applications (Howell, 1966; Musson, 1968). The 1970s and 1980s saw significant improvements in FDEM instrumentation and a broader range of applications, such as multi-frequency and multi-coil configurations. Furthermore, the development of digital signal processing enabled better noise reduction, data acquisition and interpretation (Lytle, 1979; McNeill, 1980, 1983a, 1983b; Smith and West, 1987; Tabbagh, 1986). Likewise, developments in inversion algorithms allowed geophysicists to obtain more accurate subsurface conductivity maps. By the 1990s, commercial FDEM instruments such as the Geonics EM31, EM34, and EM38 became industry standards for near-surface geophysics, particularly in environmental and agricultural studies (Cook and Walker, 1992; Hendrickx et al., 1992; Sheets and Hendrickx, 1995).

Advancements in computational power and machine learning contributed in the evolution of FDEM as an essential tool in geophysics. By integrating other geophysical methods, such as Ground Penetrating Radar (GPR), Magnetotellurics (MT), and Time-Domain Electromagnetic (TDEM) surveys, current geophysical applications offer a more comprehensive understanding of subsurface conditions. Currently, the emergence of UAV-mounted (drone-based) FDEM systems has expanded their use in rapid and cost-effective geophysical surveys over large areas.

1.2. PRINCIPLES OF THE FDEM METHOD

The governing laws that relate the electromagnetic fields to physical properties in the FDEM method are described by Maxwell's equations (Nabighian and Corbett, 1991; West and Macnae, 2012). According to Faraday's law, when a time-varying magnetic field is applied in the vicinity of a conductor, an electric current is generated within the conductor itself. The mathematical formulation can be expressed as:

$$\nabla \times \mathbf{E} = -\frac{\partial \mathbf{B}}{\partial t} - \mathbf{J}_m, \tag{1.1}$$

where $\mathbf{E}$ represents the electric field, $\mathbf{B}$ is the magnetic flux and $\mathbf{J}_m$ the magnetic current density of the source.

Ampere's law states that to every time-varying electric field, a magnetic field is associated, expressed by:

$$\nabla \times \mathbf{H} = \frac{\partial \mathbf{D}}{\partial t} + \mathbf{J}_e, \tag{1.2}$$

where $\mathbf{H}$ represents the magnetic field, $\mathbf{J}_e$ is the electric current density, and $\mathbf{D}$ is the elec-

tric displacement. These vectors **E**, **D**, **B**, **H** and $\mathbf{J}_e$ are linked by the following relations:

$$\mathbf{D} = \epsilon \mathbf{E}, \tag{1.3}$$

$$\mathbf{B} = \mu \mathbf{H}, \tag{1.4}$$

$$\mathbf{J}_e = \sigma \mathbf{E}, \tag{1.5}$$

where ϵ is the dielectric constant (F/m), μ is the magnetic permeability (H/m) and σ is the electric conductivity (S/m), which are physical properties of the air, water and Earth's subsurface or materials within it.

Through temporal Fourier transformations of Maxwell's equations, we can obtain a set of two equations describing the propagation of the electric and the magnetic field in a source-free, homogeneous and isotropic medium whose physical properties are given by ϵ, μ and σ as follows:

$$\nabla^2 \mathbf{E} = (i\omega\mu\sigma - \epsilon\mu\omega^2)\mathbf{E}, \tag{1.6}$$

$$\nabla^2 \mathbf{H} = (i\omega\mu\sigma - \epsilon\mu\omega^2)\mathbf{H}, \tag{1.7}$$

where ω is the angular frequency. In equations 1.6 and 1.7, the term $i\omega\mu\epsilon$ relates to the so-called conduction currents, while the term $\epsilon\mu\omega^2$ relates with the so-called displacement currents. When $\sigma \gg \omega\epsilon$ (generally at frequencies lower than 10 kHz), conduction currents prevail with respect to the displacement currents; this is known as the diffusive regime. When the frequency of the instrument signal is higher than 10 MHz, displacement currents dominate with respect to the conductive currents, and this is known as the radar regime (Nabighian and Corbett, 1991).

The FDEM method is based on a loop-loop electromagnetic inductive instrument, where a time-harmonic electric current of intensity I^{p} flows in the transmitter coil T_x usually laid out on the ground or in the air above it (Deidda et al., 2022). The current generates a time-harmonic primary magnetic field $\mathbf{H}^{\mathrm{p}}$ that spreads in all directions. Part of the magnetic field directly arrives to the receiver coil R_x located at a distance s from the transmitter coil, generating a voltage in the receiver coil that is then measured.

Simultaneously, the primary electromagnetic field travels through the subsurface, inducing electric currents (eddy currents). Then, according to Ampere's law, a secondary magnetic field $\mathbf{H}^{\mathrm{s}}$ is generated due to the eddy currents. This secondary electromagnetic field will also flow through the receiver coil and will have a phase difference with respect to the primary. The secondary magnetic field generated by the conductive materials in the subsurface is much smaller than the primary magnetic field ($\|\mathbf{H}^{\mathrm{s}}\| \ll \|\mathbf{H}^{\mathrm{p}}\|$). The primary field $\mathbf{H}^{\mathrm{p}}$ is known, as it depends solely on the instrument's geometrical configuration, and the secondary response will include information about the electromagnetic field and the subsurface properties (Everett, 2013).

The primary and secondary magnetic field intensities ($\mathbf{H}^{\mathrm{p}}$ and $\mathbf{H}^{\mathrm{s}}$) are complex values. The primary magnetic field is time-harmonic varying ($\mathbf{H}^{\mathrm{p}} \sin(\omega t)$). Therefore, using the identity:

$$\sin(\omega t + \varphi) = \sin(\omega t)\cos(\varphi) + \cos(\omega t)\sin(\varphi), \tag{1.8}$$

we can decompose the total magnetic field passing through the receiver coil $\mathbf{H}^{\mathrm{T}}$ into two

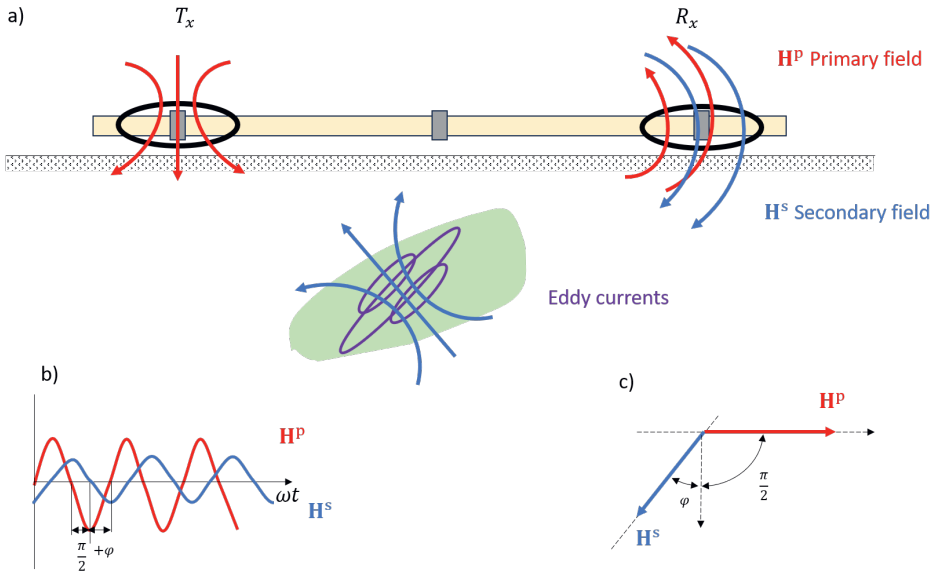


Figure 1.1: a) Schematic representation of a rigid-boom frequency-domain electromagnetic (FDEM) device. b) Time dependence of primary and secondary fields. c) Phasor diagram with the primary current as reference, showing the phase lag of the secondary magnetic field with respect to the primary field. (modified from Grant and West, 1966)

components,

$$\mathbf{H}^T = \mathbf{H}^p \sin(\omega t) + \mathbf{H}^s \sin(\omega t + \varphi), \tag{1.9}$$

$$= \mathbf{H}^p \sin(\omega t) + \mathbf{H}^s \sin(\omega t)\cos(\varphi) + \mathbf{H}^s \cos(\omega t)\sin(\varphi), \tag{1.10}$$

$$= [\mathbf{H}^p + \mathbf{H}^s \cos(\varphi)]\sin(\omega t) + [\mathbf{H}^s \sin(\varphi)]\cos(\omega t), \tag{1.11}$$

such that $\mathbf{P} = \mathbf{H}^p + \mathbf{H}^s \cos(\varphi)$ is termed the *in-phase* response component (also known as the real component) and $\mathbf{Q} = \mathbf{H}^s \sin(\varphi)$ is termed the *quadrature* response component (also known as the imaginary component). These components are obtained from the measurements of the FDEM instrument. Traditionally, the *quadrature* component is used to infer information about the bulk electrical conductivity of the subsurface, also called apparent electrical conductivity σ_a (McNeill, 1980).

1.3. ESTIMATION OF ELECTRICAL CONDUCTIVITY MODELS

The FDEM method is commonly applied for shallow subsurface estimations. It has been used in numerous fields, including environmental monitoring, agriculture, archaeology, groundwater studies, and mineral exploration (e.g., Section 1.1).

Initially, the FDEM method was implemented by mapping the apparent electrical conductivity σ_a over an area. The changes in electrical properties between two subsurface materials were interpreted to detect targets, such as contaminants, moisture or salinity changes (e.g., Ferguson et al., 1996; Sam and Ridd, 1998).

In recent years, more sophisticated methods that determine the 1D, 2D, or 3D subsurface distribution of the electrical conductivity or other physical properties (salinity, clay content, soil moisture, etc.) derived from petrophysical models have been presented (e.g., Delefortrie et al., 2014; Delrue et al., 2020; Guillemoteau et al., 2017, 2019; Monteiro Santos et al., 2011; Zhang et al., 2021).

Like many other geophysical inverse problems, FDEM data inversion is typically ill-posed, due to non-uniqueness or unstability of the solution (Tikhonov et al., 1977). Usually, the inversion methods applied to FDEM measurements implement optimization schemes to obtain subsurface models. To handle the ill-posedness of the inverse problem, a stabilizing term (or regularization term) is introduced in the objective functional to be minimized as prior information (Constable et al., 1987). However, this approach holds two possible challenges: 1) the assumption of prior information about the subsurface, and 2) the result could depend on the chosen initial model.

The FDEM presents several advantages over other geophysical electrical methods that encourage us to investigate the inversion of these measurements. Some of these advantages are:

- FDEM is an inductive method, therefore, it is not affected by current injection problems in resistive areas encountered in other geoelectric geophysical methods (McNeill, 1980).

- FDEM methods are non-invasive, they do not require direct contact with the ground.

- In the FDEM method, physical contact with the ground is not necessary. The instrument is just placed above the area to be measured. This allows for flexibility and easier movement above the surface. For this reason, the data collection is done in a fast manner compared with other geoelectric measurements. This decreases acquisition costs.

On the other hand, the FDEM method also has disadvantages that affect an accurate estimation of the electrical conductivity distribution:

- A major drawback of many FDEM surveys is that the measured bulk electrical conductivity σ_a values are affected by systematic measurement errors, for which correction procedures might be necessary (Binley et al., 2015).

- Several factors, such as solar flares, humidity, and temperature changes, in addition to the proximity of metallic objects or instruments with wireless communication too close to the FDEM system, can distort the measurements (Delefortrie et al., 2014; Gebbers et al., 2009; von Hebel et al., 2019).

- The vertical sounding capability is limited by the loop-loop offset and set frequencies when these are fixed.

To address these challenges, we aim to study the accuracy of the inversion methodologies, their assumptions, and limitations.

1

1.4. THESIS OBJECTIVES

The FDEM geophysical method holds promise as a tool for investigating the shallow subsurface. We are motivated to better understand the information in the measurements and obtain accurate estimations from them. In this thesis, we investigate the impact of the following approaches on a reliable and accurate estimation of electrical conductivity models of the subsurface:

- The low induction number (LIN) approximation.
- Using an optimization inversion scheme.
- Assuming flat topography and horizontal position of the instrument.
- Horizontally isotropic, homogeneous layered Earth assumption.
- Using machine learning algorithms.

FDEM acquisition can contain a large amount of measurements; on average, a measurement is taken every 0.2 m, but it can vary greatly. To obtain electrical conductivity estimations at each measurement position, some methodologies perform iteratively forward modeling until obtaining a minimal data misfit, which can make the estimations computationally expensive for real-time applications. The approaches and assumptions mentioned above are used for computing efficiency and simplification purposes. Our aim is to study the consequences of these simplifications on the accuracy of the estimated models. Moreover, we plan to design an inversion strategy that balances the computational effort with the accuracy of the estimation.

The contributions and objectives of this thesis are summarized in the following list:

- The analysis of the contribution of the *quadrature* and *in-phase* components of the FDEM measurements with respect to distribution of electrical conductivity.
- The detailed study of the well-posedness of the inversion problem for 2- and 3-layered subsurface models.
- Studying the impact of 3D variations of the earth into the FDEM measurements and the propagation of this effect into the inversion methods when assuming a horizontally earth.
- Developing a method for estimating electrical conductivity models of the subsurface using FDEM measurements using machine learning algorithms.

1.5. OUTLINE

This thesis focuses on investigating the impact of the assumptions made to solve the FDEM inversion problem and developing a computationally efficient, accurate and reliable inversion methodology.

We dedicate Chapter 2 to demonstrate, using a global search inversion approach, that both *quadrature* and *in-phase* measurement components are sensitive to the electrical conductivity of the subsurface, using 1D horizontally layered earth models. Additionally, we compare the impact of two different forward functions into the inversion

scheme: the low induction number (LIN) approximation forward function and the semi-analytical forward function. We show how the use of different forward functions impact on the estimations with both numerical examples and a field case example.

In Chapter 3 we analyze the uniqueness and stability of the inversion problem for 1D horizontally layered earth models. For this, we show with numerical examples that the inversion problem seems to be unique for 2-layered earth models when using both *quadrature* and *in-phase* measurements. However, the inversion problem is affected by stability issues even for a simple 2-layered case, meaning that it is still ill-posed. Moreover, we find results that suggest the problem is non-unique for 3-layered earth models. The inversion methodology is further demonstrated with field data.

Afterwards, in Chapter 4 we present the effect of 2.5D and 3D conductivity distributions, including topographic variations and instrument pitch angle on the FDEM measurements. In order to do this we examine how these measurement distortions propagate into two inversion strategies, the Piecewise 1D (PWI) and the Laterally Constrained Inversion (LCI) in different 2D and 3D electrical conductivity distributions. We show that the FDEM measurements are highly sensitive to topography or tilt of the instrument, which amplifies the limitations of using this geophysical method to obtain accurate electrical conductivity information of the subsurface.

In Chapter 5 a simple and practical methodology is applied to train a machine learning algorithm to predict 1D electrical conductivity distributions without prior information of the subsurface. This is done by training, testing and valuidating an XGBoost decision tree algorithm with synthetic FDEM measurements. We analyse the prediction power of the algorithm with numerical examples and show the advantages with respect to the classical optimization approach.

Finally, Chapter 6 summarises the main conclusions based on the results obtained in the previous chapters. Additionally, recommendations for future research are made, which can help further develop the ideas and methodologies proposed in this thesis.

BIBLIOGRAPHY

Berktold, A. (1983). Electromagnetic studies in geothermal regions. *Geophysical surveys*, *6*(1), 173–200. https://doi.org/10.1007/BF01454000

Binley, A., Hubbard, S. S., Huisman, J. A., Revil, A., Robinson, D. A., Singha, K., & Slater, L. D. (2015). The emergence of hydrogeophysics for improved understanding of subsurface processes over multiple scales. *Water Resources Research*, *51*(6), 3837–3866. https://doi.org/10.1002/2015WR017016

Blau, L. W. (1933). *Method and apparatus for geophysical exploration* (US1911137A).

Constable, S., Parker, R., & Constable, C. (1987). Occam's inversion: A practical algorithm for generating smooth models from electromagnetic sounding data. *Geophysics*, *52*(3), 289–300. https://doi.org/10.1190/1.1442303

Cook, P. G., & Walker, G. R. (1992). Depth profiles of electrical conductivity from linear combinations of electromagnetic induction measurements. *Soil Science Society of America Journal*, *56*(4), 1015–1022. https://doi.org/10.2136/sssaj1992.03615995005600040003x

Davydycheva, S. (2010). 3D modeling of new-generation (1999–2010) resistivity logging tools. *The Leading Edge*, *29*(7), 780–789. https://doi.org/10.1190/1.3462778

Deidda, G. P., Carlo, L. D., Caputo, M. C., & Cassiani, G. (2022). Frequency domain electromagnetic induction imaging: An effective method to see inside a capped landfill. *Waste Management*, *144*, 29–40. https://doi.org/10.1016/j.wasman.2022.03.007.

Delefortrie, S., Saey, T., Van De Vijver, E., De Smedt, P., Missiaen, T., Demerre, I., & Van Meirvenne, M. (2014). Frequency domain electromagnetic induction survey in the intertidal zone: Limitations of low-induction-number and depth of exploration. *Journal of Applied Geophysics*, *100*, 14–22. https://doi.org/10.1016/j.jappgeo.2013.10.005

Delrue, S., Maveau, B., & Dudal, D. (2020). A damped forward EMI model for a horizontally stratified earth. *Exploration Geophysics*, *51*(4), 422–433. https://doi.org/10.1080/08123985.2019.1708717

Duckworth, K. (1970). Electromagnetic depth sounding applied to mining problems. *Geophysics*, *35*(6), 1086–1098. https://doi.org/10.1190/1.1440145

Eadie, T. (1987). The downhole EM response of the Hellyer ore deposit. *Exploration Geophysics*, *18*(3), 255–264. https://doi.org/10.1071/EG987255

Eklund, J., Sundberg, K., & Lundberg, H. (1923). Electrical prospecting in Sweden. *Sveriges GeologiskaUndersökning*, *17*. https://api.semanticscholar.org/CorpusID:127181596

Everett, M. E. (2013). Electromagnetic induction. In *Near-surface applied geophysics* (pp. 200–238). Cambridge University Press. https://doi.org/https://doi.org/10.1017/CBO9781139088435.009

Ferguson, I. J., Taylor, W. J., & Schmigel, K. (1996). Electromagnetic mapping of saline contamination at an active brine pit. *Canadian Geotechnical Journal*, *33*(2), 309–323. https://doi.org/10.1139/t96-009

Gebbers, R., Lück, E., Dabas, M., & Domsch, H. (2009). Comparison of instruments for geoelectrical soil mapping at the field scale. *Near Surface Geophysics*, *7*(3), 179–190. https://doi.org/10.3997/1873-0604.2009011

Goldstein, N. E., Benson, S. M., & Alumbaugh, D. (1990). Saline groundwater plume mapping with electromagnetics. *Geotechnical and environmental geophysics*, *2*, 17–25. https://doi.org/10.1190/1.9781560802785.2.ch2

Grant, F. S., & West, G. F. (1966). Interpretation theory in applied geophysics. *Geological Magazine*, *103*(2), 184–184. https://doi.org/10.1017/S0016756800050627

Guillemoteau, J., Christensen, N. B., Jacobsen, B. H., & Tronicke, J. (2017). Fast 3D multichannel deconvolution of electromagnetic induction loop-loop apparent conductivity data sets acquired at low induction numbers. *Geophysics*, *82*(6), E357–E369. https://doi.org/10.1190/geo2016-0518.1

Guillemoteau, J., Simon, F.-X., Hulin, G., Dousteyssier, B., Dacko, M., & Tronicke, J. (2019). 3-D imaging of subsurface magnetic permeability/susceptibility with portable frequency domain electromagnetic sensors for near surface exploration. *Geophysical Journal International*, *219*(3), 1773–1785. https://doi.org/10.1093/gji/ggz382

Hendrickx, J. M. H., Baerends, B., Raza, Z. I., Sadig, M., & Chaudhry, M. A. (1992). Soil salinity assessment by electromagnetic induction of irrigated land. *Soil Science Society of America Journal*, *56*(6), 1933–1941. https://doi.org/10.2136/sssaj1992.03615995005600060047x

Howell, M. (1966). A soil conductivity meter. *Archaeometry*, *9*(1), 20–23. https://doi.org/10.1111/j.1475-4754.1966.tb00902.x

Kaufman, A., & Itskovich, G. (2017). Induction logging based on transient em measurements. In A. Kaufman & G. Itskovich (Eds.), *Basic principles of induction logging* (pp. 311–383). Elsevier. https://doi.org/10.1016/B978-0-12-802583-3.00010-1

Lytle, R. (1979). Properties of the ground inferred from electromagnetic measurements. *IEEE Transactions on Antennas and Propagation*, *27*(6), 899–902. https://doi.org/10.1109/TAP.1979.1142208

Martinez-Garcia, M. (1992). Electromagnetic induction in geothermal fields and volcanic belts. *Surveys in Geophysics*, *13*(4), 409–434. https://doi.org/10.1007/BF01903485

McNeill, J. D., et al. (1990). Use of electromagnetic methods for groundwater studies. *Geotechnical and environmental geophysics*, *1*(5), 191–218. https://doi.org/10.1190/1.9781560802785.ch7

McNeill, J. D. (1980). *Electromagnetic terrain conductivity measurement at low induction numbers* (tech. rep.). Geonics Limited. ON, Canada. https://geonics.com/pdfs/technicalnotes/tn6.pdf

McNeill, J. D. (1983a). EM34-3 survey interpretation techniques. https://geonics.com/pdfs/technicalnotes/tn8.pdf

McNeill, J. D. (1983b). Use of EM31 inphase information. https://geonics.com/pdfs/technicalnotes/tn11.pdf

Mitsuhata, Y., Uchida, T., Matsuo, K., Marui, A., & Kusunose, K. (2006). Various-scale electromagnetic investigations of high-salinity zones in a coastal plain. *Geophysics*, *71*(6), B167–B173. https://doi.org/10.1190/1.2335658

Monteiro Santos, F. A., Triantafilis, J., & Bruzgulis, K. (2011). A spatially constrained 1D inversion algorithm for quasi-3D conductivity imaging: Application to DUALEM-421 data collected in a riverine plain. *Geophysics*, *76*(2), B43–B53. https://doi.org/10.1190/1.3537834

Musson, C. R. (1968). A geophysical survey at South Cadbury Castle, Somerset, using the howell soil conductivity anomaly detector. *Prosp. Archeol.*, *3*, 115–121.

Nabighian, M. N., & Corbett, J. D. (1991). *Electromagnetic Methods in Applied Geophysics - Applications - Part A and Part B, Volume 2*. Society of Exploration Geophysicists (SEG). https://app.knovel.com/hotlink/toc/id:kpPV1HI9Z3/electromagnetic-methods/electromagnetic-methods

Påsse, T., & Kim-Andersson, A. (1948). Sveriges geologiska undersökning : 150 år i samhällets tjänst : Undersökningen, uppdragen, människorna.

Sainson, S. (2017). Principles and methods. In *Electromagnetic seabed logging: A new tool for geoscientists* (pp. 51–129). Springer International Publishing. https://doi.org/10.1007/978-3-319-45355-2_2

Sam, R., & Ridd, P. (1998). Spatial variations of groundwater salinity in a mangrove-salt flat system, Cocoa Creek, Australia. *Mangroves and Salt Marshes*, *2*(3), 121–132. https://doi.org/10.1023/A:1009919411508

Sheets, K. R., & Hendrickx, J. M. H. (1995). Noninvasive soil water content measurement using electromagnetic induction. *Water Resources Research*, *31*(10), 2401–2409. https://doi.org/10.1029/95WR01949

Smith, R. S., & West, G. F. (1987). Electromagnetic induction in an inhomogeneous conductive thin sheet. *Geophysics*, *52*(12), 1677–1688. https://doi.org/10.1190/1.1442284

Tabbagh, A. (1986). Applications and advantages of the Slingram electromagnetic method for archaeological prospecting. *Geophysics*, *51*(3), 576–584. https://doi.org/10.1190/1.1442112

Tikhonov, A. N., Arsenin, V. J., & John, F. (1977). *Solutions of ill-posed problems* [Section: xiii, 258 p. : ill. ; 23 cm.]. V.H. Winston ; Wiley.

von Hebel, van der Kruk, Huisman, Mester, Altdorff, Endres, Zimmermann, Garré, & Vereecken. (2019). Calibration, Conversion, and Quantitative Multi-Layer Inversion of Multi-Coil Rigid-Boom Electromagnetic Induction Data. *Sensors*, *19*(21), 4753. https://doi.org/10.3390/s19214753

West, G. F., & Macnae, J. C. (2012). Physics of the Electromagnetic Induction Exploration Method. In *Electromagnetic methods in applied geophysics: Volume 2, Application, Parts A and B* (pp. 5–46). Society of Exploration Geophysicists (SEG). https://doi.org/10.1190/1.9781560802686.ch1

Witherly, K. (2000). The quest for the Holy Grail in mining geophysics: A review of the development and application of airborne EM systems over the last 50 years. *The Leading Edge*, *19*(3), 270–274. https://doi.org/10.1190/1.1438586

Zhang, B., Yin, C., Liu, Y., Ren, X., Baranwal, V. C., & Xiong, B. (2021). 3D Inversion of large-scale frequency-domain airborne electromagnetic data using unstructured lo-

cal mesh. *Geophysics*, *86*(5), E333–E342. https://doi.org/10.1190/geo2020-0243.1

2

EXPLOITING THE INFORMATION IN FDEM MEASUREMENTS

It's easy to play any musical instrument:
all you have to do is touch the right key at the right time
and the instrument will play itself.

Johann Sebastian Bach

Rigid boom electromagnetic surveys that use loop-loop configurations are often used to obtain information about the subsurface conductivity. Semi-analytic solutions help to simulate electromagnetic induction measurements for a large number of horizontally layered models, which can then be stored and used as a lookup table. This procedure is performed once and then used to find the corresponding model that produces the best data fit, eliminating the need to run numerous simulations in every minimization step of an inversion scheme for large field datasets. We apply this methodology to a numerical example and field data acquired in The Netherlands. Our results from both cases using the global search demonstrate its ability to estimate electrical conductivity distributions in two-layered models in a fast and accurate manner. Furthermore, we apply the workflow using a lookup table based on low induction number approximation-derived measurements. The outcome of implementing this methodology using the low induction number lookup table shows poor accuracy in the electrical conductivity estimations for both the numerical example and the field data in comparison to the semi-analytical approach.

Part of this chapter was published as M. Carrizo Mascarell, D. Werthmüller, and E. Slob, *Global search inversion for electromagnetic induction data using layered models*, NSG2023 29th European Meeting of Environmental and Engineering Geophysics **2023**. Minor modifications have been applied to the text and figures for thesis consistency.

2.1. INTRODUCTION

FDEM instruments are commonly used to estimate the electrical conductivity of the shallow subsurface for hydrogeological, environmental, agricultural, and archeological purposes. McNeill (1980) proposed a way to linearly derive an approximated value of the apparent electrical conductivity σ_a of a horizontally layered subsurface from FDEM measurements, which is called the low induction number (LIN) approximation. This methodology assumes two main conditions: 1) the low induction number (LIN) condition $\beta \ll 1$, where the induction number is defined as $\beta = s/\delta$, s is the loop-loop separation and $\delta = \sqrt{\omega\mu_0\sigma/2}$ is the skin depth (ω is the angular frequency of the source, μ_0 is the magnetic permeability of free space), 2) the instrument lays on the ground surface and free-space magnetic permeability.

From the LIN approach, McNeill (1980) defined sensitivity functions that calculate for horizontally layered models the contributions of each layer thickness and electrical conductivity to the apparent electrical conductivity, based on Wait (1962). Subsequently, due to its simplicity and linearity, numerous inversion schemes to estimate electrical conductivity vertical distribution profiles using McNeill (1980) sensitivity functions have been developed (e.g. Hendrickx et al., 2002; Monteiro Santos et al., 2011). However, previous studies suggest that using the LIN approximation approach, even under the LIN conditions provides inaccurate estimations of electrical conductivity in the subsurface. For example, Callegary et al. (2007) compared the sensitivity of the apparent electrical conductivity with respect to the vertical distribution using LIN approximation and Maxwell's equations for two-layered models and observed clear differences. Additionally, von Hebel et al. (2019) performed a multi-layered inversion using both the LIN approximation and Maxwell's exact solutions as forward models, finding erroneous electrical conductivity estimations using the LIN approximation.

One of the assumptions of the LIN approximations is that while the LIN conditions are being met the real part of the measurements (*in-phase* part) is very small, so it is considered negligible. This is a condition that is rarely accomplished since the bulk subsurface conductivity must be less than a few mS/m (Beamish, 2011). Previous studies mention the influence of the subsurface electrical conductivity on the *in-phase* response. Deidda et al. (2022) mentions that at a fixed magnetic permeability the *in-phase* component will increase as with increasing electrical conductivity of an assumed volume that influences the measurements. Delefortrie et al. (2014) presented the visual comparison of *in-phase* responses to evidence the similarity with the distribution of electrical conductivity, suggesting a relationship. de Alba and Rodriguez (2016) also investigated the possibility of getting more information from the available data, considering either the *in-phase* or the *quadrature* component of the signal for a regularized Gauss-Newton inversion scheme. In this chapter, we study the sensitivity of both the *quadrature* and *in-phase* components of the FDEM measurements and what information these measurements could provide from the distribution of the subsurface conductivity.

Using the full non-linear solution from Maxwell's equations for horizontally layered models can be computationally expensive to perform in an inversion scheme that needs to calculate many forward models in each minimization step. In this study, we use the semi-analytical modeler *empymod* (Werthmüller, 2017) that provides the exact magnetic response due to a magnetic point source in a layered-earth model with vertical trans-

verse isotropic (VTI) electrical conductivity. This modeler allows us to calculate the measurements for a large range of models and create a lookup table that can be used in a global search to find the electrical conductivity model that better explains the FDEM measurements. For completeness, we also use the LIN approximation function to create a lookup table and perform the global search methodology. The workflow using both semi-analytical and LIN lookup tables is applied to a numerical example and to data acquired for hydrogeophysical evaluation in Ackerdijkse Plassen, The Netherlands.

2.2. METHODOLOGY

The basic FDEM instrument consists of a pair of loops: a transmitter loop (T_x) and a receiver loop (R_x), where the subscript x denotes the measurement position on the x-axis. The system uses an alternating current flowing in the transmitter coil that generates a primary magnetic field $\mathbf{H}^{\mathrm{p}}$. This time-varying flux produces an electromotive force that induces eddy currents in conductive materials of the subsurface. The eddy currents then generate a secondary magnetic $\mathbf{H}^{\mathrm{s}}$. Both $\mathbf{H}^{\mathrm{p}}$ and $\mathbf{H}^{\mathrm{s}}$ fields go through the receiver coil. Consequently, a voltage is induced in the receiver coil (the time variation of the magnetic flux is then measured).

Since the primary field $\mathbf{H}^{\mathrm{p}}$ is known, FDEM instruments can provide the coupling ratio between the secondary magnetic field induced in the ground and the primary magnetic field from the direct wave propagating from the transmitter through the air to the receiver coil, which is a complex ratio:

$$\frac{\mathbf{H}^{\mathrm{s}}}{\mathbf{H}^{\mathrm{p}}} = \mathbf{P} + i\mathbf{Q}, \tag{2.1}$$

where $\mathbf{P}$ represents the *in-phase* part and $\mathbf{Q}$ represents the *out-of-phase* or *quadrature* part. Equation 2.1 is derived from the polar decomposition of Equation 1.11.

SEMI-ANALYTIC (SA) FORWARD MODEL

From Ward and Hohmann (1987), for FDEM sensors where the distance between the transmitter and receiver coils is at least five times larger than the radius of the coils, the coils are considered independent magnetic dipoles. Ward and Hohmann (1987) derived the formulations for the axial component of the magnetic field generated by a magnetic dipole, assuming a horizontally layered subsurface. The derived equations for the horizontal coplanar (HCP), vertical coplanar (VCP), and perpendicular (PRP) coil orientations, where both transmitter and receiver coils are placed at the same elevation, a, are shown in the following equations:

$$Z_{\mathrm{HCP}} = \frac{\mathbf{H}^{\mathrm{s}}_z}{\mathbf{H}^{\mathrm{p}}_z} = -s^3 \int_0^\infty R_0 e^{-2\lambda a} \lambda^2 J_0(\lambda s) d\lambda, \tag{2.2a}$$

$$Z_{\mathrm{VCP}} = \frac{\mathbf{H}^{\mathrm{s}}_x}{\mathbf{H}^{\mathrm{p}}_x} = -s^2 \int_0^\infty R_0 e^{-2\lambda a} \lambda J_1(\lambda s) d\lambda, \tag{2.2b}$$

$$Z_{\mathrm{PRP}} = \frac{\mathbf{H}^{\mathrm{s}}_x}{\mathbf{H}^{\mathrm{p}}_z} = \; s^3 \int_0^\infty R_0 e^{-2\lambda a} \lambda^2 J_1(\lambda s) d\lambda, \tag{2.2c}$$

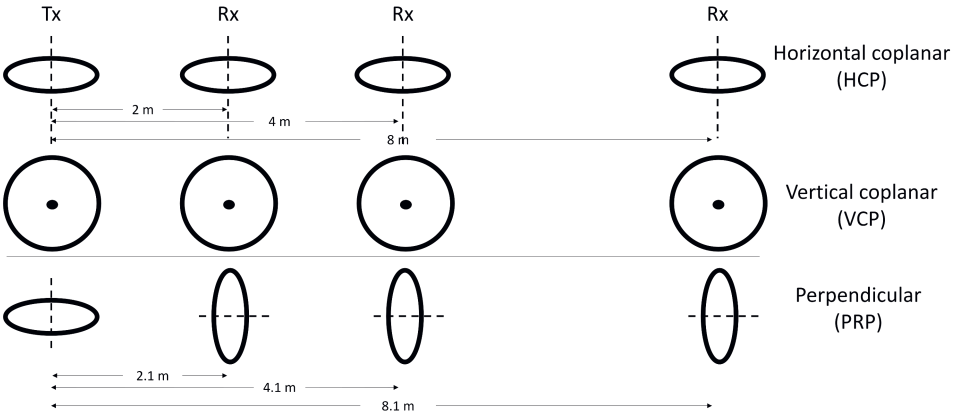


Figure 2.1: FDEM loop-loop configurations.

where λ is the Hankel transform integral parameter, R_0 is the reflection coefficient, J_0 and J_1 are the Bessel functions of zeroth and first order respectively. In Equations 2.2 the integral represents the contribution from each layer to the measurements. With the SA forward model, we compute $\mathbf{H}^{\mathrm{p}}$, $\mathbf{H}^{\mathrm{s}}$ and calculate the complex ratios $Z_{\mathrm{HCP}}, Z_{\mathrm{VCP}}$ and Z_{PRP}, to obtain $\mathbf{Q}$ and $\mathbf{P}$ values.

The equations are solved for the following coil configurations: 3 loop-loop orientations (HCP, VCP, and PRP) with three different offsets each (2, 4, 8 m for HCP and VCP coils; 2.1, 4.1, 8.1 m for the PRP loop orientation) at a frequency of 9000 Hz (see Figure 2.1). FDEM data is modeled for $n = 226981$ electrical conductivity 2-layered models with first layer thickness h_1 ranging from 0.1 m to 7 m, sampled linearly in 51 steps. The electrical conductivity for each layer ranged from 1 mS/m up to 100 mS/m, sampled logarithmically in 51 steps. The electrical conductivity values for the proposed loop-loop geometry do not largely deviate from satisfying the LIN conditions. Therefore, the models are formulated by two layers where the parameters are the logarithms of the conductivity and the thickness, $\mathbf{m} = [\log(\sigma_1), \log(\sigma_2), h_1]$. The data generated for each model contains the values of $\mathbf{Q}$ and $\mathbf{P}$ for each coil geometry and each loop-loop offset in ppt (parts per thousand), $\mathbf{d} = [\mathbf{Q}_{\mathrm{HCP}}, \mathbf{Q}_{\mathrm{VCP}}, \mathbf{Q}_{\mathrm{PRP}}, \mathbf{P}_{\mathrm{HCP}}, \mathbf{P}_{\mathrm{VCP}}, \mathbf{P}_{\mathrm{PRP}}]$. The FDEM data $\mathbf{d}$ is computed and stored in the lookup table $\mathbf{D}_{\mathrm{SA}} = [\mathbf{d}_1, \mathbf{d}_2, ..., \mathbf{d}_n]$, which is then used in the global search. The workflow for the methodology is shown in Figure 2.3 , where this stage is shown as step 1: Forward operation.

LOW INDUCTION NUMBER (LIN) FORWARD MODEL

McNeill (1980) proposed that the Equations 2.2 can be modified to a linear relationship between a bulk apparent conductivity of the subsurface σ_a and the imaginary part of the complex ratio $\Im(\mathbf{H}^{\mathrm{s}}/\mathbf{H}^{\mathrm{p}})$, which belongs to the *quadrature* $\mathbf{Q}$ as we have mentioned, for low induction numbers as follows:

$$\sigma_a^{\mathrm{LIN}} = \frac{4}{\mu_0 \omega s^2} \mathbf{Q}. \tag{2.3}$$

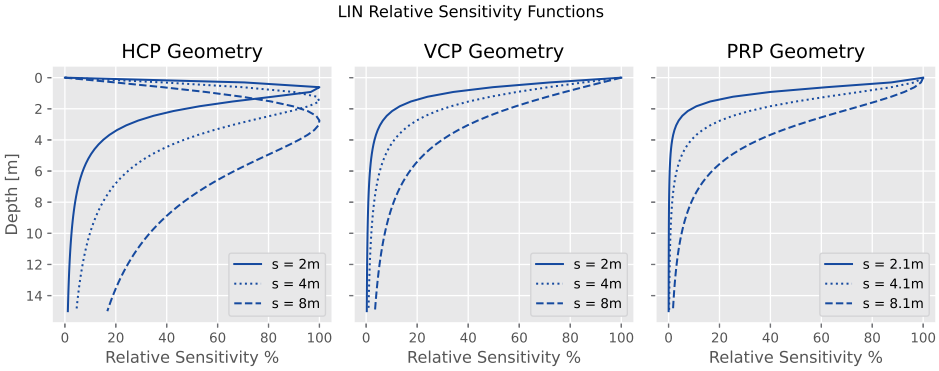


Figure 2.2: LIN Relative sensitivity functions for each loop-loop configuration.

This approximation is defined for coils directly laying on the ground surface. From the LIN approximation, the vertical distribution of the electrical conductivity is linearly related to relative sensitivity (S_R) functions presented in McNeill (1980), from Wait (1962). These functions are based in the LIN conditions, where the sensitivity of the different coil orientations is a function of depth, frequency and the loop-loop offset solely, and does not depend on the subsurface conductivity distribution. These relative sensitivity functions S_R weight the contribution of a 2-layered function in the following manner:

$$\sigma_a^{\text{LIN}} = \sigma_1[1 - S_R(b_1)] + \sigma_2[S_R(b_1)], \tag{2.4}$$

where b_1 is the depth of the first layer normalized by the loop-loop separation. The S_R sensitivity functions for the different loop-loop separations are defined by McNeill (1980) and Monteiro Santos et al. (2011), as:

$$S_R^{\text{HCP}}(b) = \frac{1}{\sqrt{(4b^2+1)}}, \tag{2.5a}$$

$$S_R^{\text{VCP}}(b) = \sqrt{(4b^2+1)} - 2b, \tag{2.5b}$$

$$S_R^{\text{PRP}}(b) = \frac{2b}{(4b^2+1)^{1/2}}. \tag{2.5c}$$

These relative sensitivity functions are shown for the FDEM system configurations in Figure 2.2. These equations are used to repeat step 1 Forward operation and obtain for $n = 226981$ possible models the lookup table $\mathbf{D}_{\text{LIN}} = [\mathbf{d}_1, \mathbf{d}_2, ..., \mathbf{d}_n]$.

GLOBAL SEARCH

After storing the solutions computed in step 1 of the workflow (see Figure 2.3) we perform for each position i in a survey a global search that minimizes the misfit $\min(\mathbf{d} - \mathbf{d}_i)$ between the measurement $\mathbf{d}_i$ and all the measurements $\mathbf{d}$ stored in lookup table $\mathbf{D}$. The minimum misfit yields the best electrical conductivity model $\mathbf{m}_i$. Recall that each

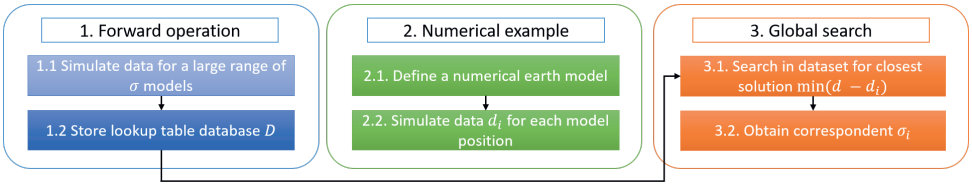


Figure 2.3: Global search workflow.

data vector **d** contains the measurements from all coil distances and loop configurations shown in Figure 2.1.

SENSITIVITY OF THE *quadrature* AND *in-phase* MEASUREMENTS

For each loop-loop geometry and measurement component (**Q** or **P**), the sensitivity of the measurements to changes in the electrical conductivity for a homogeneous halfspace is calculated (see Figures 2.4 and 2.5). In Figure 2.4, the results show that the instrument *quadrature* measurements are overall quite sensitive to the first few meters of the subsurface (< 5 meters), increasing in depth with increasing loop-loop separation. Below this depth, the sensitivity decays. The sensitivity differs between loop-loop geometries; for this reason, FDEM instrument developers have incorporated multiple configurations to include the sensitivity to different volumes of the subsurface and obtain more information (Wait, 1962, Deidda et al., 2022, Blanchy et al., 2024).

In Figure 2.4, it is clear that the sensitivity of the measurement also changes with halfspace conductivity, especially for the largest offset in all geometries. The sensitivity of the measurements in the *in-phase* component (Figure 2.5) also differs from loop-loop geometry and is affected by the halfspace conductivity. For increasing offsets, the LIN conditions break down even with a halfspace conductivity under 10 mS/m. Therefore, the *in-phase* part is no longer negligible and is sensitive to the subsurface conductivity.

2.3. NUMERICAL EXAMPLE

In order to test the appropriate forward function to use for estimating 2-layered electrical conductivity models, we use the workflow presented in Figure 2.3 in two numerical cases. The global search is applied for each position in a 2D section of stitched 1D earth models using 4 different lookup tables: 1) a lookup table with semi-analytic **Q** values, $\mathbf{D}_{\text{SA-Q}}$, 2) a lookup table with semi-analytic **P** values, $\mathbf{D}_{\text{SA-P}}$, 3) a lookup table with the full semi-analytic measurements **Q** and **P**, $\mathbf{D}_{\text{SA}}$, and 4) a lookup table with the LIN forward **Q** values, $\mathbf{D}_{\text{LIN}}$.

To evaluate the accuracy of the estimation, we calculate the normalized root mean squared error (RMSE) between true and estimated 1D models obtained for the σ and h model parameters, as follows:

$$\text{RMSE}(\mathbf{m}_{\text{true}}, \mathbf{m}_{\text{pred}}) = \sqrt{\frac{\sum_{i=0}^{M-1} (m_{\text{true}} - m_{\text{pred}})^2}{M}}, \tag{2.6}$$

where $\mathbf{m}_{\text{true}}$ is the true model and $\mathbf{m}_{\text{pred}}$ is the predicted model.

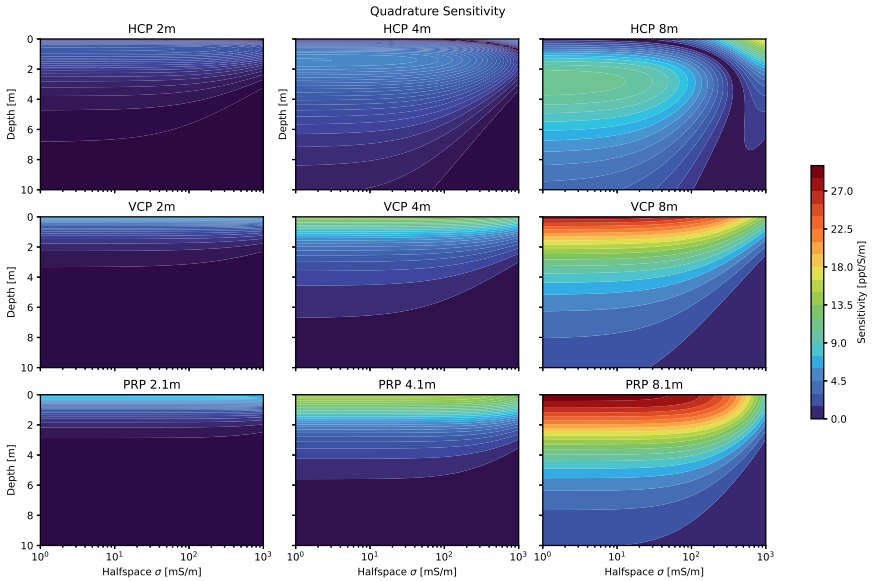


Figure 2.4: Sensitivity of *Quadrature* measurements with respect to halfspace conductivity for the different loop-loop configurations.

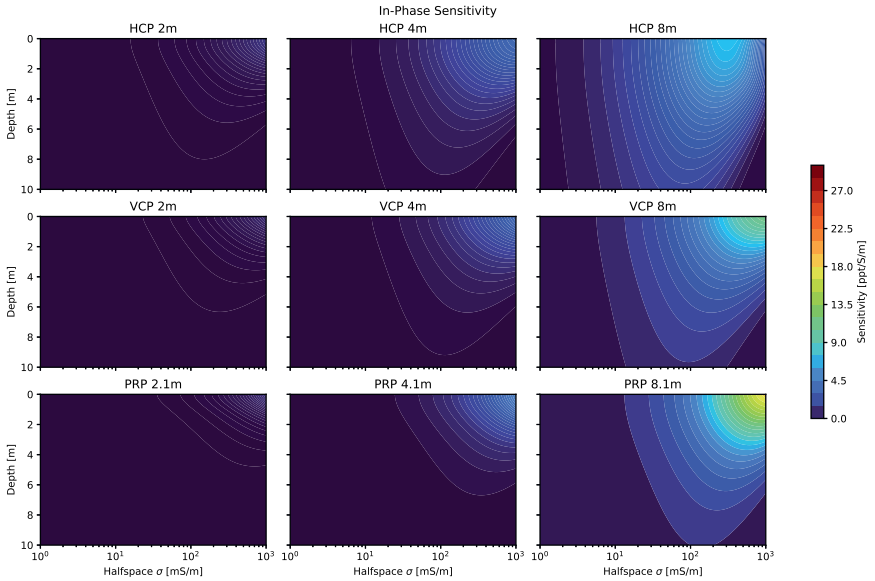


Figure 2.5: Sensitivity of *In-Phase* measurements with respect to halfspace conductivity for the different loop-loop configurations.

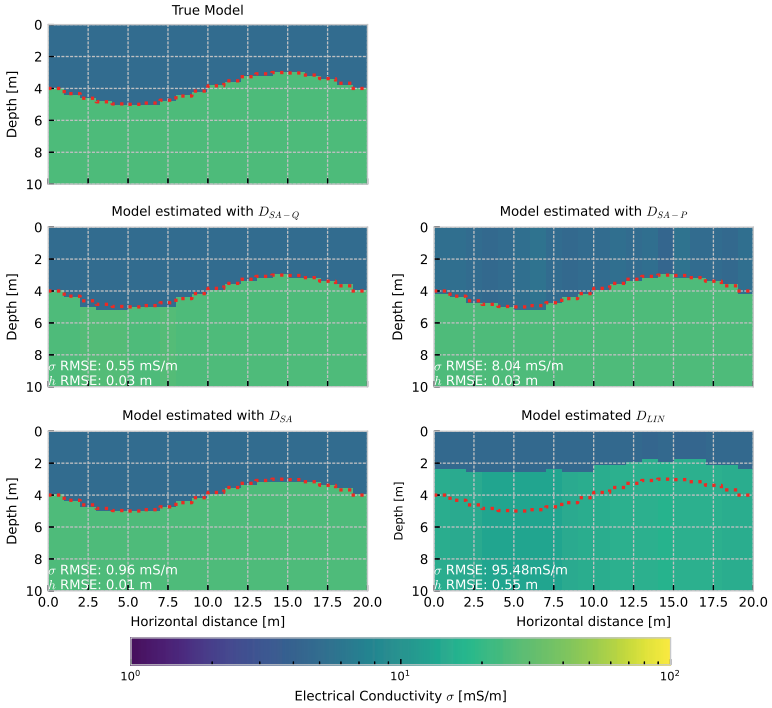


Figure 2.6: Results of estimation of electrical conductivity models for the upper conductive case. The RMSE of the estimation with respect to the true model is shown on the left of each subfigure. The red dotted line shows the thickness of the first layer of the true model.

The first numerical example has an upper resistive layer (σ_1 = 5 mS/m, σ_2 = 25 mS/m). The results of the estimations with the 4 lookup tables are shown in Figure 2.6. From the results, it is clear that using either only **Q** or **P** measurements in a lookup table approach is sufficient to estimate the model with an RMSE < 10 mS/m. Combining both measurements in a lookup table search further improves the accuracy. The estimation using the $\mathbf{D}_{\text{LIN}}$ lookup table is not as accurate in both the electrical conductivity values and the thickness of the first layer. The data simulated using Equation 2.2 of the estimated models are shown in Figures 2.8 and 2.9, where the $\mathbf{D}_{\text{LIN}}$ results deviate from the true data, suggesting that the electrical conductivity values of the model do not comply with the LIN conditions. In the data RMSE plots, it is also noticeable that the *in-phase* measurements are fluctuating in the smallest offsets, perhaps due to the low sensitivity to conductivity in this geometry, as it is observed in 2.5.

For the upper conductive case (σ_1 = 25 mS/m, σ_2 = 5 mS/m) shown in Figure 2.7, the estimation results are similar to the previous case. The $\mathbf{D}_{\text{LIN}}$ lookup table produces the worst fit to the true model. Moreover, the $\mathbf{D}_{\text{SA-Q}}$ and $\mathbf{D}_{\text{SA-P}}$ lookup table search results produce estimations with RMSE < 10 mS/m. These results also suggest that the **P** part of the response is sensitive to the electrical conductivity distribution of the subsurface, even with the low conductivity values of the models tested. In both numerical examples,

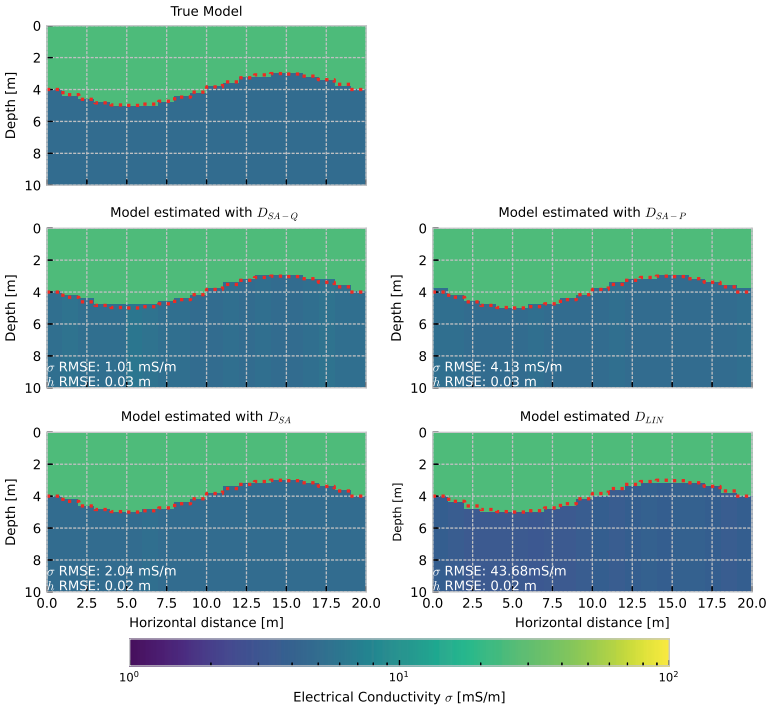


Figure 2.7: Results of estimation of electrical conductivity models for the upper conductive case.

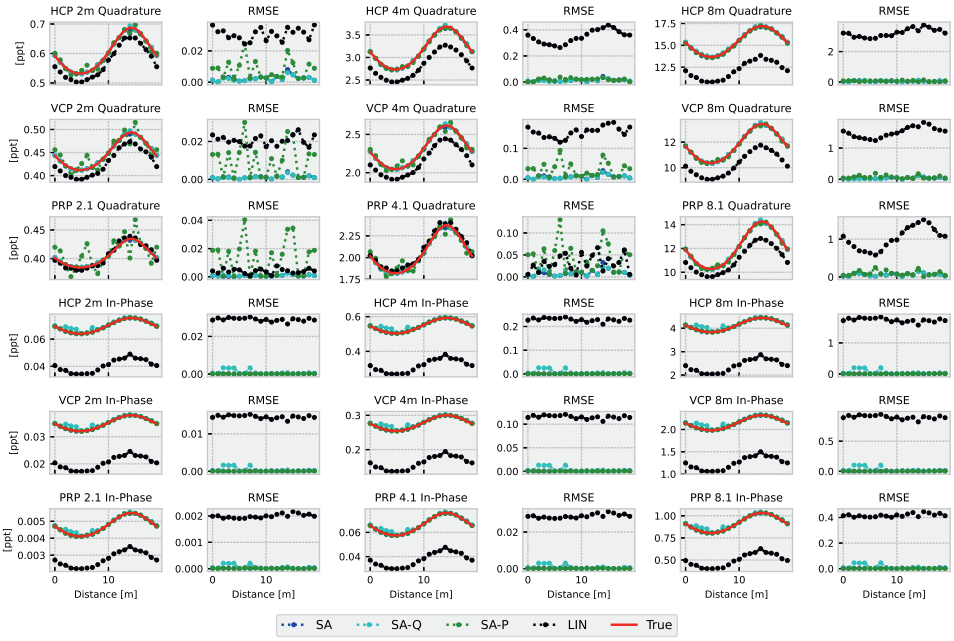


Figure 2.8: Upper resistive case. Comparison of the data of the estimated electrical conductivity models with respect to the true data for every loop-loop configuration. In the first, third and fifth columns are the measurements for each position of the model. In the second, fourth and sixth columns, the RMSE of the measurements is plotted.

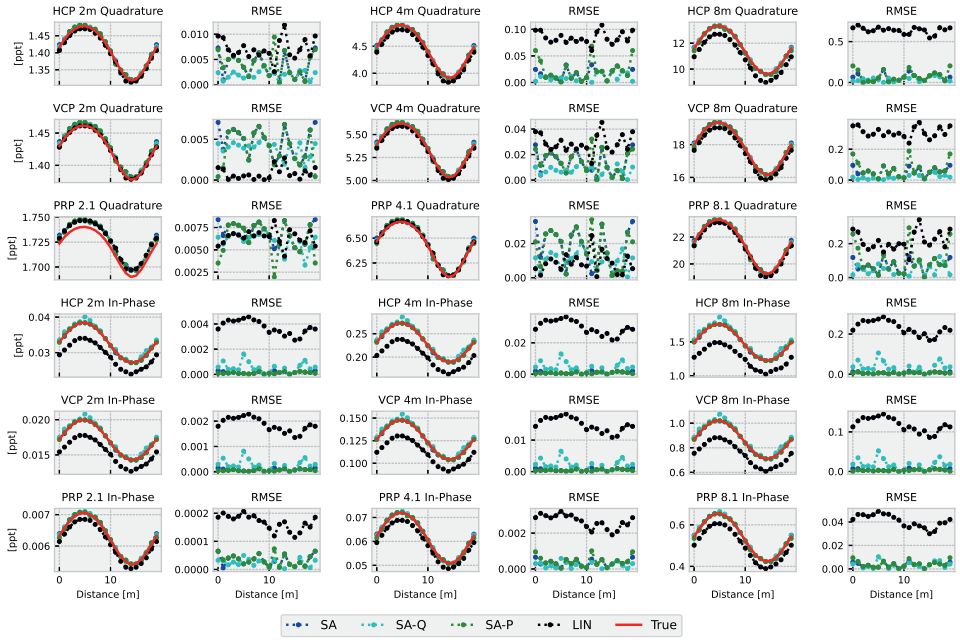


Figure 2.9: Upper conductive case. Comparison of the data of the estimated electrical conductivity models with respect to the true data for every loop-loop configuration.

as the loop-loop offset increases, the data from the $\mathbf{D}_{\text{LIN}}$ estimated model deviates from the true data. This also indicates the breakdown of the LIN conditions.

2.4. CASE STUDY: ACKERDIJKSE PLASSEN

We apply the methodology for FDEM data acquired in the natural monument Ackerdijkse Plassen, The Netherlands (see Figure 2.10). A total of 37 measurement lines were acquired with an instrument configuration as described in Figure 2.1. The lines were acquired in a southwest - northeast direction as shown in the Figure 2.10. For offsets up to 4m, the $\mathbf{P}$ values are considered less accurate according to the manufacturer of the FDEM instrument (Taylor, 2023), therefore, these values were not included in the methodology. The global search is performed using the $\mathbf{D}_{\text{SA-Q}}$, $\mathbf{D}_{\text{SA-P}}$, $\mathbf{D}_{\text{SA}}$ and $\mathbf{D}_{\text{LIN}}$ lookup tables separately. The estimated electrical conductivity models for Lines 1, 2 and 3 are shown in Figures 2.11, 2.12, and 2.13, respectively. The location of these lines are shown in Figure 2.10. In Figures 2.14, 2.15 and 2.16 the data fit between the acquired measurements and data simulated for the estimated models is shown.

In the electrical conductivity estimation results (see Figures 2.11, 2.12 and 2.13), using separate lookup tables provides quite different estimations. The results of $\mathbf{D}_{\text{SA-Q}}$, $\mathbf{D}_{\text{SA-P}}$ and $\mathbf{D}_{\text{SA}}$ show an upper resistive layer above a conductive layer. However, the depth and conductivity of these layers is not consistent. On the other hand, in the $\mathbf{D}_{\text{LIN}}$ case, the estimation shows a lower resistive body, similarly to $D_{\text{SA-Q}}$.

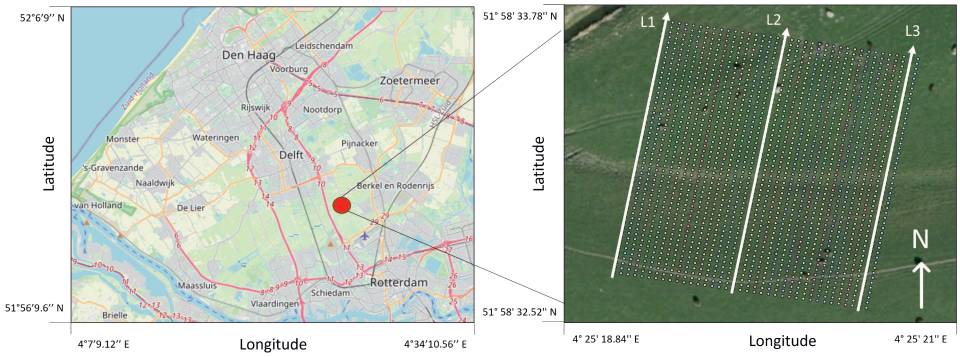


Figure 2.10: Study Area: Ackerdijkse Plassen, The Netherlands. The cross-sections L1, L2 and L3 are highlighted.

The data fit of the model estimations illustrates clear differences (see Figures 2.14, 2.15, 2.16). The acquired measurements are better described overall by the estimation obtained using $\mathbf{D}_{\text{SA}}$. When simulating the measurements using the LIN forward function (Equation 2.4), it seems that the model corresponding to $\mathbf{D}_{\text{LIN}}$ describes well the field measurements. However, when simulating SA data for the $\mathbf{D}_{\text{LIN}}$ estimation, as shown in the figure as SA-LIN data, it is clear that this model does not accurately describe the field measurements.

Additionally, we can see in the data fit illustrations that, although the $\mathbf{D}_{\text{SA-Q}}$, $\mathbf{D}_{\text{SA-P}}$ data fit is good, the estimations differ from the $\mathbf{D}_{\text{SA}}$. This suggests that using either SA-Q or SA-P separately extracts only a part of the full information of the measurements, and therefore provides an incomplete and probably inaccurate estimation of the subsurface. Moreover, there could be 3D effects in the field data that are not accounted for in Equations 2.2 and 2.3. It is also important to consider that the electrical conductivities measured in the field showed values of σ_a where the LIN conditions are not satisfied for the HCP 8m coil configuration.

Generating and storing the lookup table for the examples shown took only minutes. Afterward, finding the best-fitting data for one position in the lookup table can be accomplished in just 7.68 milliseconds. In our numerical example, we estimated the electrical conductivity model using a dataset with 20 horizontal distance positions, which only took 70.78 milliseconds. For the field example, we utilized only the HCP and VCP coil geometries in the data measurements. Estimating the 50 positions presented in this case only took 118.90 milliseconds. Our computations were performed using an Intel(R) Core(TM) i7-8665U CPU with 8 cores.

2.5. CONCLUSIONS

We used a semi-analytical modeler to simulate the exact response of frequency-domain electromagnetic induction measurements in a layered earth and obtain a lookup table to be used in a global search workflow. After computing the lookup table to find the best fitting measurement for one position can be done in milliseconds. This method yields a

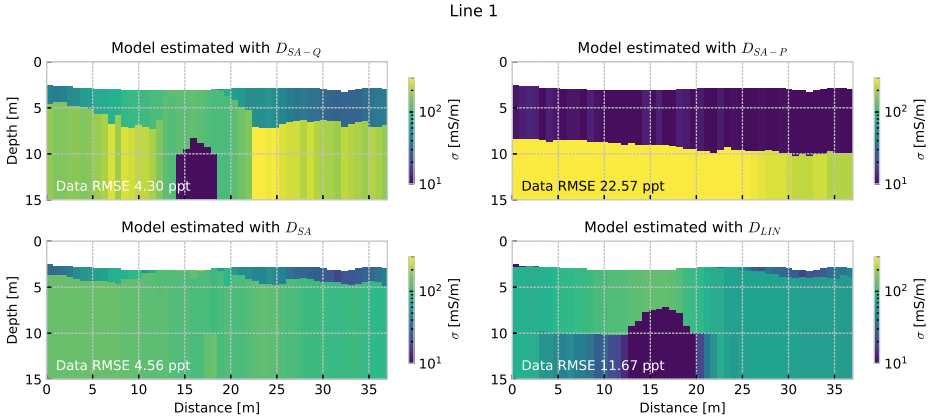


Figure 2.11: Estimated electrical conductivity models for Line 1. Top left: Model estimated with $\mathbf{D}_{SA-Q}$ lookup table. Top right: Model estimated with $\mathbf{D}_{SA-P}$ lookup table. Bottom left: Model estimated with $\mathbf{D}_{SA}$ lookup table. Bottom right: Model estimated with $\mathbf{D}_{LIN}$ lookup table.

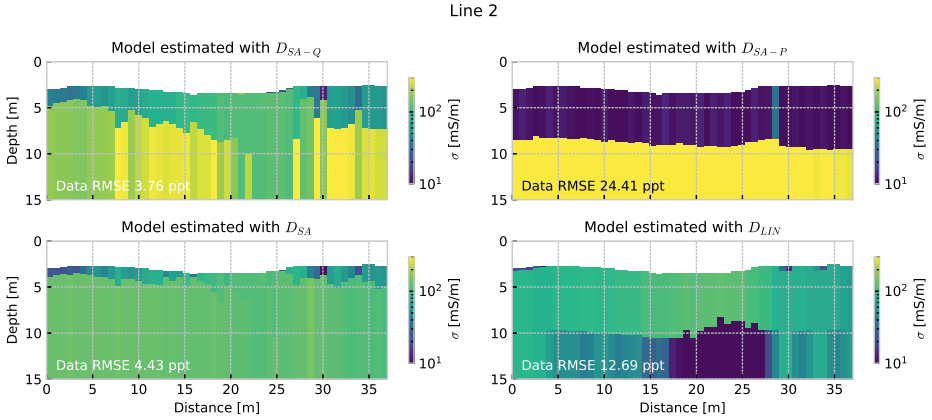


Figure 2.12: Estimated electrical conductivity models for Line 2.

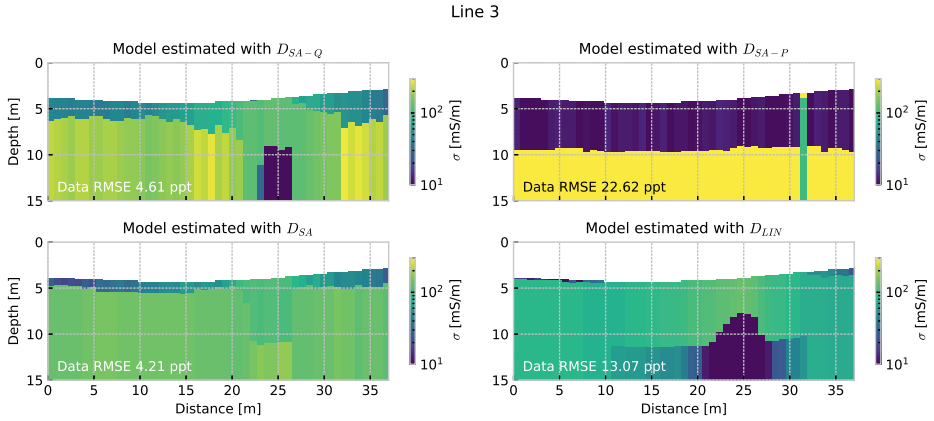


Figure 2.13: Estimated electrical conductivity models for Line 3.

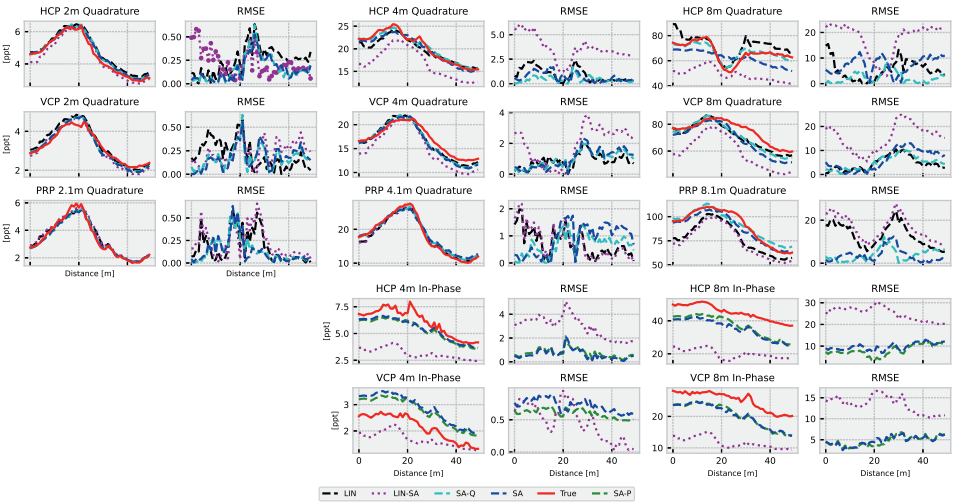


Figure 2.14: Data fit of field measurements and simulated measurements for each estimated model for Line 1. The SA, SA-Q, SA-P and SA-LIN were calculated using Equation 2.2. The LIN measurements were calculated using Equation 2.4. LIN-SA shows the poorest accuracy.

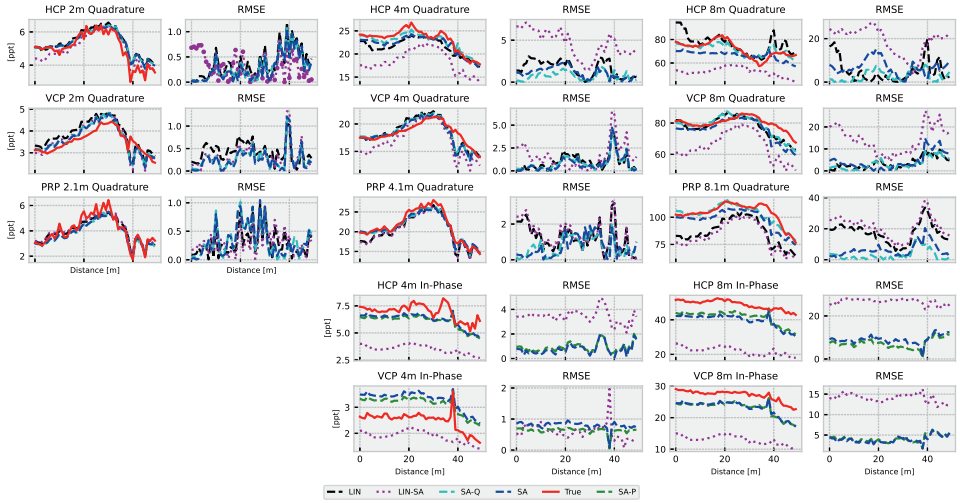


Figure 2.15: Data fit of field measurements and simulated measurements for each estimated model for Line 2.

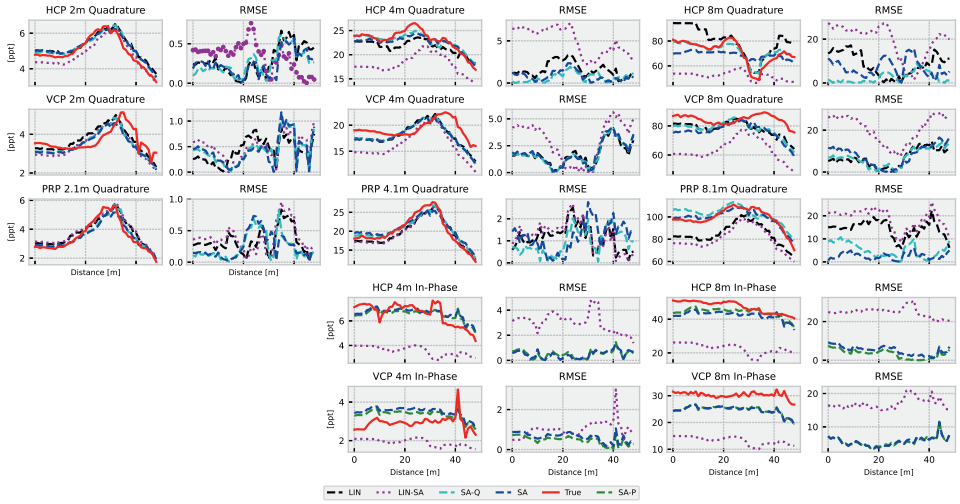


Figure 2.16: Data fit of field measurements and simulated measurements for each estimated model for Line 3.

fast estimation for horizontal two-layered models of the subsurface, which can be easily applied in field datasets. Furthermore, the application of the semi-analytical approach to the numerical example reproduced the electrical conductivity model accurately. We compared the results of using the semi-analytical simulated measurements with respect to using low induction number approximation functions to generate the lookup table. The global search methodology using the low induction number approximation lookup table provided a poor estimation in the case of two-layered models, even when the low induction number conditions are satisfied.

Moreover, this chapter illustrates the sensitivity of the quadrature and in-phase components of the frequency-domain electromagnetic induction measurements separately. Estimates with numerical and field case examples showed how both components contain information about the electrical conductivity of the subsurface. This stresses the importance of using both parts of the complex measurement in the estimation of electrical conductivity earth properties.

DATA AVAILABILITY

The codes and data used in this chapter is available via 4TU.ResearchData: (Link).

BIBLIOGRAPHY

Beamish, D. (2011). Low induction number, ground conductivity meters: A correction procedure in the absence of magnetic effects. *Journal of Applied Geophysics*, *75*(2), 244–253. https://doi.org/10.1016/j.jappgeo.2011.07.005

Blanchy, G., McLachlan, P., Mary, B., Censini, M., Boaga, J., & Cassiani, G. (2024). Comparison of multi-coil and multi-frequency frequency domain electromagnetic induction instruments [Publisher: Frontiers]. *Frontiers in Soil Science*, *4*. https://doi.org/10.3389/fsoil.2024.1239497

Callegary, J. B., Ferré, T. P. A., & Groom, R. W. (2007). Vertical Spatial Sensitivity and Exploration Depth of Low-Induction-Number Electromagnetic-Induction Instruments. *Vadose Zone Journal*, *6*(1), 158–167. https://doi.org/10.2136/vzj2006.0120

de Alba, P. D., & Rodriguez, G. (2016). Regularized inversion of multi-frequency EM data in geophysical applications. In F. Ortegón Gallego, M. V. Redondo Neble, & J. R. Rodríguez Galván (Eds.), *Trends in differential equations and applications* (pp. 357–369). Springer International Publishing. https://doi.org/10.1007/978-3-319-32013-7_20

Deidda, G. P., Carlo, L. D., Caputo, M. C., & Cassiani, G. (2022). Frequency domain electromagnetic induction imaging: An effective method to see inside a capped landfill. *Waste Management*, *144*, 29–40. https://doi.org/10.1016/j.wasman.2022.03.007.

Delefortrie, S., Saey, T., Van De Vijver, E., De Smedt, P., Missiaen, T., Demerre, I., & Van Meirvenne, M. (2014). Frequency domain electromagnetic induction survey in the intertidal zone: Limitations of low-induction-number and depth of exploration. *Journal of Applied Geophysics*, *100*, 14–22. https://doi.org/10.1016/j.jappgeo.2013.10.005

Hendrickx, J., Borchers, B., Corwin, D., Lesch, S., Hilgendorf, A., & Schlue, J. (2002). Inversion of soil conductivity profiles from electromagnetic induction measurements: Theory and experimental verification. *Soil Science Society of America Journal*, *66*(3), 673–685. https://doi.org/10.2136/sssaj2002.6730

McNeill, J. D. (1980). *Electromagnetic terrain conductivity measurement at low induction numbers* (tech. rep.). Geonics Limited. ON, Canada. https://geonics.com/pdfs/technicalnotes/tn6.pdf

Monteiro Santos, F. A., Triantafilis, J., & Bruzgulis, K. (2011). A spatially constrained 1D inversion algorithm for quasi-3D conductivity imaging: Application to DUALEM-421 data collected in a riverine plain. *Geophysics*, *76*(2), B43–B53. https://doi.org/10.1190/1.3537834

Taylor, R. (2023, April). Website of DualEM manufacturer: EM Induction (accessed on 21/04/2023). Retrieved April 21, 2023, from https://dualem.com/documents/em-induction/

von Hebel, van der Kruk, Huisman, Mester, Altdorff, Endres, Zimmermann, Garré, & Vereecken. (2019). Calibration, Conversion, and Quantitative Multi-Layer Inversion of Multi-Coil Rigid-Boom Electromagnetic Induction Data. *Sensors*, *19*(21), 4753. https://doi.org/10.3390/s19214753

Wait, J. R. (1962). A note on the electromagnetic response of a stratified earth. *Geophysics*, *27*(3), 382–385. https://doi.org/10.1190/1.1439028

Ward, S. H., & Hohmann, G. W. (1987). 4. Electromagnetic Theory for Geophysical Applications. *Electromagnetic Methods in Applied Geophysics: Volume 1, Theory*, 130–311.

Werthmüller, D. (2017). An open-source full 3D electromagnetic modeler for 1D VTI media in Python: Empymod. *Geophysics*, *82*(6), WB9–WB19. https://doi.org/10.1190/geo2016-0626.1

3

ESTIMATION OF ELECTRICAL CONDUCTIVITY MODELS

In summary, there are no small problems.
Problems that appear small are large problems that are not understood.

Santiago Ramón y Cajal

Electromagnetic induction measurements from multi-loop configuration instruments are used to obtain information about the electrical conductivity distribution in the subsurface. The resulting inverse problem might not have a unique and stable solution. In that case, a local inversion method can be trapped in a local minimum and lead to an incorrect solution. In this study, we evaluate the well-posedness of the inverse problem for two and three-layered electrical conductivity models. We show that for a two-layered model, uniqueness is ensured only when both in-phase and quadrature data are available from the measurements. Results from a Gauss-Newton inversion and a lookup table demonstrate that the solution space is convex. Furthermore, we demonstrate that for even a simple three-layered model, the data contained in such measurements are insufficient to reach a correct or stable solution. For models with more than 2 layers, independent prior information is necessary to solve the inverse problem. The insights from the numerical examples are applied in a field case.

3.1. INTRODUCTION

Near-surface geophysical technologies are increasingly being used to estimate the electrical conductivity of the subsurface as a way to better understand soil and groundwater

This chapter was published as M. Carrizo Mascarell, D. Werthmüller, and E. Slob, *Estimation of electrical conductivity models using multi-coil rigid-boom electromagnetic induction measurements*, Computers and Geosciences **2024**, 105732 (193). Minor modifications have been applied to the text and figures for thesis consistency

properties. A commonly used geophysical technique for this purpose is the electromagnetic induction method with FDEM instruments. The FDEM method can be used for a wide range of environmental and hydrogeophysical applications such as soil characterization (Moghadas and Christiansen, 2020), locating contaminants (de Oliveira et al., 2020), evaluation of shallow aquifers (Kiflai and Whitman, 2023), and detection of buried objects (Thiesson et al., 2018).

The non-destructive and cost-effective advantages of frequency-domain electromagnetic induction (FDEM) instruments make them valuable for characterizing shallow subsurface properties. FDEM instruments enable rapid data collection across extensive areas, facilitating quick acquisition of information. Consequently, there is a need to promptly transform these data into a model interpretation of the subsurface. The ability to generate near real-time accurate estimations of subsurface electrical conductivity would turn the collected measurements into an effective decision-making tool.

However, this is not a trivial task. The relationship between the electrical conductivity of the subsurface and the measurements obtained by the FDEM instrument is nonlinear. For this reason, the inverse problem is usually solved either by making a linear approximation of the solution, which is not feasible for situations with large induction number (Beamish, 2011; Delrue et al., 2020), or iteratively as an optimization problem. Some examples of the optimization approach to obtain layered electrical conductivity models are given by Monteiro Santos et al. (2011), Deleersnyder et al. (2020) and Klose et al. (2022). This inverse scheme requires computing time to perform the forward function iteratively, which might not be practical for near real-time estimation. Moreover, the inverse problem is non-unique, due to the inherent nonlinearity of the governing physical laws. This factor makes the outcome of the inversion by iterative forward modeling strongly depend on the chosen initial model.

In the following study, we present in Section 3.2 in detail how we compute the FDEM instrument responses using the method described by Ward and Hohmann (1987) for magnetic dipoles over a horizontally, n-layered halfspace. In Section 3.3 we describe two estimation algorithms: the global search method using a lookup table and the Gauss-Newton inversion. In Section 3.4 we evaluate both methods using numerical exercises for 2-layered and 3-layered earth models, with different electrical conductivity distributions. We investigate the uniqueness of the solution when in-phase and/or quadrature components of the measurements are available. We also analyze the stability of the solutions for noise presence in the data. From the results of these exercises, we discuss the limitations of the measurements and the methods to obtain a unique solution for 3-layered earth models. Finally, we show the usefulness of the measurements in a field data case, assuming a 2-layered earth.

3.2. BACKGROUND

The FDEM instrument consists of two components: a transmitter coil T_x and a receiver coil R_x, where the subscript x denotes the measurement position on the x-axis. The system uses as a source an alternating current flowing in the transmitter coil to create a primary magnetic field $\mathbf{H}^{\mathrm{p}}$, where the magnetic dipole is perpendicular to the transmitter coil plane of T_x. This time-varying flux produces an electromotive force, inducing eddy currents in the conductive materials of the subsurface, which generate a secondary

magnetic field $\mathbf{H}^s$. The time-varying fluxes of the magnetic fields $\mathbf{H}^p$ and $\mathbf{H}^s$ pass through the receiver coil, inducing a voltage that can be measured by the instrument. Since the primary field $\mathbf{H}^p$ is known, FDEM instruments can provide the mutual impedance ratio between $\mathbf{H}^s$ and $\mathbf{H}^p$, which contains information about the subsurface conductivity.

The solutions of the mutual impedance ratio for diffusive electromagnetic fields for loop-loop configurations over a horizontally layered medium are given by Wait (1982) for the horizontal coplanar (HCP), vertical coplanar (VCP), and perpendicular (PRP) coil orientations as in Equation 2.2.

Ward and Hohmann (1987) proposes that for FDEM sensors, where the distance between the transmitter and receiver coils is at least five times larger than the radius of the coils, the coils are considered magnetic dipoles. Moreover, in Equation 4.19 on page 205 of Ward and Hohmann (1987), we find that R_0 can be calculated recursively, beginning with $R_{n+1} = 0$ and

$$R_n = \frac{\frac{\Gamma_n - \Gamma_{n+1}}{\Gamma_n + \Gamma_{n+1}} + R_{n+1} e^{-2\Gamma_{n+1} h_{n+1}}}{1 + \frac{\Gamma_n - \Gamma_{n+1}}{\Gamma_n + \Gamma_{n+1}} R_{n+1} e^{-2\Gamma_{n+1} h_{n+1}}}, \tag{3.1}$$

where $\Gamma_n = \sqrt{\lambda^2 + \gamma_n^2}$, the vertical wavenumber is defined as $\gamma_n = \sqrt{\omega\mu_0(\mathrm{i}\sigma_n - \omega\epsilon_0)}$, ω is the angular frequency, μ_0 is the magnetic permeability of free space, ϵ_0 is the vacuum permittivity, h is the layer thickness, λ is the radial component of the wavenumber, and σ_n is the electrical conductivity of the n-th layer. For a diffusive field approximation $\Gamma_0 = \lambda$. The ground surface is at $z = 0$, and the z-axis points into the ground.

3.3. METHODOLOGY

DATA GENERATION

Considering an earth model with 2 layers, with first layer thickness h_1, we end up with the following equations to solve the reflection coefficient described by Ward and Hohmann (1987):

$$R_2 = 0, \tag{3.2a}$$

$$R_1 = \frac{\Gamma_1 - \Gamma_2}{\Gamma_1 + \Gamma_2}, \tag{3.2b}$$

$$R_0 = \frac{\frac{\lambda - \Gamma_1}{\lambda + \Gamma_1} + R_1 e^{-2\Gamma_1 h_1}}{1 + \frac{\lambda - \Gamma_1}{\lambda + \Gamma_1} R_1 e^{-2\Gamma_1 h_1}}. \tag{3.2c}$$

It is possible to obtain the ratios between primary and secondary magnetic fields for each coil geometry using Equation 2.2 and solving the Hankel transform using a digital filter (Werthmüller et al., 2019). This forward operator is fast and easy to compute, generating quickly a large range of possible 1D earth models and storing them in a lookup table.

We assume the model parameters to be $\mathbf{m} = [\sigma_1, \sigma_2, h_1]$, where σ_1, σ_2 are the electrical conductivities of the two layers, h_1 is the thickness of the first layer, the second layer is the rest of the halfspace. We use Equations 3.2a - 3.2c to calculate the response R_0 and subsequently compute the ratios $Z_{\mathrm{HCP}}, Z_{\mathrm{VCP}}$ and Z_{PRP} using Equation 2.2 for an FDEM

Table 3.1: Lookup tables variables

	Lookup table $\mathbf{D}_{\text{2-layers}}$	Lookup table $\mathbf{D}_{\text{3-layers}}$
Model parameters $\mathbf{m}$	h_1, σ_1, σ_2	$h_1, h_2, \sigma_1, \sigma_2, \sigma_3$
Number of model parameters M	3	5
Number of layers	2	3
σ range	10 - 2000 mS/m	10 - 2000 mS/m
h range	0.1 - 7 m	0.15 - 5 m
Number of samples N	121	51
Number of models simulated N^M	1,771,561	345,025,251

system shown in Figure 2.1. Each ratio is a complex number where the real part is called in-phase or **P**, and the imaginary part is called quadrature or **Q**. For each model, we compute the data $\mathbf{d} = [\mathbf{Q}_{\text{HCP}}, \mathbf{Q}_{\text{VCP}}, \mathbf{Q}_{\text{PRP}}, \mathbf{P}_{\text{HCP}}, \mathbf{P}_{\text{VCP}}, \mathbf{P}_{\text{PRP}}]$ for the combination of three different offsets, obtaining 18 data values. We then simulate the data measurements for a large range of possible electrical conductivities sampled on a logarithmic scale and possible thicknesses. Finally, the corresponding synthetic data are stored in the lookup table $\mathbf{D}_{\text{2-layers}}$ (see Table 3.1).

We proceed in the same manner, for an earth model with 3 layers, where the model parameters are given by $\mathbf{m} = [\sigma_1, \sigma_2, \sigma_3, h_1, h_2]$, with $\sigma_1, \sigma_2, \sigma_3$ being the electrical conductivities of the 3 layers, and h_1, h_2 being the thicknesses of the first layer and second layer (See table 3.1, $\mathbf{D}_{3-layers}$), the third layer is the rest of the halfspace.

GLOBAL SEARCH (GS)

After storing the pre-computed solutions in a lookup table, we perform a global search for the data acquired in each position. This search minimizes the misfit between the acquired data $\mathbf{d}_{\text{true}}$ and the data $\mathbf{d}_i$ stored in the lookup table **D**. The minimum misfit yields the index of the corresponding best estimate for the electrical conductivity model,

$$\mathbf{m}_i = \|\mathbf{d}_{\text{true}} - \mathbf{d}_i\|^2 \tag{3.3}$$

GAUSS-NEWTON INVERSION (GN)

The gradient-based optimization scheme uses the Gauss-Newton method to solve non-linear least square problems (Nocedal and Wright, 1999) to minimize the following objective function:

$$\Phi_{\mathbf{m}} = \|\mathbf{C}_d(\mathscr{F}(\mathbf{m}) - \mathbf{d})\|_2^2 + \alpha\|\mathbf{C}_m(\mathbf{m} - \mathbf{m}_0)\|_2^2, \tag{3.4}$$

where $\mathscr{F}(\mathbf{m})$ is the forward operator, $\mathbf{C}_d$ and $\mathbf{C}_m$ are the data weighting and model constraint weighting matrices, $\mathbf{m}_0$ is the initial model, and α is a regularization term. The Gauss-Newton scheme to minimize this equation updates the model $\Delta\mathbf{m}_k$ in the k^{th} iteration as follows:

$$(\mathbf{J}^T\mathbf{C}_d^T\mathbf{C}_d\mathbf{J} + \alpha\mathbf{C}_m^T\mathbf{C}_m)\Delta\mathbf{m}^k = \mathbf{J}^T\mathbf{C}_d^T\mathbf{C}_d(\Delta\mathbf{d}^k) - \alpha\mathbf{C}_m^T\mathbf{C}_m(\mathbf{m}^k - \mathbf{m}^0), \tag{3.5}$$

where $\mathbf{J} = \frac{\partial\mathscr{F}(\mathbf{m})}{\partial\mathbf{m}}$, $\Delta\mathbf{d}^k = \mathbf{d} - \mathscr{F}(\mathbf{m}^k)$. The model vector $\mathbf{m}$ is updated iteratively following:

$$\mathbf{m}^{k+1} = \mathbf{m}^k + \tau^k\Delta\mathbf{m}^k, \tag{3.6}$$

using a linear search parameter, τ, the superscript k indicates the iteration number. The linear search parameter τ is obtained by linear interpolation between the old and new model responses. This is solved using a conjugate-gradient least squares solver (Günther et al., 2006), implemented in the *pyGIMLi* package (Rücker et al., 2017).

Model performance was assessed using two commonly employed error measures: the root mean squared error (RMSE) to quantify the absolute deviation between predictions and reference values, and the normalized root mean squared error (NRMSE) to provide a scale-independent comparison:

$$\text{RMSE} = \sqrt{\frac{1}{n}\sum_{i=1}^{n}(y_i - \hat{y}_i)^2}, \tag{3.7}$$

$$\text{NRMSE} = \frac{\text{RMSE}}{y_{\max} - y_{\min}}, \tag{3.8}$$

where y_i represents the true/observed values, $\hat{y}_i$ represents the predicted/estimated values, n the number of samples, y_{max} and y_{min} denote the maximum and minimum values of the true values.

3.4. RESULTS AND DISCUSSION

We start by presenting the estimation of electrical conductivity models on several synthetic datasets of 1D FDEM measurements, where each measurement is at an x position, generating a 1D solution and combined to create a stitched 2D section. We generated the estimations using the GS and GN methods. These synthetic datasets were generated using the forward operator discussed in Section 3.2 (Equations 2.2). In the following analysis, we investigate for the 2-layered earth whether **P** and **Q** data are needed to find the correct estimations or if having only **Q** or **P** data is sufficient. Furthermore, we investigate whether the solution space is convex and contains a unique minimum. We apply this analysis to a 3-layered earth as well.

2-LAYERED EARTH

The estimation methods presented in Section 3.3 are used for predicting electrical conductivity models in eight numerical cases with different electrical conductivity contrasts (see Table 3.2). Each case uses twenty 1D synthetic earth models with the same conductivity values for both layers but with increasing thicknesses of the first layer, from 3.25 m to 5.15 m. These are noise-free tests. We present two main cases: A1) Top resistive layer, A2) Top conductive layer. It is important to note that while these models fall within the simulated ranges of the lookup table, the exact values are not included in it (See the ranges in Table 3.1). In the global search (GS) workflow, we found for each 1D model the corresponding model with the best data fit in the lookup table. The obtained models are compared with estimated models using the Gauss-Newton inversion (GN). For the GN method, an initial homogeneous model is set with $\boldsymbol{m}_0 = [3\text{ m}, 500\text{ mS/m}, 500\text{ mS/m}]$, and the regularization parameter is set to $\alpha = 0$.

The results for cases A1-3 and A2-3 are presented in Figures 3.1 and 3.2. In each case panel, the true 1D models are in the top row, the GS results are in the left column and the

Table 3.2: 2-layered earth numerical cases

	A1: Top resistive layer		A2: Top conductive layer	
Subcase	Top EC [mS/m]	Bottom EC [mS/m]	Top EC [mS/m]	Bottom EC [mS/m]
1	20	200	200	20
2	20	400	400	20
3	20	800	800	20
4	20	1600	1600	20

Table 3.3: RMSE table: 2-layered models

		Data: **Q** +**P**				Data: **Q**			Data: **P**		
Method	Case	RMSE σ [mS/m]	RMSE h [m]	RMSE **Q** [ppt]	RMSE **P** [ppt]	RMSE σ [mS/m]	RMSE h [m]	RMSE **Q** [ppt]	RMSE σ [mS/m]	RMSE h [m]	RMSE **P** [ppt]
Global search (GS)	A1-1	0.725	0.34	0.112	0.038	6.087	0.133	0.093	2.534	0.11	0.01
	A1-2	4.213	0.061	0.246	0.161	12.102	0.102	0.094	9.333	0.164	0.022
	A1-3	5.537	0.029	0.252	0.243	12.198	0.027	0.19	7.993	0.054	0.026
	A1-4	0.75	0.017	0.251	0.333	0.646	0.017	0.271	4.039	0.018	0.025
	A2-1	1.27	0.064	0.108	0.028	3.073	0.121	0.084	1.294	0.066	0.027
	A2-2	9.325	0.213	0.539	0.113	40.252	0.353	0.432	10.191	0.236	0.114
	A2-3	18.019	0.066	0.944	0.736	43.39	0.216	0.903	8.511	0.115	0.307
	A2-4	5.174	0.018	0.121	0.145	4.174	0.018	0.106	5.619	0.018	0.125
Gauss Newton (GN)	A1-2	0.035	0	0.013	0.003	0.172	0.003	0.004	2.359	0.076	0.005
	A1-2	0.016	0	0.005	0.002	0.009	0	0.003	8.781	0.165	0.009
	A1-3	0.014	0	0.004	0.002	0.037	0	0.003	16.612	0.125	0.024
	A1-4	0.027	0	0.007	0.003	0.022	0	0.006	88.015	0.257	0.14
	A2-1	0.003	0	0.001	0	965.09	3.788	5.582	0.042	0.001	0.004
	A2-2	0.181	0	0.022	0.03	657.04	3.603	9.151	1.353	0.032	0.023
	A2-3	0.382	0.001	0.018	0.05	51.979	0.264	0.8	1.942	0.019	0.031
	A2-4	1.012	0	0.045	0.102	5.301	0.019	0.105	3.648	0.01	0.088

GN results are in the right column. The relative difference of each result is in the third row, and in the fourth- and fifth rows, the **Q** and **P** data fit is shown. The models were estimated using both **P** and **Q** data values. For all A1 cases, the estimated models using both GS and GN methods show accurate results (see Table 3.3). The GN produces better results than the GS method because the lookup table was created with discrete steps, in which the true model is not included, giving only the best available model. However, for the A2 cases, both the GS and GN method shows a poor estimation of the bottom resistive layer, which worsens with increasing contrast in the electrical conductivity values and with greater thickness of the top conductive layer. Figures of the estimated results for all cases are presented in the Supplementary Material (Carrizo Mascarell et al., 2025).

In Figure 3.3 case A1-3 is estimated using the GS and GN methods described using either the **Q** or **P** component of the measurements only. The estimated models show good results for both methods. The results of case A1-3 show that when all data is used both GS and GN result in an accurate estimation of the lower conductive layer. Using only **Q** data values produces reasonably good estimates. Interestingly, with **Q**-data both layers are well estimated, whereas with the **P** data, the conductive layer is better estimated.

On the other hand, in Figure 3.4 for case A2-3, both GS and GN methods using **Q** data only produce poorer estimations, especially of the lower resistive layer. The estimation of the electrical conductivity of the resistive layer worsens with increasing contrast (see Table 3.3). Using **P** data only also describes better the upper conductive layer.

In both cases, it is clear that the data is more sensitive to the conductive layer than the resistive one. The results shown in this section indicate that **P** data is sensitive to

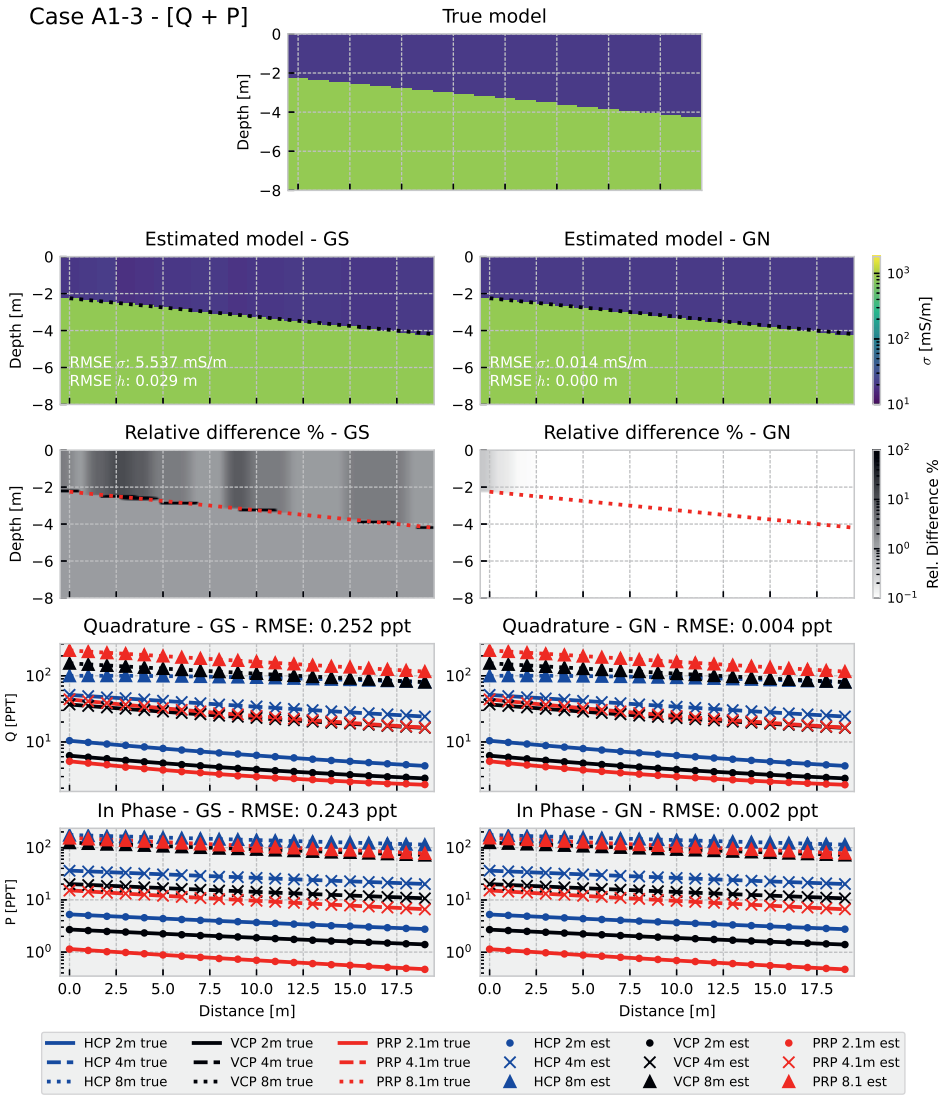


Figure 3.1: 2-layered earth model estimated using Q and P data. Case A1-3. Top row: true model. Left column: results using GS (Global search). Right column: results using GN (Gauss-Newton inversion) method. Third row: relative difference of the electrical conductivity of the estimated models. Fourth and fifth row: fit between the true and simulated data for the estimated models.

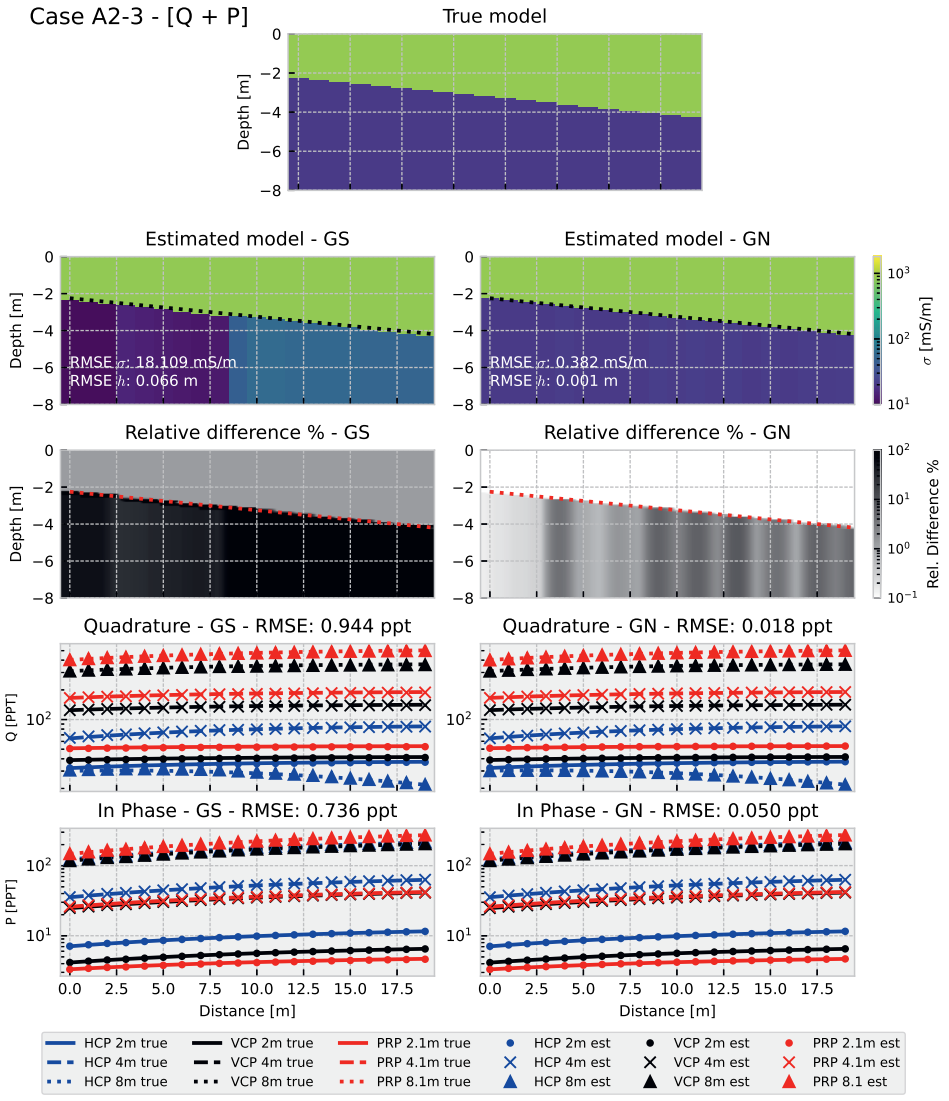


Figure 3.2: 2-layered earth model estimated using Q and P data. Case A2-3. Top row: true model. Left column: results using GS (Global search). Right column: results using GN (Gauss-Newton inversion) method. Third row: relative difference of the electrical conductivity of the estimated models. Fourth and fifth row: fit between the true and simulated data for the estimated models.

the conductivity of the model and combined with **Q** measurements produces better estimates in both the GS and GN than using **Q** data alone. It is clear then, that FDEM data is sensitive to the conductive layer and that using both **Q** and **P** increases the chance to better estimate the 2-layered model. These results will be further analyzed in section 3.4.

Apart from the instrument depth sensitivity, a thick conductive first layer attenuates the electromagnetic field more than a resistive first layer, and signal strength is important for deep targets. This can be seen in Figure 3.4 from the fact that neither method with **Q** or **P** data only cannot predict the conductivity of the lower resistive layer

SOLUTION SPACE ANALYSIS

To analyze the reasons behind the results in the previous section, we sample the solution space and study different cross-sections for the model in position $x = 10$ m, presented in Figures 3.5c and 3.6. In these figures, it is clear that in case A1-3 the GS and GN methods can find a unique minima. In case A2-3 the GN method is able to find the minima, but there is also a large area of the solution space that has very low NRMSE values which could present a problem when there is noise present in the data. This means that in cases where the subsurface has an upper conductive layer, finding the minima could depend on the data quality.

In A2 cases using **Q** data only for the estimations, we obtained poor results in examples A2-1 and A2-2. In Figure 3.6 we observe that the error space using **Q** data only has a saddle shape, which is also the case for cases A2-1 and A2-2 (see Supplementary Material (Carrizo Mascarell et al., 2025)). For this reason, depending on the initial model chosen the estimation might follow a path with a direction to a local minima instead of the true minima. This explains the inaccurate results seen in Figure 3.4.

In Figure 3.6 the solution space cross-sections for case A2-3 using **P** data only for the estimations. The cross-sections show that the solution space has a valley shape that allows the GN method to find the convex area where the true minima can be found. For this reason, we can obtain better estimations of an upper conductive 2-layered earth model using **P** data only. This suggests that **P** data is relevant and should be included in FDEM estimations. The **Q + P** cross-sections represent the combination of the overlapping of the **Q** and **P** cross-sections

NOISE ANALYSIS

FDEM measurements can be affected due to a low signal-to-noise ratio (Delefortrie et al., 2014). Therefore, we evaluate the performance of the methods against random noise. The random noise is created as in the following equation:

$$\tilde{\mathbf{d}} = \mathbf{d}(\mathbf{I} + \mathbf{N}\varepsilon) \tag{3.9}$$

where $\tilde{\mathbf{d}}$ is the noisy data, $\mathbf{I}$ is the identity matrix, $\mathbf{N}$ is a diagonal matrix of random values with a standard normal distribution of zero mean and unit standard deviation $\mathbf{N} = \text{diag}(\mathcal{N}(0,1))$, and ε is the error fraction.

In Figure 3.7 we observe the estimation with GS and GN methods of a 1D model using data with 10% random noise in 100 instances. For A1 cases the estimation results show a good estimation of the lower conductive layer and a larger variance in the conductivity and thickness of the upper resistive layer. The variance of the thickness decreases for

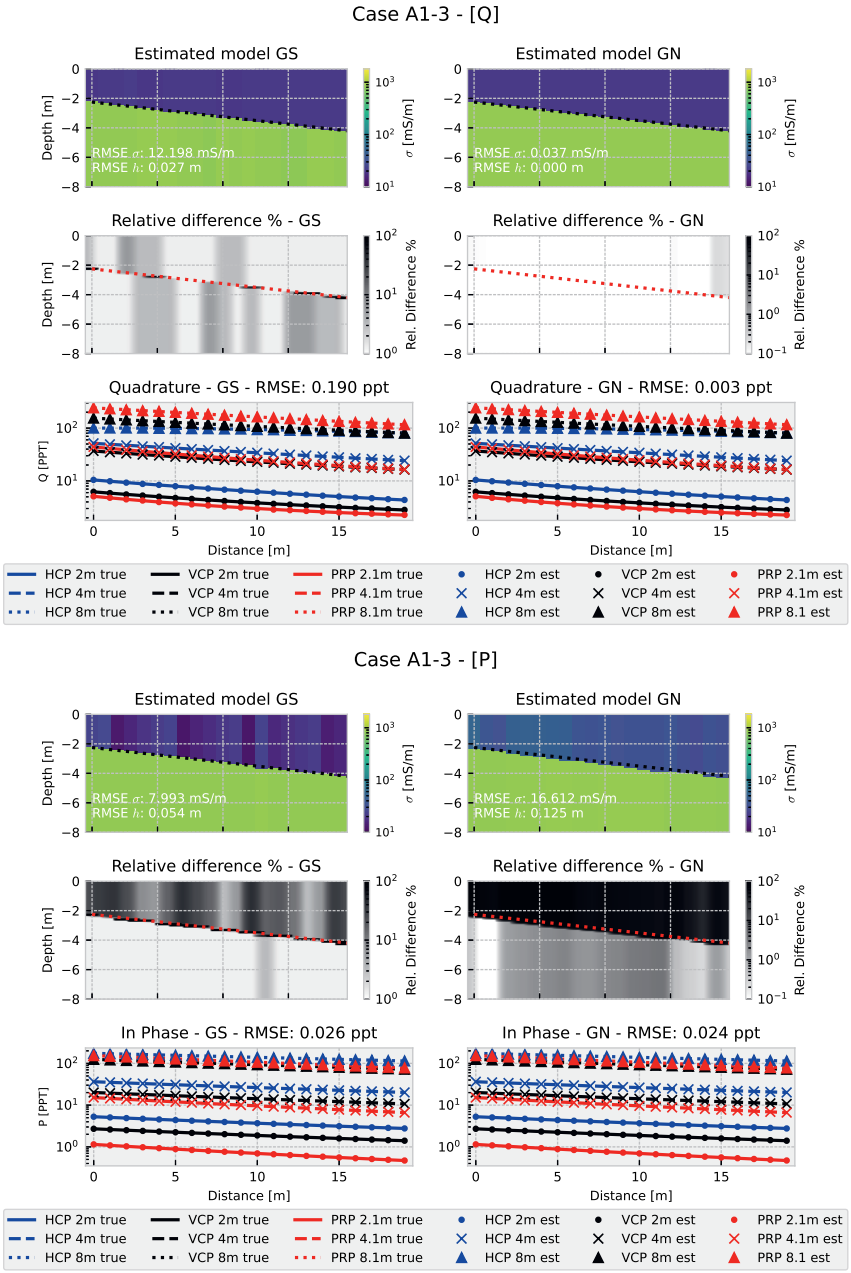


Figure 3.3: 2-layered models A1-3 estimated using **Q** component (top row) or **P** component only (bottom row)

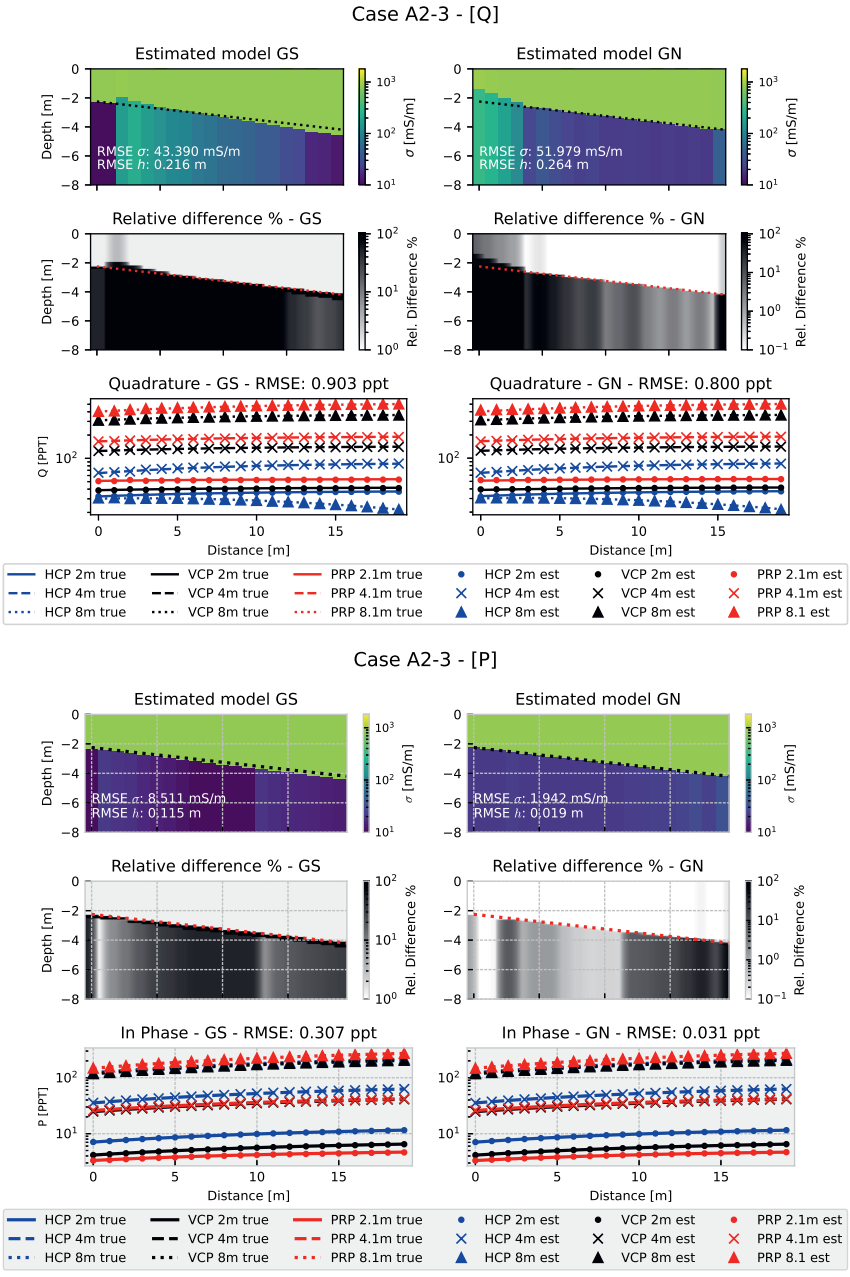
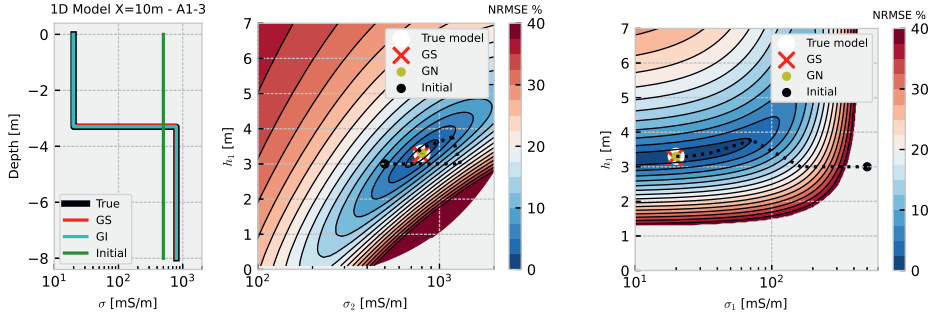
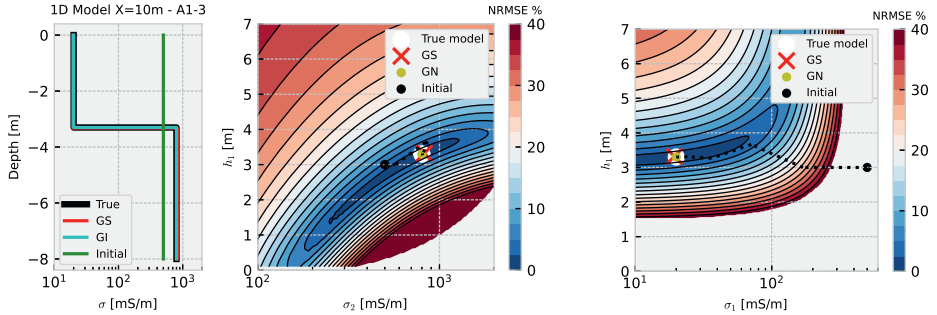


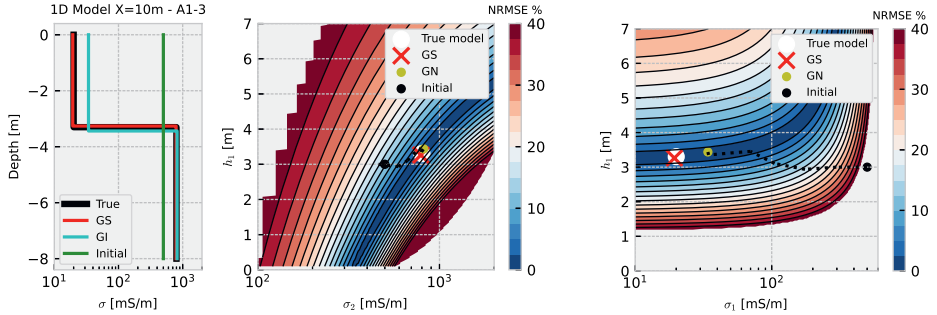
Figure 3.4: 2-layered models A2-3 estimated using **Q** component (top row) or **P** component only (bottom row)



(a) Error Space for $\mathbf{Q}+\mathbf{P}$.

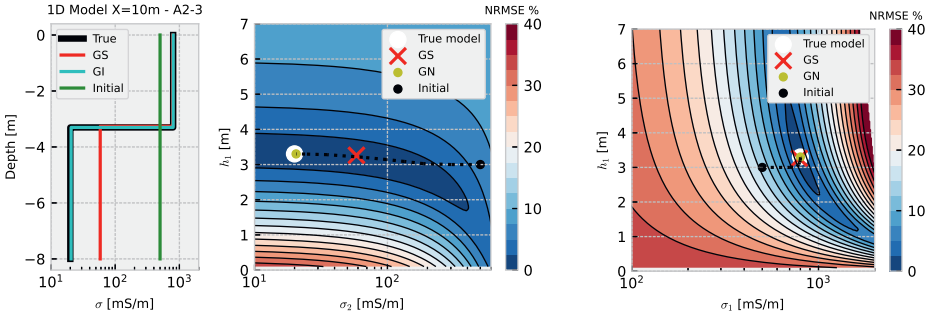


(b) Error Space for $\mathbf{Q}$.

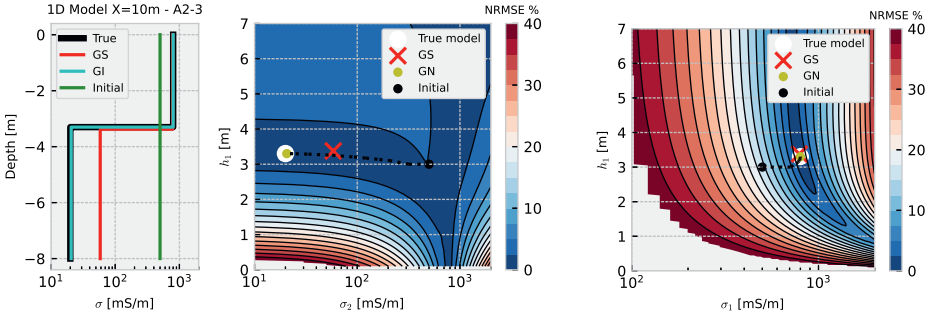


(c) Error Space for $\mathbf{P}$.

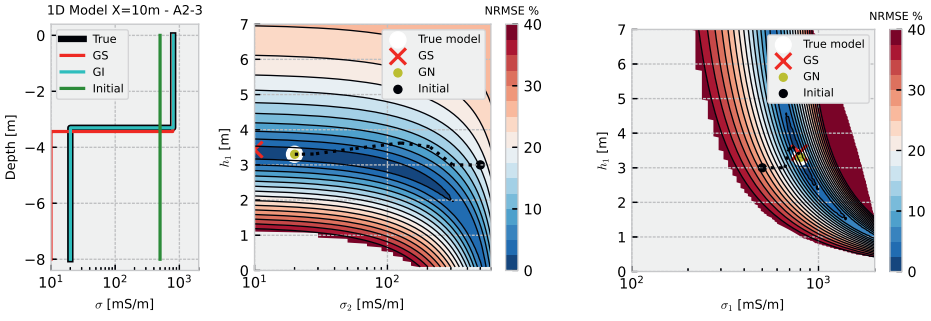
Figure 3.5: Cross-sections of the solution space for case A1-3. Top panel: using $\mathbf{Q}+\mathbf{P}$ data. Middle panel: $\mathbf{Q}$ data. Lower panel: $\mathbf{P}$ data. In each panel the estimated model is shown in the left column, the cross-section for fixed σ_1 to the estimated value in the middle column, and in the rightmost column the cross-section for a fixed σ_2 equal to the estimated value. In the cross-sections, the true model is indicated with a white dot which corresponds to the only minima present. The GS and GN methods can find the minima.



(a) Error Space for **Q** + **P**.



(b) Error Space for **Q**.



(c) Error Space for **P**.

Figure 3.6: ross-sections of the solution space for case A2-3. In the cross-sections, the true model is indicated with a white dot which corresponds to the minima in a wide area of small NRMSE. The GS estimated model falls close due to the true model not being contained in the lookup table sampled models, therefore estimating slightly different models to the true model

Table 3.4: 3-layered earth cases

	B1: Conductive middle layer		B2: Resistive middle layer	
Subcase	Background EC [mS/m]	Middle layer EC [mS/m]	Background EC [mS/m]	Middle layer EC [mS/m]
1	20	200	200	20
2	20	400	400	20
3	20	800	800	20
4	20	1600	1600	20

higher contrast in the electrical conductivity. For A2 cases the estimations cannot accurately describe the lower resistive layer using either the GS or GN method. The results worsen with increasing contrast in EC between the upper and lower layers. The variance of the conductivity values for the resistive layer ranges several orders of magnitude in the worst case (A2-4). This can be explained by looking at Figure 3.6 where a no-noise case can find the true minima using the GN method, but the solution space shows a wide low misfit valley where by adding only 10% of noise to the measurements the method finds very different models that can explain the data within the noise range. This means, that for an upper-conductive 2-layered earth model even when using both **Q** and **P** measurements, the model estimations might not be accurate depending on the noise levels.

A1 and A2 cases estimated with noisy data are shown in the Supplementary Material (Carrizo Mascarell et al., 2025). The RMSE increases for both estimation approaches for increasingly noisy data. The resulting 1D model estimations are worse for the case of the upper conductive layer (A2). The GS and the GN approach focus on solving the conductive part of the models.

3-LAYERED EARTH

We analyze a more complex inverse problem by increasing the number of model parameters to a 3-layered model and studying whether the inversion methods can reach a unique solution. We show the results of the estimations for the GS and GN methods using twenty 3-layered 1D earth models in a stitched 2D section. The estimations were carried out using both **Q** and **P** components in the measurements. We present eight cases: B1) Four conductive middle-layer cases in a resistive background. B2) Four resistive middle-layer cases in a conductive background. For all examples, the middle layer thickness increases from 1.5 m to 3.5 m (see Table 3.4). As in the previous case, while these models fall within the simulated ranges of the lookup table, the exact values are not included in it. For the Gauss-Newton inversion, an initial homogeneous model is set with $\mathbf{m}_0 = [3\,\text{m}, 3\,\text{m}, 100\,\text{mS/m}, 100\,\text{mS/m}, 100\,\text{mS/m}]$, and the regularization parameter $\alpha = 0$.

The results for the conductive middle layer case B1-3 and the resistive middle layer case B2-3 are presented in Figures 3.8 and 3.9. The RMSE values for all the cases are indicated in Table 3.5. All estimated models are shown in the Supplementary Material (Carrizo Mascarell et al., 2025). The GS and GN methods' performance differs in B1-3 and B2-3 cases. In case B1-3, the GS method can properly estimate the thickness and conductivity of the first and second layers. The estimation of the third layer, however, is the least accurate. On the other hand, the GN model predictions are quite poor.

For the B2-3 case, neither the GS nor the GN could predict the true models with suf-

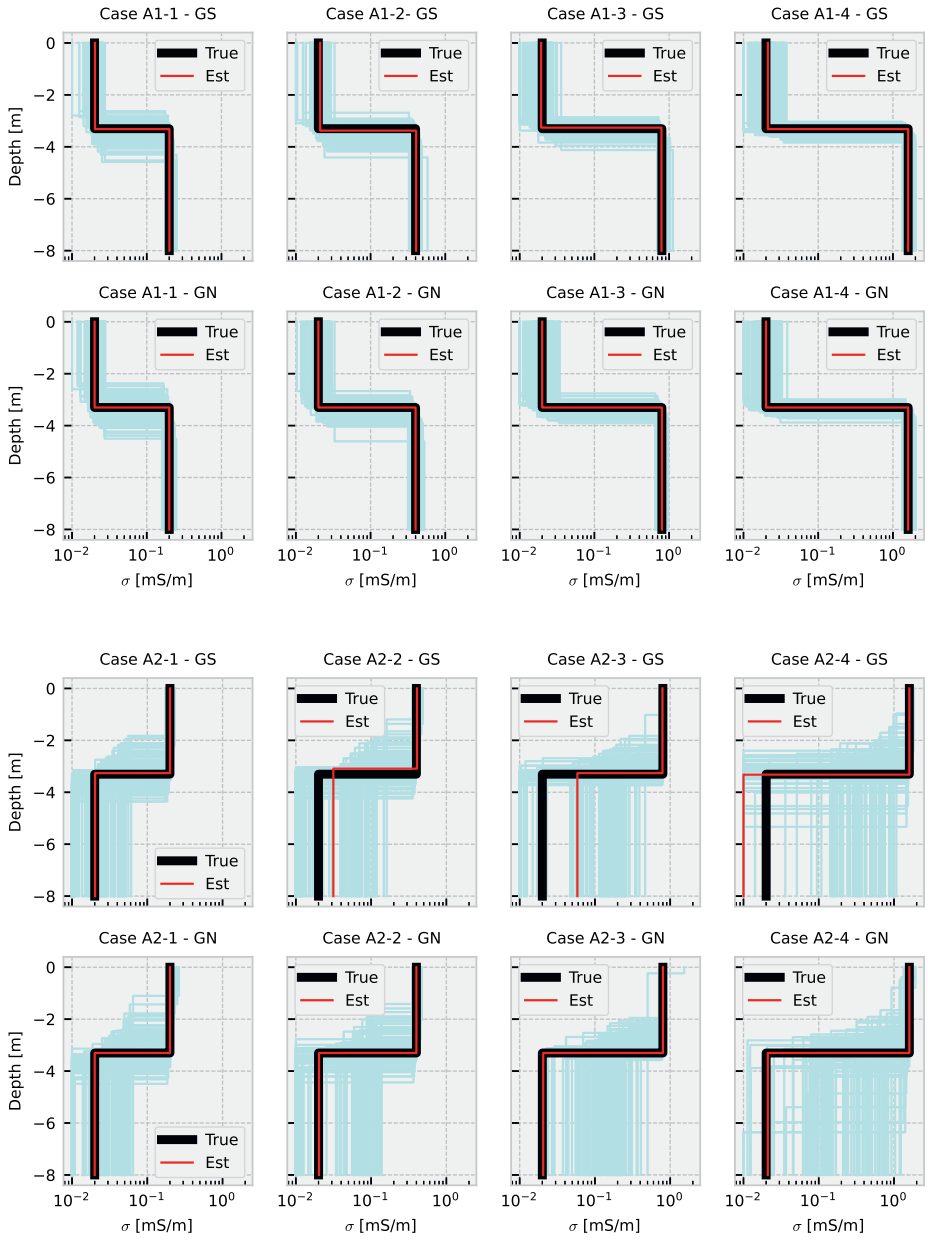


Figure 3.7: Results for the GS and GN method results using the data measurements for a 1D model with added 10 % random noise in 100 instances. The estimated models are presented in pale turquoise lines. The true and no-noise estimated models are presented in black and red lines, respectively. In A1 cases the results show a wider variance in the estimation of the top resistive layer. For A2 cases (top conductive) the results show that the bottom resistive layer varies widely. This suggests that the estimation problem in these cases is quite unstable due to noise presence in the data.

Table 3.5: RMSE table: 3-layered models

		Data: **Q** +**P**			
Method	Case	RMSE σ [mS/m]	RMSE h [m]	RMSE **Q** [ppt]	RMSE **P** [ppt]
Global search (GS)	B1-1	10.314	0.309	0.114	0.016
	B1-2	15.765	0.284	0.165	0.038
	B1-3	15.546	0.104	0.143	0.061
	B1-4	39.095	0.138	0.223	0.138
	B2-1	11.447	0.573	0.287	0.041
	B2-2	82.463	1.862	0.239	0.068
	B2-3	249.355	1.078	1.207	0.652
	B2-4	323.55	1.167	0.51	0.284
Gauss-Newton (GN)	B1-1	1.422	0.0488	0.01	0.003
	B1-2	10.197	0.069	0.04	0.027
	B1-3	275.136	1.285	28.048	10.953
	B1-4	916.156	1.316	27.269	15.034
	B2-1	21.324	0.677	0.034	0.011
	B2-2	15.013	0.134	0.038	0.01
	B2-3	479.202	0.793	39.046	29.249
	B2-4	666.667	1.585	145.819	68.717

ficient accuracy. Both the GS and GN could predict the conductivity of the first layer, and the thickness of the first layer for some positions. However, the resistive body is not well determined in conductivity or thickness. These results will be better explained in the following sections.

INITIAL MODEL $\mathbf{m}_0$

Using the GN estimation method, we must choose an initial model $\mathbf{m}_0$ to initialize the minimization of Equation 3.4. Depending on the shape of the error space, the choice of $\mathbf{m}_0$ might affect the resulting estimation, as was shown in Figure 3.6 for the A2 case using **Q** data only. In Figure 3.10 we show the estimated models for the position x = 10 m in case B1-3 using different initial models $\mathbf{m}_0$. From these results, it is clear that the estimated models differ greatly depending on the initial model. This indicates that estimating a 1D 3-layered model using **Q** and **P** measurements might not be feasible.

SOLUTION SPACE ANALYSIS

When increasing the number of layers from 2 to 3 we find that both the GS and GN schemes have trouble estimating the 1D models. To explain this better, let us focus on Figure 3.11 where we study the 1D model in position x = 10 m of the 3-layered case B1-3. In the figure, the left panel contains the true and estimated 1D model, and the right panel shows a 3D cloud of points of the solution space (corresponding to the solutions computed in the lookup table). In the solution space cloud, the low **NRMSE** values correspond to a large volume, with models from wide ranges of different thicknesses and electrical conductivities. The path taken by the GN method shows that the minimization is trapped in a local minimum far from the true solution. From this analysis above, there are two main insights: First, different 3-layered earth models can explain the measurements within a small error range, translating into an unstable solution. Second, depending on the initial model the path taken by the GN method might differ and thus, result in very different estimations of the earth models.

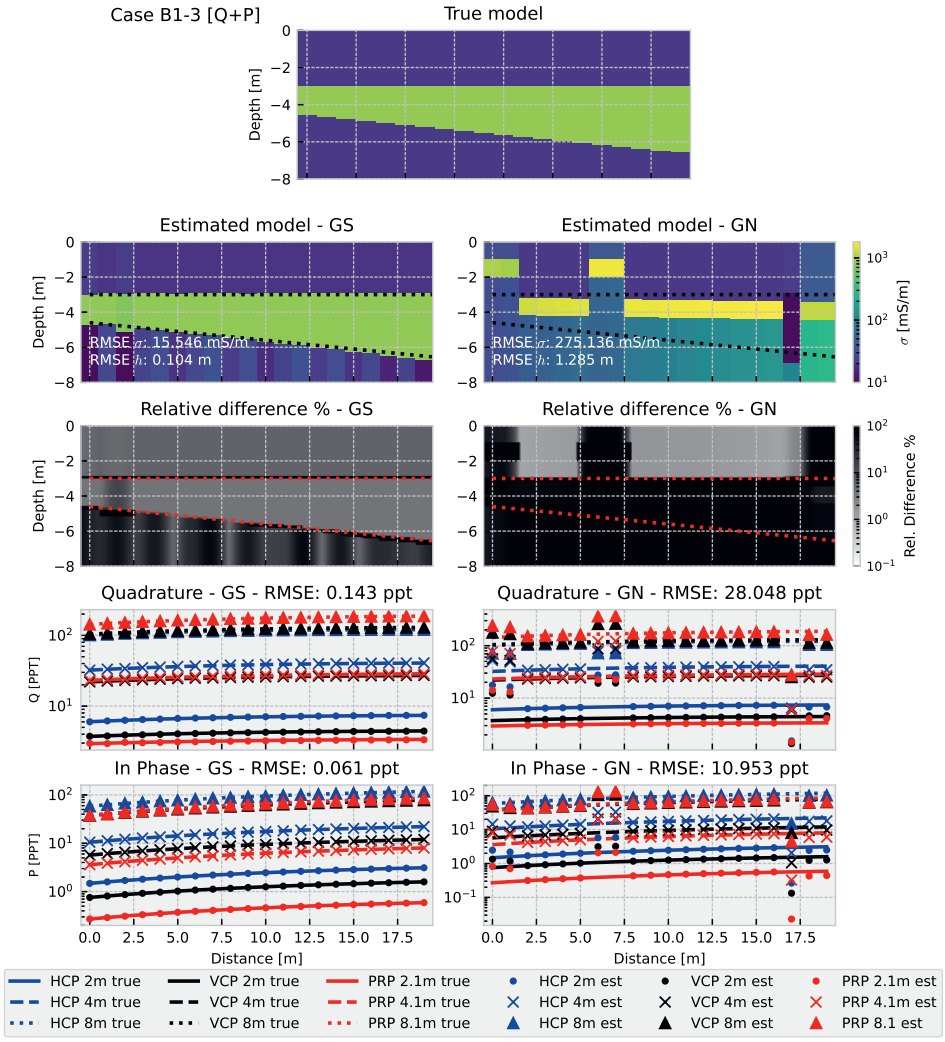


Figure 3.8: 3-layered earth: Models estimated using Q and P data. Top row: true model. Left column: results using GS. Right column: results using GN. Third row: relative difference of the estimated models. Fourth and fifth row: fit between the true and simulated data.

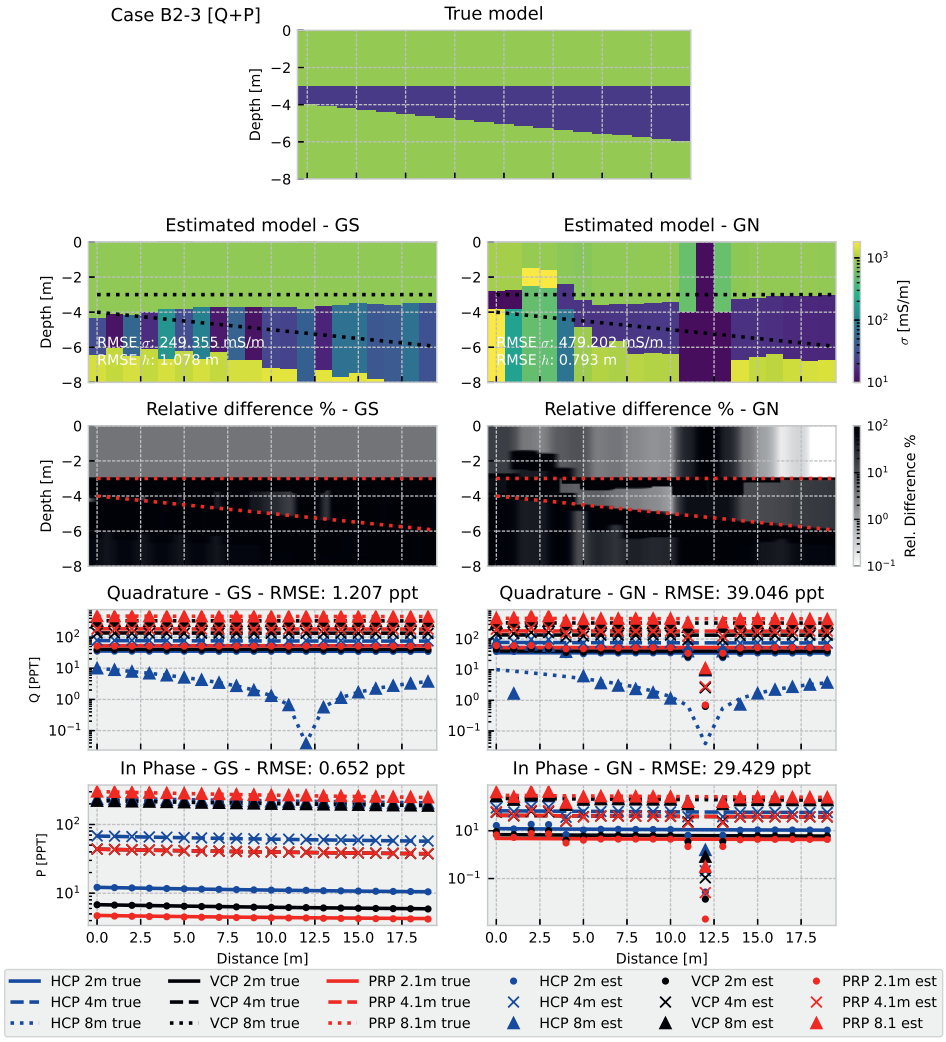


Figure 3.9: 3-layered earth: Models estimated using Q and P data. Top row: true model. Left column: results using GS. Right column: results using GN. Third row: relative difference of the estimated models. Fourth and fifth row: fit between the true and simulated data.

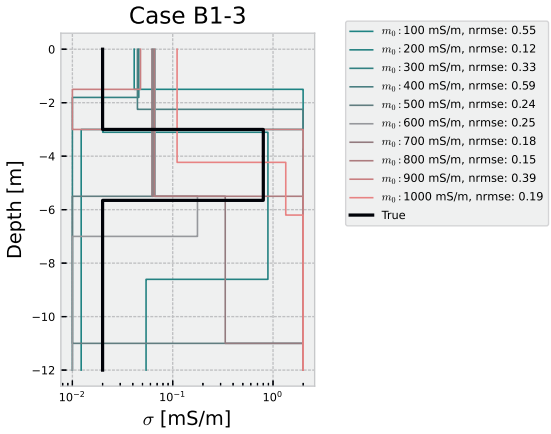


Figure 3.10: Estimation of a 1D 3-layered earth models in case B1-3 using GN method with different m_0

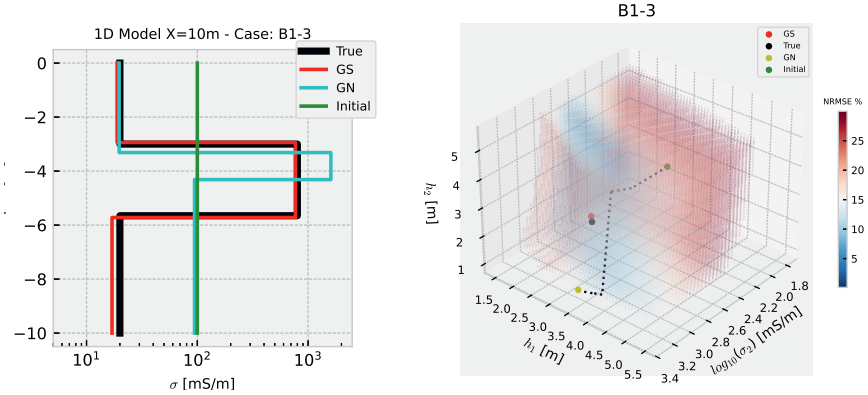


Figure 3.11: In the left panel, the true and estimated 3-layered 1D models for cases B1-3 are shown. In the right panel, the solution space cloud points corresponding to the position $x = 10$ m in case B1-3 is shown. The true model in the 3D plot is a black dot, and the GS estimated model is a red dot. The initial model for GN is a green dot, the path of the model updates is a dotted black line, and the final GN estimated model is a yellow dot.

Table 3.6: Computing parameters of the GS method for increasing n number of layers using 8 processors

n number of layers	Parameters	Samples per parameter	Number of pre-computed measurements	Time to compute measurements	Memory resources	Time to estimate 1 model
2	3	121	1,771,561	57 seconds	230 Megabytes	0.24 seconds
3	5	51	345,025,251	3.08 hours	45 Gigabytes	48 seconds

LIMITATIONS OF THE METHODS

The GN method is usually applied to estimate earth models with this type of electromagnetic measurement. However, as we have seen in the previous results, in a 2-layered earth for the configuration of the instrument described, it is necessary to use both **Q** and **P** measurements, which are not available in some instruments already existent in the industry. Additionally, for a 3-layered case, even with the **Q** and **P** components available, the success while using this method depends highly on the initial model chosen. Moreover, many possible models that differ greatly from each other explain the data within a 5% **NRMSE** of the measurements, which makes the solution to this inversion problem quite unstable.

On the other side, the GS method for a 2-layered earth can determine an acceptable estimate, depending on how many models are pre-computed and whether the ranges of the variables contain the true earth model. However, for a 3-layered earth, the GS is only moderately successful for a middle conductive layered earth. Due to memory limitations (see Table 3.6), the variable sampling ranges of the pre-computed models are coarser for a 3-layered case, which translates to less accurate estimations. In the middle resistive case, the estimations worsen, due to the low sensitivity of the instrument to resistive bodies under a conductive layer.

In the following section, we analyse the benefit of using the GS method as a previous step of the GN method to increase the chance of success in estimating 3-layered earth models.

GLOBAL SEARCH + GAUSS-NEWTON

The previous results showed that for a 3-layered earth, the GN method is limited by the initial model. If there is no previous knowledge of the subsurface, the GN method estimation could be very far from the true subsurface. We study if for such a case using the GS method to obtain an initial estimate could be beneficial. The method begins by doing a global search in the pre-computed solutions present in the lookup table obtaining a 1D estimated model. Afterward, this estimated model can be used as the initial model $\mathbf{m}_0$ in the Gauss-Newton inversion, providing a better opportunity for the minimization to reach the appropriate minima in the error space. In Figure 3.12 the results of the two previous estimation methodologies and the new combination of GS and GN for the 3-layered earth numerical examples are shown. In both cases B1-3 and B2-3, we can see that for some 1D models, there is a slight improvement in the detection of the middle layer and the **RMSE** decreases. For the resistive middle layer cases (B2-3), there is an improvement, however, the estimates still differ from the true models. This brings out the point that the GN method is still in some cases unable to find the true solution for 3-layered cases. Moreover, the GS method also cannot always find the proper solution

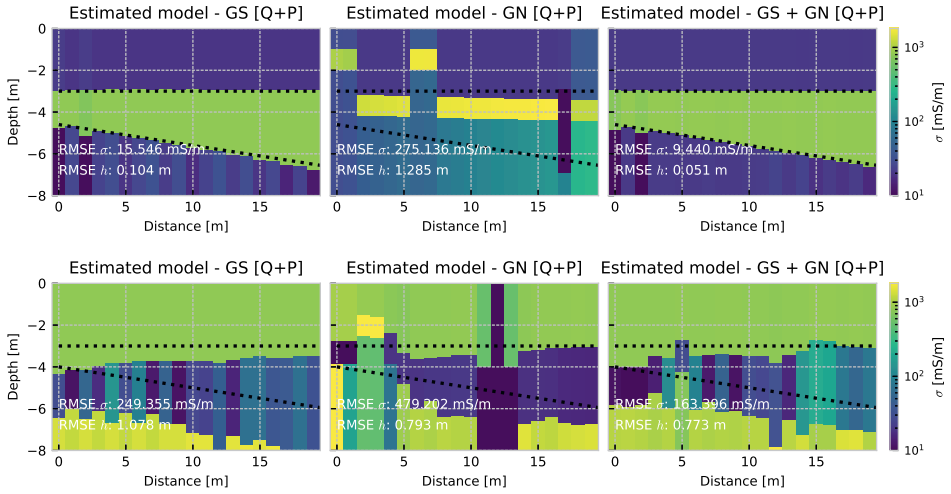


Figure 3.12: Global search + Gauss Newton results. Top row: B1-3 case (middle conductive layer). Bottom row: B2-3 case (middle resistive layer). The GS method estimates are in the left column, the GN estimates in the middle column and the combined algorithm results in the right column.

due to several models satisfying a certain data misfit criterion, then the GN method cannot be expected to improve the estimation further. This further suggests that such data cannot be used for 3-layered model estimation without prior information.

FIELD DATA CASE

We use an electromagnetic induction dataset acquired in Ackerdijkse Plassen, The Netherlands (see Figure 2.10) containing 1850 measurements. The dataset is pre-processed removing noisy spikes. Following the instrument developer's recommendations, we do not use the **P** measurements for offsets under 4 meters in the estimations (Taylor, 2023). We use only the HCP and VCP loop-loop configurations. We assume the area to have a 2-layered shallow subsurface (up to 10 meters depth) based on lithology samples taken from nearby boreholes.

We carry out 2-layered 1D model estimations from the field measurements using the two approaches: global search (GS) and Gauss-Newton (GN) inversion. In Figure 3.13 three cross-sections from each estimation methodology are shown. In the first column are the results from the GS method, and in the second column are the results from the GN approach. These cross-sections show that the area holds a top resistive layer with values around 60 mS/m, with a maximum thickness of 6 meters, and a bottom conductive layer with values around 120 mS/m. Both methods show similar results. There are differences in the thickness of the first layer in a topographic low where a water stream is present in the field. This is better observed in the maps in Figure 3.14 where the estimated model parameters are shown in the area.

From Figure 3.14 we can see that the distribution of the electrical conductivity and thicknesses generally does not show great changes in the different methods. The top

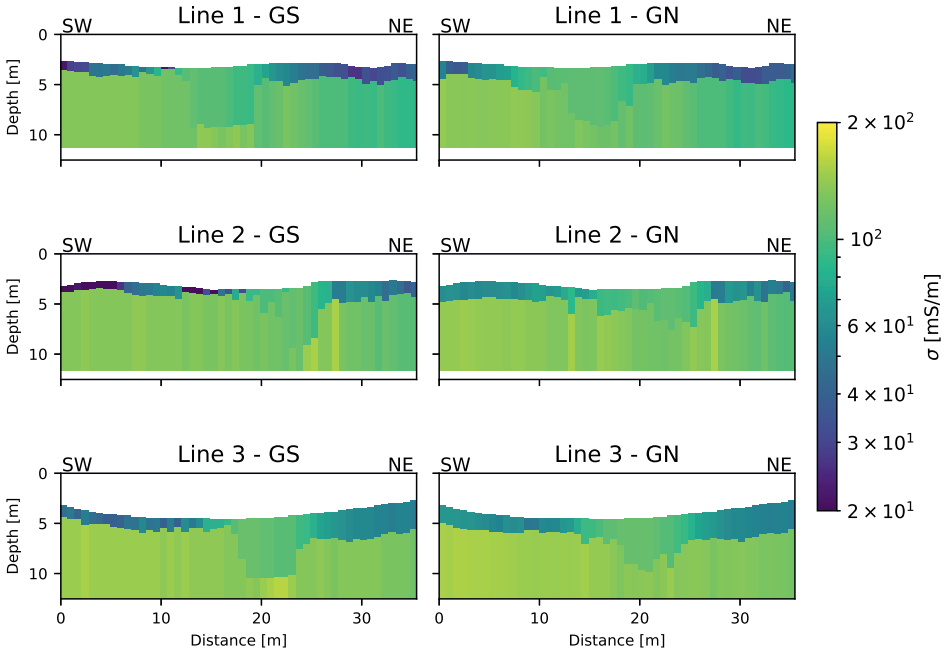


Figure 3.13: Cross-sections of estimated models. The estimations show a top resistive layer above a conductive layer. The top layer increases in conductivity around the stream feature present in the satellite image

layer resistivity shows higher conductivity values above the stream feature. The thickness maps show a thickness increase above the stream feature. The misfit **RMSE** between true and simulated data for all measurements acquired is 2.29 ppt and 1.79 ppt for the GS and GN methods, respectively. We can see a slight improvement using the Gauss-Newton inversion methodology, however, the difference is marginal. Therefore, we can deduce that for this 2-layered field case, either method can be used and will reach a satisfactory outcome.

3.5. CONCLUSIONS

In this study, we evaluate the well-posedness of the inverse problem in estimating two-layered and three-layered 1D earth models using multi-coil single-frequency rigid-boom electromagnetic induction measurements. This analysis is carried out using a global search through lookup tables and a Gauss-Newton inversion scheme.

We showed that for a two-layered model, a Gauss-Newton approach is sufficient to find the minimum misfit and estimate the model only when using both quadrature and in-phase data components. Adding the in-phase part to the quadrature part of the measurements increases the amount of information about the subsurface and produces a convex solution space for two-layered earth models. Hence, the inverse problem is well-posed in this case. Moreover, we show the solution is quite stable under the influence of

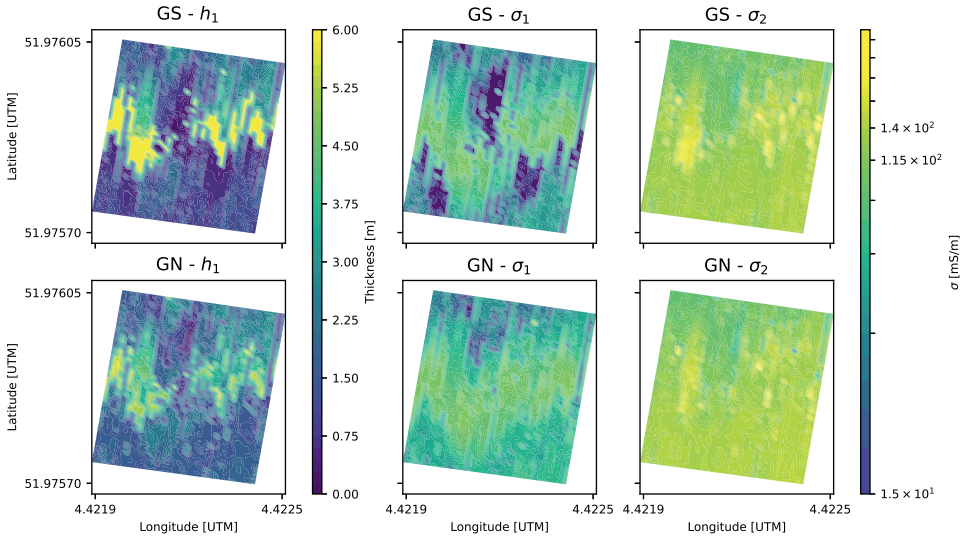


Figure 3.14: Maps of estimated models. Left column: Thickness of first layer (h_1). Middle column: electrical conductivity of first layer (σ_1). Right column: Electrical conductivity of the second layer (σ_2).

noise, except when the upper layer is more conductive than the lower halfspace.

On the other hand, already for a three-layered noise-free numerical model, the Gauss-Newton method is not able to find the correct model, except when the initial estimate is close to the correct model. This is due to the shape of the solution space, which is rather flat close to the true minimum, and it has multiple local minima where the optimization might get trapped. This suggests that the problem is ill-posed for a three-layered earth due to the solution's non-uniqueness. The global search method might provide better estimations given a sufficient sampling of the pre-computed models in the middle conductive layered earth. Nonetheless, neither method can describe the subsurface precisely for a middle resistive layered earth.

Additionally, we tested an alternative inversion scheme that combines a global search to get an initial estimate before the Gauss-Newton inversion to improve the model estimate through a local search. The scheme was applied to synthetic cases, where the middle resistive layered cases showed little improvement. For finite precision data, the global search cannot improve in reaching the true model because a local minimum can have the same or smaller misfit value than the true solution. This emphasizes the point that the data available for the instrument configuration used in this study are insufficient to uniquely and precisely determine a three-layered 1D earth model without prior knowledge of the subsurface.

Finally, the application of both inversion approaches to field data produced consistent results. As predicted by the numerical experiments, the two-layered case yields a unique and stable solution.

DATA AVAILABILITY

The codes and data used in this chapter is available via 4TU.ResearchData (Link).

BIBLIOGRAPHY

Beamish, D. (2011). Low induction number, ground conductivity meters: A correction procedure in the absence of magnetic effects. *Journal of Applied Geophysics*, *75*(2), 244–253. https://doi.org/10.1016/j.jappgeo.2011.07.005

Carrizo Mascarell, M., Werthmüller, D., & Slob, E. (2025). Supplementary material: Additional results. https://doi.org/10.5281/zenodo.17662459

Deleersnyder, W., Maveau, B., Hermans, T., & Dudal, D. (2020). Inversion of electromagnetic induction data using a novel wavelet-based and scale-dependent regularization term. *Geophysical Journal International*, *226*(3), 1715–1729. https://doi.org/10.1093/gji/ggab182

Delefortrie, S., Saey, T., Van De Vijver, E., De Smedt, P., Missiaen, T., Demerre, I., & Van Meirvenne, M. (2014). Frequency domain electromagnetic induction survey in the intertidal zone: Limitations of low-induction-number and depth of exploration. *Journal of Applied Geophysics*, *100*, 14–22. https://doi.org/10.1016/j.jappgeo.2013.10.005

Delrue, S., Maveau, B., & Dudal, D. (2020). A damped forward EMI model for a horizontally stratified earth. *Exploration Geophysics*, *51*(4), 422–433. https://doi.org/10.1080/08123985.2019.1708717

de Oliveira, L. A., Woodbury, B. L., de Miranda, J. H., & Stromer, B. S. (2020). Using electromagnetic induction technology to identify atrazine leaching potential at field scale. *Geoderma*, *375*. https://doi.org/10.1016/j.geoderma.2020.114525

Günther, T., Rücker, C., & Spitzer, K. (2006). Three-dimensional modelling and inversion of dc resistivity data incorporating topography — II. Inversion. *Geophysical Journal International*, *166*(2), 506–517. https://doi.org/10.1111/j.1365-246X.2006.03011.x

Kiflai, M. E., & Whitman, D. (2023). Geophysical mapping of freshwater lens in Big Pine Key, Florida: electromagnetic induction calibration and application. *Near Surface Geophysics*, *21*(2), 152–167. https://doi.org/10.1002/nsg.12244

Klose, T., Guillemoteau, J., Vignoli, G., & Tronicke, J. (2022). Laterally constrained inversion (LCI) of multi-configuration EMI data with tunable sharpness. *Journal of Applied Geophysics*, *196*, 104519. https://doi.org/10.1016/j.jappgeo.2021.104519

Moghadas, D., & Christiansen, A. V. (2020). Soil electrical conductivity imaging using a neural network-based forward solver: Applied to large-scale Bayesian electromagnetic inversion. *Journal of Applied Geophysics*, *176*, 104012. https://doi.org/10.1016/j.jappgeo.2020.104012

Monteiro Santos, F. A., Triantafilis, J., & Bruzgulis, K. (2011). A spatially constrained 1D inversion algorithm for quasi-3D conductivity imaging: Application to DUALEM-421 data collected in a riverine plain. *Geophysics*, *76*(2), B43–B53. https://doi.org/10.1190/1.3537834

Nocedal, J., & Wright, S. J. (1999). Nonlinear least-squares problems. *Numerical Optimization*, 250–275. https://doi.org/10.1007/0-387-22742-3_10

Rücker, C., Günther, T., & Wagner, F. M. (2017). pyGIMLi: An open-source library for modelling and inversion in geophysics. *Computers and Geosciences*, *109*, 106–123. https://doi.org/10.1016/j.cageo.2017.07.011

Taylor, R. (2023, April). Website of DualEM manufacturer: EM Induction (accessed on 21/04/2023). Retrieved April 21, 2023, from https://dualem.com/documents/em-induction/

Thiesson, J., Tabbagh, A., Dabas, M., & Chevalier, A. (2018). Characterization of buried cables and pipes using electromagnetic induction loop-loop frequency-domain devices. *Geophysics*, *83*(1), E1–E10. https://doi.org/10.1190/geo2016-0476.1

Wait, J. R. (1982, January). Chapter III - Electromagnetic Induction and Loop–Loop Coupling. In J. R. Wait (Ed.), *Geo-Electromagnetism* (pp. 101–139). Academic Press. https://doi.org/10.1016/B978-0-12-730880-7.50007-7

Ward, S. H., & Hohmann, G. W. (1987). 4. Electromagnetic Theory for Geophysical Applications. *Electromagnetic Methods in Applied Geophysics: Volume 1, Theory*, 130–311.

Werthmüller, D., Key, K., & Slob, E. (2019). A tool for designing digital filters for the Hankel and Fourier transforms in potential, diffusive, and wavefield modeling. *Geophysics*, *84*(2), F47–F56. https://doi.org/10.1190/geo2018-0069.1

4

IMPACT OF 3D DISTRIBUTION OF ELECTRICAL CONDUCTIVITY

An experiment is a question which science poses to Nature and a measurement is the recording of Nature's answer.

Michael Faraday

Subsurface electrical conductivity models estimated from FDEM measurements are often derived using computationally efficient one-dimensional piecewise inversion (PWI) approaches. However, PWI does not account for lateral conductivity variations or the measurement overlap between adjacent soundings, which can limit model estimation accuracy. Laterally constrained inversion (LCI) introduces smoothness constraints to reduce lateral variability between neighboring models, potentially improving continuity. In this study, both PWI and LCI use a 1D forward function, assuming a horizontally layered earth, and a horizontally laying rigid boom instrument, to perform the estimations. This study presents a detailed analysis of how various 2.5D and 3D conductivity distributions, including topographic variations and instrument pitch angle, affect FDEM measurements. We examine how these measurement distortions propagate into PWI and LCI inversion results. Under ideal conditions, such as flat terrain, no instrument tilt, and simple two-layer models, both methods recover accurate conductivity structures, with LCI offering little advantage in accuracy. When topography is introduced, however, distortions occur even at slopes as small as 2°, and both methods show degraded performance, particularly in 3D scenarios. In the field example, LCI produces smoother and more stable results than PWI in the presence of noise, but its assumption of lateral smoothness can be restrictive in geologically complex settings. Our findings demonstrate that both inversion strategies are sensitive to topographic and 3D effects, and that error propagation has a significant influence on inversion reliability. These results highlight the need for improved methodologies capable of handling realistic acquisition conditions and measurement uncertainties in FDEM surveys.

4.1. INTRODUCTION

Ground-based frequency domain electromagnetic (FDEM) induction soundings with loop-loop configurations are commonly used for mapping electric conductivity inside the subsurface. Electrical conductivity models estimated with this geophysical measurement are used in various applications, such as geologic mapping, mining, water exploration, precision farming, and archeology. Single-frequency, multi-configuration sensors can simultaneously measure different volumes of subsurface investigation. The resulting measurements are commonly used to image the subsurface through data inversion.

It has been suggested with numerical examples that for a 2-layered horizontal subsurface, the inversion problem is unique for a specific instrument configuration (see Chapter 3). This allows for the estimation of electrical conductivity models from loop-loop configuration FDEM measurements using a 1D piecewise layered medium approach, as they are computationally easy to solve (Heagy et al., 2017, Kiyan et al., 2022, McLachlan et al., 2021). However, FDEM measurements are influenced by a volume of the subsurface that contains lateral and vertical variations in three dimensions. This might present a limitation for an accurate representation of the true distribution of the electrical conductivity of the subsurface. Moreover, the piecewise 1D approach presents a lack of continuity between adjacent soundings when, in reality, there is an overlap of the subsurface volumes that are influencing the measurements.

A way to tackle the lack of continuity between 1D estimations is to introduce prior information through smoothness constraints, to limit the variability between the parameter values characterizing the adjacent 1D models (Constable et al., 1987). This inversion method is called Laterally Constrained Inversion (LCI), see, e.g., Auken and Christiansen (2004). Some examples of FDEM data are shown in Monteiro Santos (2004), Christiansen et al. (2016) and Klose et al. (2022).

Previous studies have mentioned the limitations of the PWI and LCI methods in reproducing 2D and 3D structures, since they rely on 1D forward modelling (Ley-Cooper et al., 2010, Silic et al., 2015). Several corrective approaches have been proposed to address these issues (Bai et al., 2021, Deleersnyder et al., 2022). Moreover, full 3D inversion of electromagnetic measurements has also been subject to research in the past decade (Alumbaugh and Newman, 2000, Oldenburg et al., 2020, Zhang et al., 2021). However, it requires a significant amount of computational resources that can be prohibitive.

In this study, we investigate how different forms of three-dimensional variability in subsurface electrical conductivity affect FDEM measurements. Our goal is to determine to what extent the 1D forward model is sufficient to reproduce measurements in 2.5D/3D earth models. To this end, we demonstrate how the differences in the measurements impact the accuracy of PWI and LCI inversion results in noise-free conditions, where 1D forward modelling assumptions are considered. To better approximate field conditions, we simulate dipping interfaces, instrument pitch angle, and realistic topog-

This chapter was published as M. Carrizo Mascarell, D. Werthmüller, and E. Slob, *Impact of non-1D Earth on FDEM measurements and the performance of PWI and LCI Inversions*, Journal of Applied Geophysics **2026**, 106130 (247). Minor modifications have been applied to the text and figures for thesis consistency.

raphy, where the instrument follows the slope of the air–subsurface interface. We then evaluate how these effects influence model estimations in a series of numerical examples, culminating in a discussion of the results and their implications for field surveys.

4.2. METHODOLOGY

In this section, we describe the methodologies used to invert electrical conductivity models using FDEM measurements. We compare the results of two inversion methodologies: Piecewise 1D Inversion (PWI) and Laterally Constrained Inversion (LCI). Both inversion methods use 1D horizontally layered forward modelling described in the following section.

FORWARD MODELLING

For the 1D forward modeling, used in the PWI and LCI inversion methods, we assume a horizontally layered medium and use the wavenumber-frequency formulation given by Wait (1982). We use a digital linear filter provided by Werthmüller (2017) for the Hankel transform to the space-frequency domain. We make two key assumptions: (1) The medium is horizontally layered. (2) The instrument coils are positioned at the same height (meaning pitch angle zero). These assumptions are presented as Case (a) in Figure 4.2. Moreover, we used a 3D forward modeling scheme to simulate the data for the numerical examples in which the 1D assumptions do not hold, in order to realistically assess the impact of violating these assumptions. The scheme was created with the open source package *emg3d* presented in Werthmüller et al. (2019).

PIECEWISE 1D INVERSION (PWI)

In the PWI method, we estimate each sounding location separately (see Figure 4.1). FDEM measurements are inverted using the Gauss-Newton optimization presented by Günther et al. (2006) and implemented in the *pyGIMLi* package (Rücker et al., 2017) as described in Chapter 3. This inversion uses internally the 1D forward modeling mentioned in Section 4.2.

LATERALLY CONSTRAINED INVERSION (LCI)

We carry out the LCI using the method introduced by Auken et al. (2005) and presented for FDEM measurements on a 2-layered earth, the first layer with thickness h_1, and the second layer being the rest of the halfspace. The LCI produces a simultaneous inversion of adjacent sounding locations to obtain quasi-layered subsurface models (see Figure 4.1). The basic assumption of the LCI concept is that the lateral constraints are considered prior information on the spatial variability in the area. Lateral continuity is imposed, regularizing the inverse problem by constraining neighboring model parameters. We implement the previously mentioned Gauss-Newton optimizer, also used for the LCI method by Thalhammer (2022). This inversion also uses the 1D forward model mentioned for PWI.

The objective function is expressed by Auken and Christiansen, 2004 as

$$\Phi_{\boldsymbol{m}} = \|\boldsymbol{C}_{\mathrm{d}}(\mathscr{F}(\mathbf{m}) - \mathbf{d})\|_2^2 + \alpha\|\mathbf{R}\mathbf{C}_{\mathrm{m}}(\mathbf{m} - \mathbf{m}_0)\|_2^2, \tag{4.1}$$

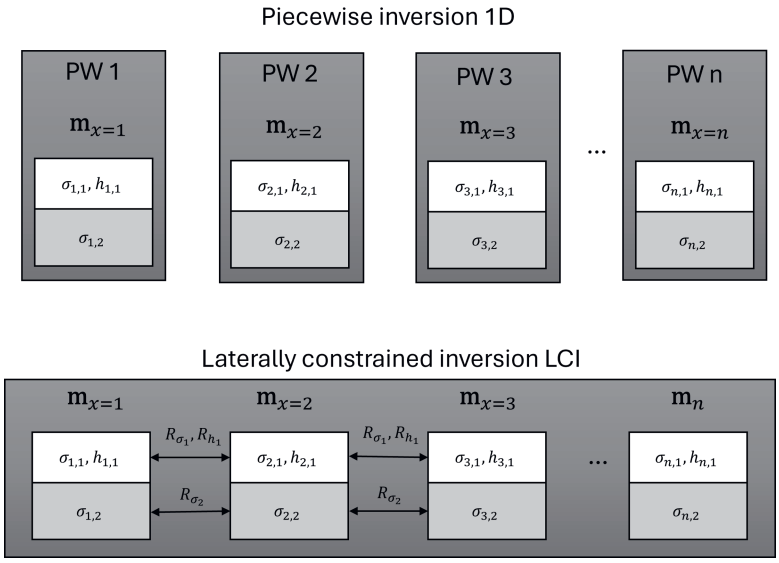


Figure 4.1: Inversion methods: In the PWI method, each sounding position x is estimated separately. In the LCI method, all of the models are inverted simultaneously using spatial constraints between adjacent models **R**. Modified from Auken et al. (2005)

where $\mathscr{F}(\mathbf{m})$ is the forward operator, $\mathbf{C}_d$ and $\mathbf{C}_m$ are the data weighting and model constraint weighting matrices, $\mathbf{m}_0$ is the initial model, and α is a regularization term. The roughening matrix **R** applies the lateral constraints as

$$\mathbf{R}\delta\mathbf{m} = \delta\mathbf{r} + \mathbf{e}_\mathrm{r}, \tag{4.2}$$

where $\mathbf{e}_\mathrm{r}$ represents the error on the constraints, $\delta\mathbf{r}$ the identity between parameters linked by constraints, and $\delta\mathbf{m} = \mathbf{m} - \mathbf{m}_0$. The roughening matrix **R**, defined by Auken and Christiansen, 2004, is sparse, containing only diagonals of 1 and -1 for the constrained model parameters (as in Equation 4.3). Each matrix row enforces a constraint between two model parameters,

$$\mathbf{R} = \begin{bmatrix} 1 & 0 & \dots & 0 & -1 & 0 & \dots & 0 & 0 & 0 \\ 0 & 1 & 0 & \dots & 0 & -1 & 0 & \dots & 0 & 0 \\ \vdots & & & & & \vdots & & & & \vdots \\ 0 & 0 & 0 & \dots & 0 & 1 & 0 & \dots & 0 & -1 \end{bmatrix}. \tag{4.3}$$

The objective function in Equation 4.1 is minimized also using *pyGIMLi* in a Gauss-Newton scheme (Günther et al., 2006). The model update is calculated by

$$\Delta\mathbf{m}^k = ([\Re[\mathbf{J}^\dagger\mathbf{C}_d\mathbf{J}] + \mathbf{R}\mathbf{C}_m)^{-1}(\Re[\mathbf{J}^T\mathbf{C}_d\delta\mathbf{d}^*] + \alpha\mathbf{R}\mathbf{C}_m\delta\mathbf{m}), \tag{4.4}$$

where $\mathbf{J} = \frac{\partial\mathscr{F}(\mathbf{m})}{\partial\mathbf{m}}$, the superscript † indicates the complex conjugate transpose and the superscript * indicates complex conjugation. It is clear if we compare equations 3.4 and 4.1 that the PWI method is equivalent to the LCI method in the case where no constraints are imposed by a roughening matrix **R**.

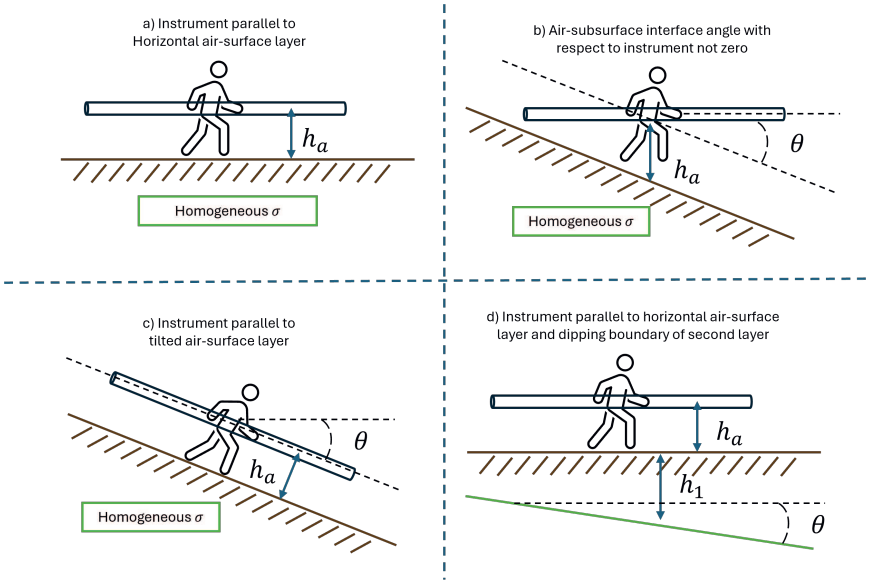


Figure 4.2: Illustration of four possible configurations of instrument geometry with respect to subsurface geometry. Case (a): Horizontally layered earth, instrument coils at the same height. Case (b): Air-subsurface interface with respect to the rigid-boom axis is not zero. Case (c): Dipping air-subsurface interface, instrument parallel. Case (d): Dipping second interface, rigid boom axis horizontal.

4.3. ERROR ANALYSIS ON MEASUREMENTS DUE TO 3D EFFECTS

In this section, we present several cases where the assumptions of the 1D forward model mentioned in Section 4.2 are violated: the subsurface is not horizontally layered, or the instrument is not positioned at the same height. These cases are shown in Figure 4.2.

CASE (A): HORIZONTAL EARTH MODEL

In this case the earth model is horizontally layered and the instrument lays parallel to the ground. The instrument coils are all at the same height.

CASE (B): AIR-SUBSURFACE INTERFACE WITH RESPECT TO THE INSTRUMENT IS NOT ZERO

This case (see Figure 4.2) illustrates when one of the two 1D forward function assumptions is violated. Either the instrument coils are at equal height and the air-subsurface interface is not horizontal. Or the air-subsurface interface is horizontal, but the instrument is at non-zero pitch angle. These cases are equivalent geometrically, representing an angle of the instrument with the air-subsurface interface. These measurements were modelled using *empymod* (from Werthmüller, 2017), modifying the coil heights and dip angles to retrieve the corresponding measurements. We show in Figure 4.3 the measurements corresponding to the instrument configuration at 8 m offset, for a wide range of homogeneous half-spaces with increasing degrees of angle between instrument and air-subsurface interface. In the figure it is clear that the measurements are distorted with

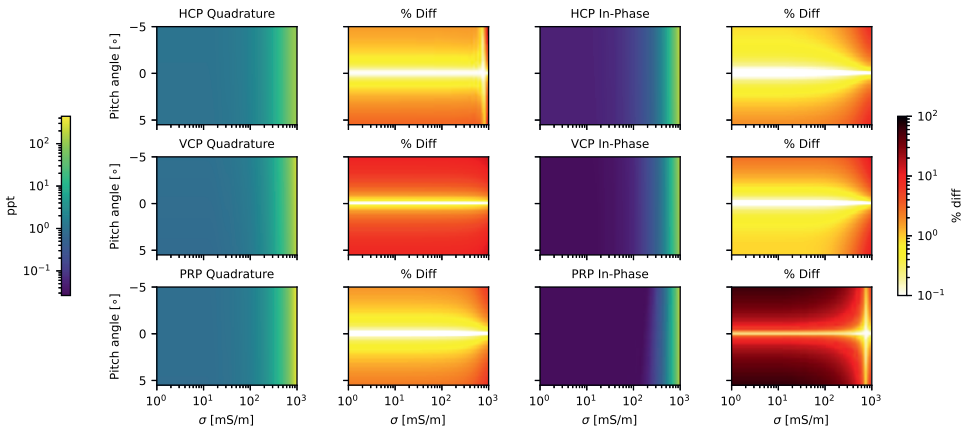


Figure 4.3: Case (b): Effect on the measurements due to pitch angle for offset 8 m. The first and third columns show the measurements and the second and fourth columns show the respective differences with a 0° pitch.

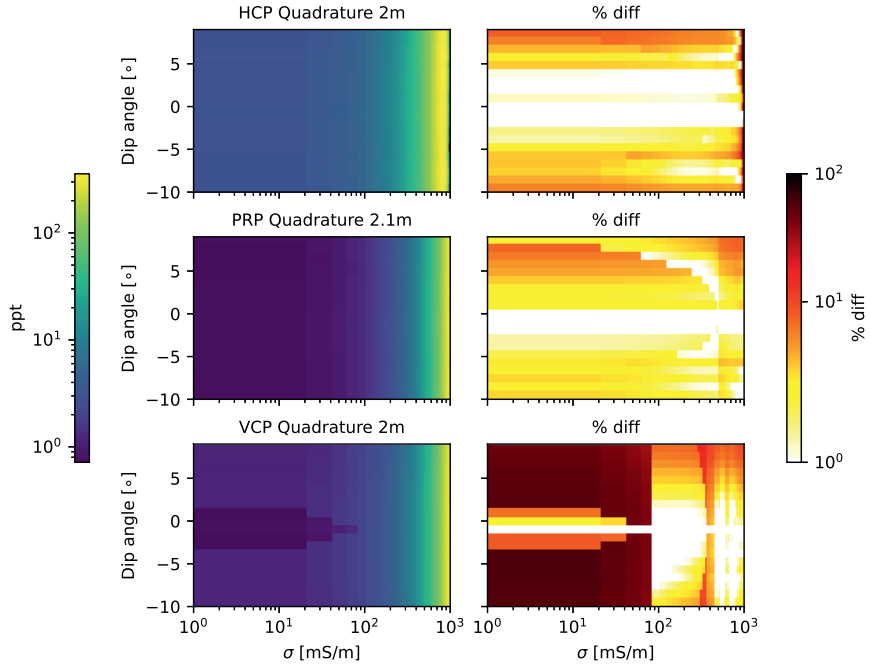
increasing pitch angle. The *quadrature* values of VCP and *in-phase* values of the PRP geometry are the most affected and differ largely with increasing pitch angle in all offsets and electrical conductivities of the halfspace. These results suggest that, if the rigid boom is positioned horizontally, the dip of the air-surface interface creates distortions of more than 5% in the measurements with only 2° dip. This effect worsens with increasing offset. It is possible that these measurement distortions will negatively impact the estimation of electrical conductivity models. The results for the remaining offsets are presented in the Supplementary Material (Carrizo Mascarell et al. (2025)).

CASE (C): DIPPING AIR-SUBSURFACE INTERFACE

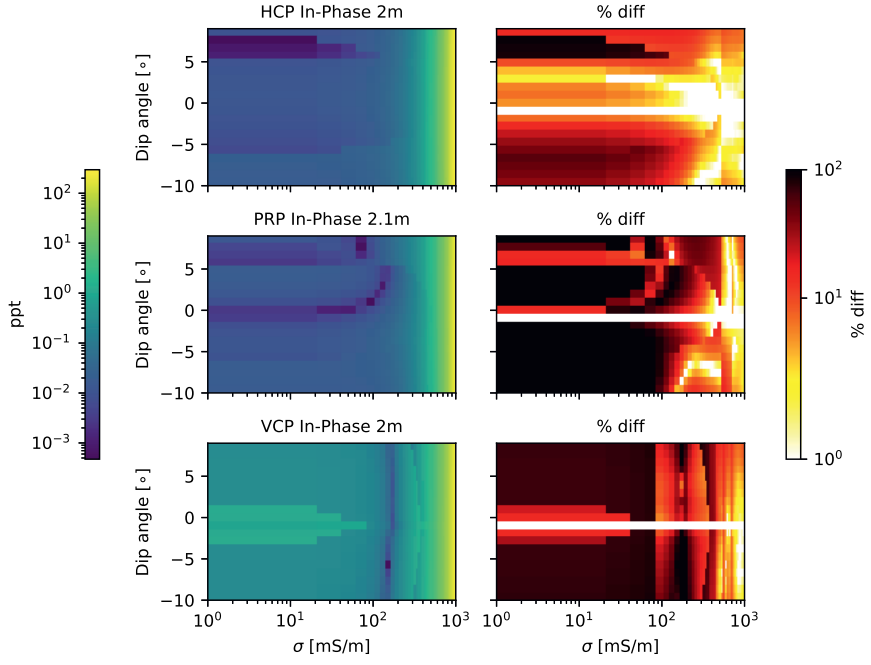
In case (c) we show the influence on the FDEM measurements of breakdown of both 1D forward function assumptions: the air-subsurface interface is not horizontal, and the instrument lies parallel to this interface, thus, the instrument coils are not at equal height. In Figure 4.4 the measurement deformations due to the violation of both assumptions are plotted for a range of different electrical conductivity halfspaces at 8 m offset. It is clear that for increasing dip angle the measurement is increasingly distorted. The VCP *quadrature* and the VCP anr PRP *in-phase* components show the largest deviations with only 2-3° of dip, in similar manner to case (b). The results for the remaining offsets are presented in the Supplementary Material (Carrizo Mascarell et al. (2025)).

CASE (D): DIP OF THE SECOND INTERFACE

In case (d) the subsurface geometry causes the breakdown of the first 1D assumption for a 2-layered model, since the interface between the first layer and the second layer is not horizontal. We show the results for eight 2-layered models presented in Table 4.1 with different electrical conductivity contrasts. The results of the upper conductive cases are presented in Figure 4.5 and the upper resistive cases are shown in Figure 4.6. Overall, for the upper conductive and upper resistive cases the measurement distortions are similar



(a) *Quadrature* values.



(b) *In-Phase* values.

Figure 4.4: Case (c): Effect of dipping topography for the coils at 8 m offset. The left column shows the measurements. The right columns presents the measurement difference percentage.

Table 4.1: Electrical conductivity (EC) distribution in 2-layered earth numerical cases

	Upper conductive layer		Upper resistive layer	
Model	Top EC [mS/m]	Bottom EC [mS/m]	Top EC [mS/m]	Bottom EC [mS/m]
1	200	20	20	200
2	400	20	20	400
3	800	20	20	800
4	1600	20	20	1600

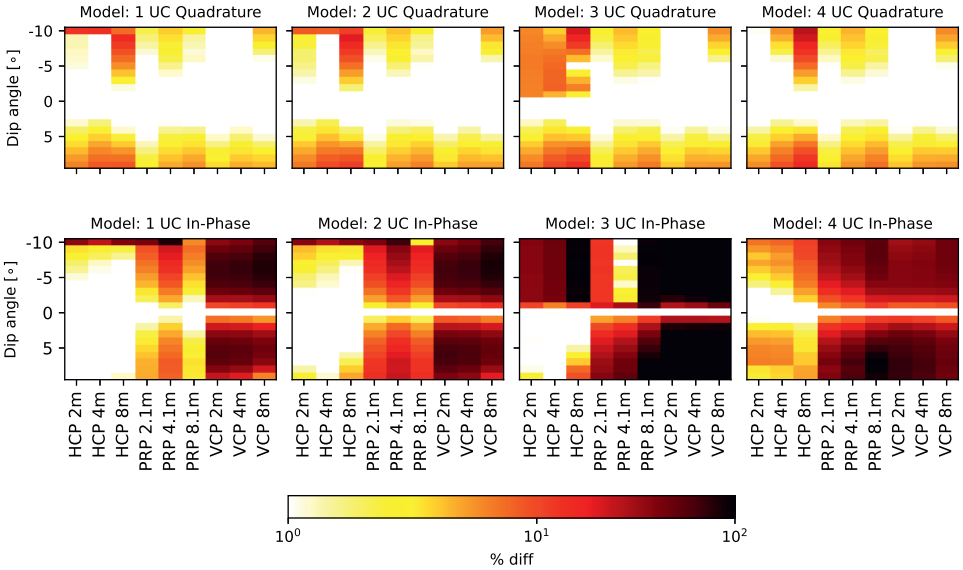


Figure 4.5: Case (d): Measurement distortion for a dipping second interface for upper conductive 2-layered models. Top row: *Quadrature* measurements. Bottom row: *In-Phase* measurements.

for different electrical conductivity contrasts. For all the upper conductive cases, the VCP *in-phase* measurements are the most affected. However, for the upper resistive cases, the PRP *in-phase* measurements are highly distorted (more than 20 % of difference) with only 2-3° of dip in the second interface.

4.4. ROBUSTNESS OF THE INVERSION METHODS

In the previous section, we showed how the FDEM measurements are quite rapidly distorted with the breakdown of the 1D forward function assumptions in the presence of variations of not-horizontally layered geometry (even with only 2-3° of difference), or due to the instrument pitch. In this section, we will test how these distortions affect the PWI and LCI results, in noise-free conditions. We present examples for two-layered earth models, for a horizontally layered earth and this instrument configuration, with all coils at the same height. It is important to mention that using a 2-layered model parameterization substantially constrains the solution space, and thus it limits the capability of the inversion method to explain the data.

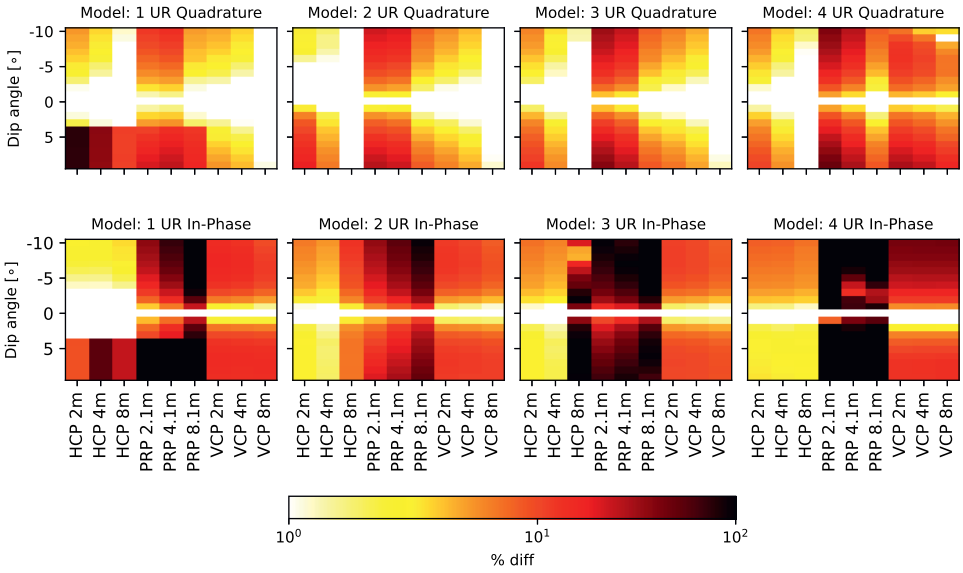


Figure 4.6: Case (d): Measurement distortion for a dipping second interface for upper resistive 2-layered models. Top row: *Quadrature* measurements. Bottom row: *In-Phase* measurements.

First, we apply the method for numerical 2.5D models (3D models where the third dimension projects the 2D model) and 3D models. Then, we apply the methods in a field case. Example 0 is a base case where the measurements are calculated using 1D forward modelling. In the following numerical examples, the measurements were simulated using 3D forward modelling. Examples 1 to 3 are 2.5D models (where the third dimension is a projection of a 2D cross-section). Examples 4 and 5 are 3D models, with variations in the electrical conductivity distributions in 3 dimensions.

EXAMPLE 0. 1D FORWARD MODELLED MEASUREMENTS

In this case, we show the results of the PWI and LCI methods for Model 4 in Table 4.1 for the upper conductive contrast. This case is shown as a base result to demonstrate the capabilities of the inversion methods when the measurements 1D assumptions are not broken. The estimation results are presented in Figure 4.7. The data fit is presented in Figure 4.8. It is clear that the fit of the models is very accurate. The measurements are reproduced with less than 1% difference.

EXAMPLE 1. FIXED DIP OF THE SECOND INTERFACE

We applied both inversion methods to 2-layered models with different electrical conductivity contrasts presented in Table 4.1 and increasing dip. The inversion results for two cases are presented in Figures 4.9 and 4.11 (the results for all examples in Table 4.1 are provided in the Supplementary Material (Carrizo Mascarell et al. (2025))). The poor estimation of the lower layer, in the upper conductive cases, can be explained by the low sensitivity of the measurement to the resistive part of the subsurface. However, we also

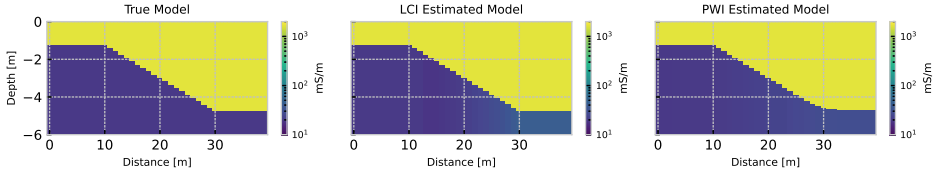


Figure 4.7: Results of inversion methods for Model 4 using 1D forward modelled measurements.

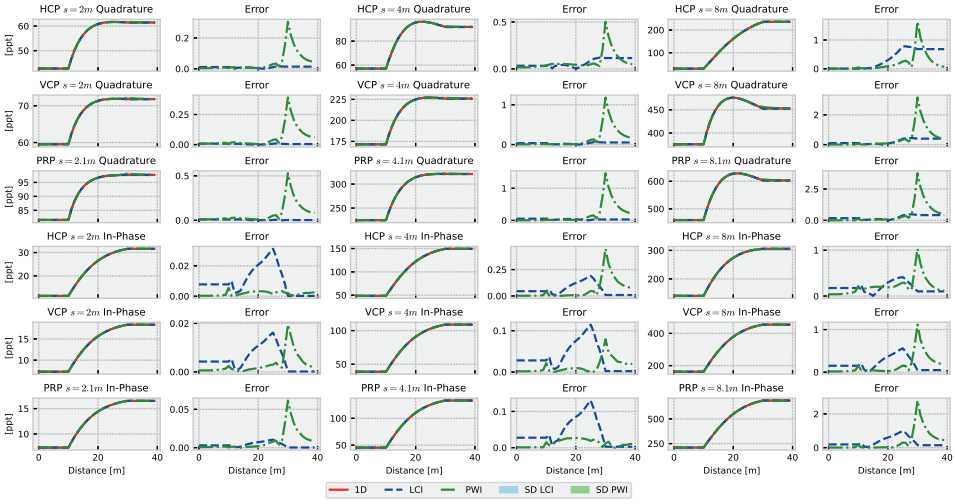


Figure 4.8: Measurements corresponding to the results of Figure 4.7.

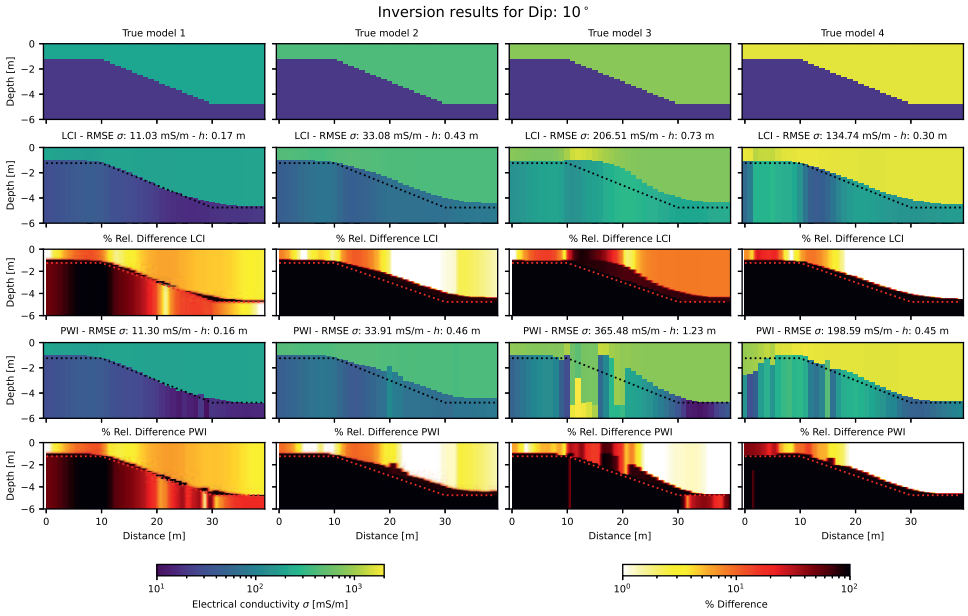


Figure 4.9: Inversion results of 2-layered earth models with an upper conductive layer and a slope of 10° between positions 10 to 30. Upper row: True models. Second row: LCI estimated models. Fourth row: PWI estimated models. The third and fifth show the error percentage of the inversion results. In each model estimation, the RMSE of the model parameters is shown.

see erratic estimations from PWI for Models 3 and 4 for a 10° dip. In Figure 4.10, we can see that the response of the PWI estimation does not differ more than 20 % difference with respect to the true measurements. However, we observe a much larger difference (larger than 100 % in some positions) between the true measurements, simulated in 3D, with respect to their respective 1D forward modelled measurements, especially for the 8 m offset. With the PWI, the measurement distortions in this case negatively affect the possibilities of obtaining accurate estimations.

On the other hand, the results provided by both the PWI and LCI methods are similar in the upper resistive cases. In Figure 4.12 the data fit for the upper resistive Model 4 for a 10° dip. In this case, we also observe that the 3D forward-modeled and 1D forward-modeled measurements differ significantly. This affects equally the LCI and PWI results, although not as strongly as in the upper conductive example.

A summary of the measurement errors for Model 1 in the upper resistive case is presented in Figure 4.13. The figure shows that for increasing dip values, for every coil configuration, the 1D forward modelled measurements increase their mean error, as well as the standard deviation. This is also true for the responses calculated for the LCI and PWI estimates. In Figure 4.14 we show the same analysis for Model 4, which has an increasing contrast between upper and lower layer conductivities. The mean error values are larger for these cases, since the conductivity also affects the estimations. Overall, for all cases the behaviour is similar, having increasing mean error values in the measurements with

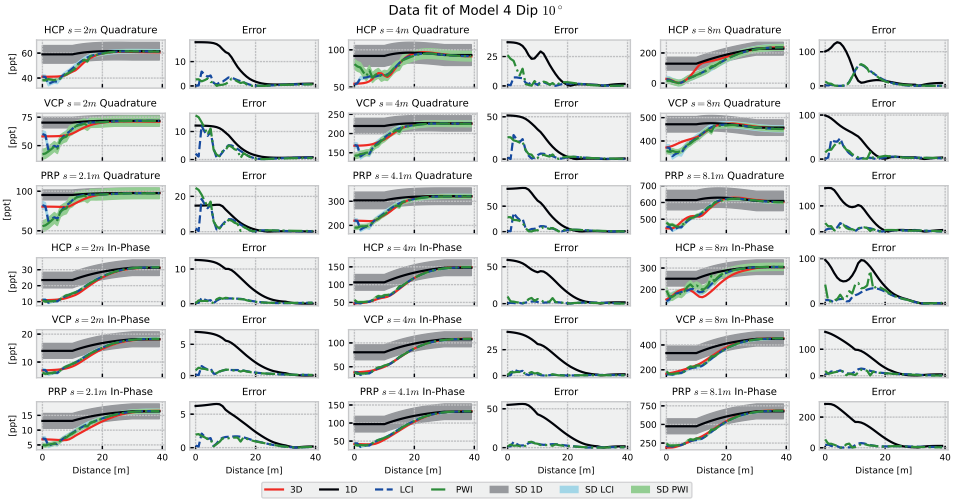


Figure 4.10: Data fit results corresponding to Model 4 in Figure 4.9. The first, third and fifth column show the data values. The second, fourth and sixth column show the error percentage. The black line represents the measurements of the true model using the 1D forward function. The red line corresponds to the 3D forward function. The blue and green lines correspond to the 1D forward function response of the LCI and PWI estimated models, respectively.

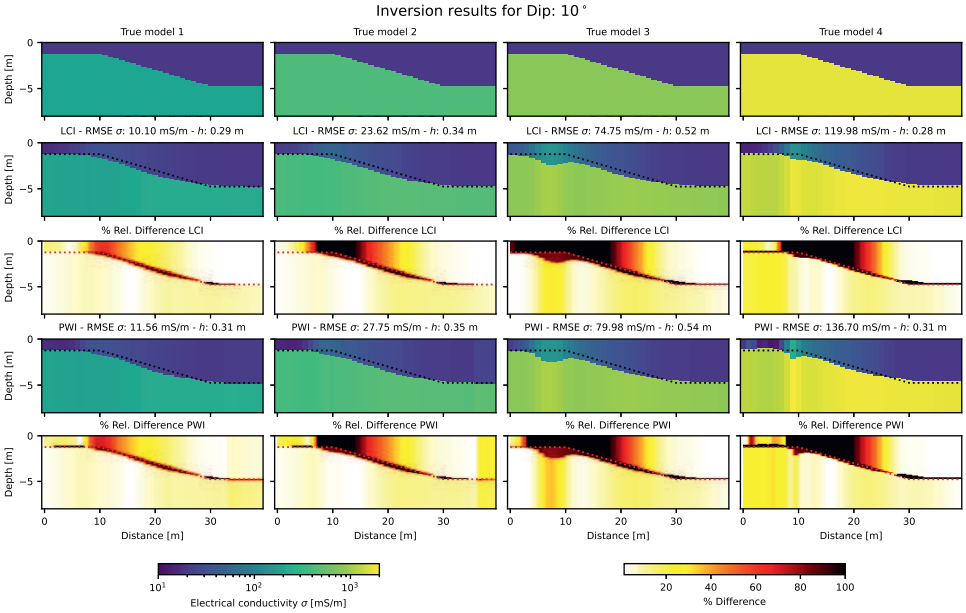


Figure 4.11: Inversion results of 2-layered earth models with an upper resistive layer and a slope of 10° between positions 10 to 30.

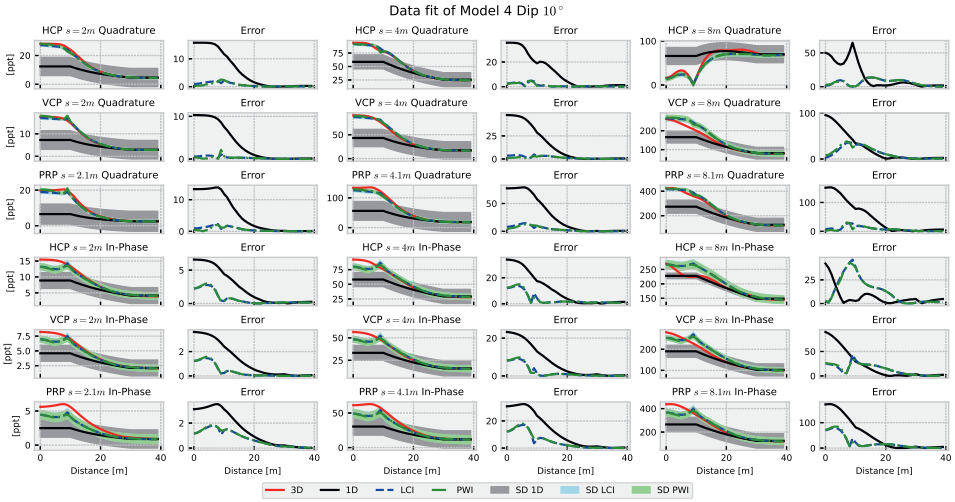


Figure 4.12: Data fit results corresponding to Model 4 in Figure 4.11.

increasing dip angle for the interface between first and second layer.

With the intention of demonstrating the impact of noise in the result of the inversion methodologies, we estimate an example for Model 2 in the upper conductive case. In Figures 4.15 and 4.16 the resulting models for increasing Gaussian random noise percentages in the measurements are shown. As expected, the estimates RMSE values increase with increasing noise in the measurements. It is clear that the LCI estimates show less spurious results, and the interface between first and second layer is better predicted.

In order to show the the performance of the inversion methodologies in a complex 2-layered geological setting, where the subsurface is not nearly layered, we present an example in Figure 4.17. Predictably, both inversion methodologies have inaccurate estimations. This is due to the fact that the measurements in these complex environments are not properly reproduced by the internal 1D forward modeller in the inversion schemes. Moreover, the LCI method holds constraints that assume a nearly layered geology, which is clearly not correct.

EXAMPLE 2. INCREASING DIP OF THE SECOND INTERFACE

In order to evaluate the effects of lateral variations in the LCI and PWI inversion methodologies, we introduced a numerical case where the boundary between two electrical conductivity layers increasingly changes with distance, based on a similar analysis by Klose et al. (2022). The estimation results are shown in Figure 4.18. We observe that the PWI estimated model shows a worsening of the estimation with increasing lateral variation of the boundary, especially in the peaks. However, it reproduces, on average, the position of the boundary. On the other hand, the LCI shows a smoothed result that does not reproduce the boundary position of the peaks. These results indicate that lateral variations will affect the PWI and LCI estimations when assuming a 1D horizontally layered earth

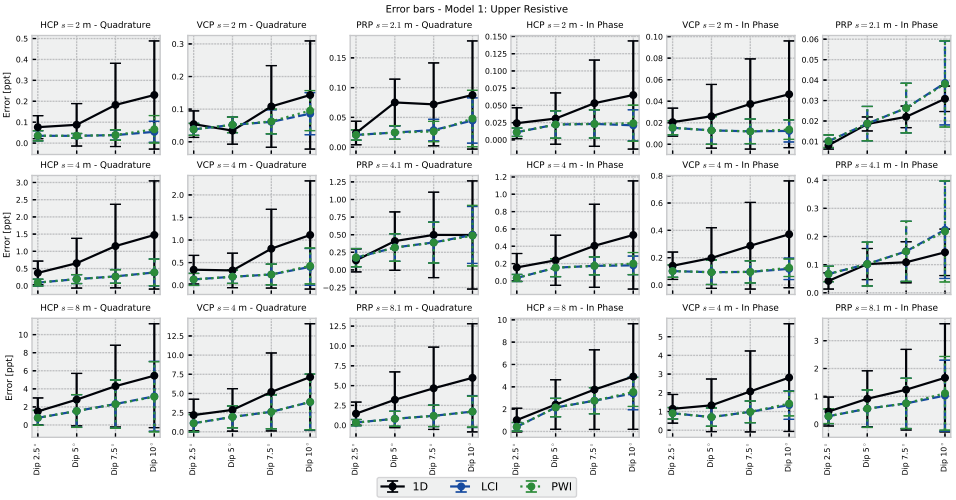


Figure 4.13: Mean error values of the measurements for Model 1: Upper Resistive case.

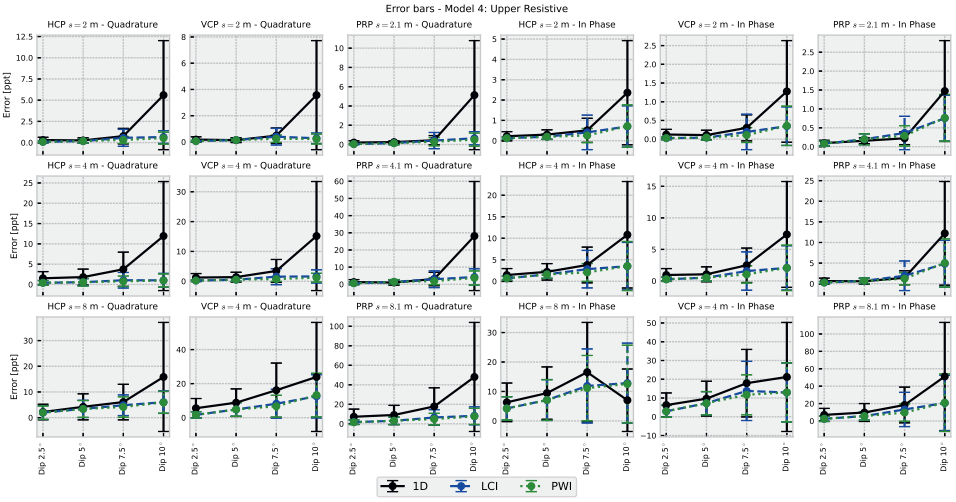


Figure 4.14: Mean error values of the measurements for Model 1: Upper Resistive case.

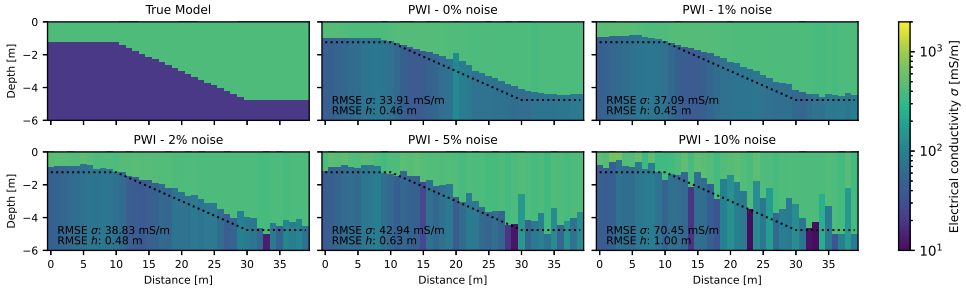


Figure 4.15: Effects of noise in the measurements in the PWI inversion.

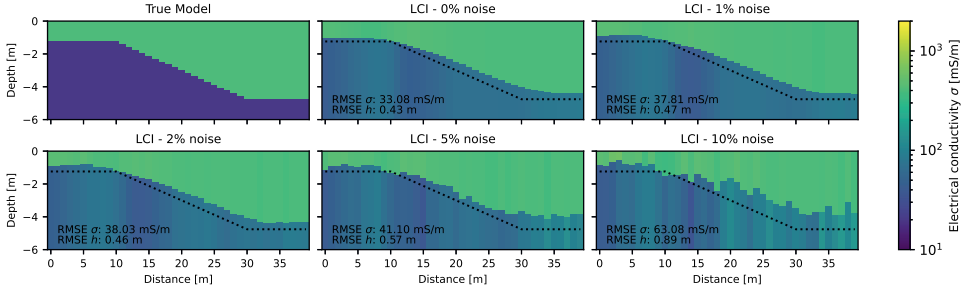


Figure 4.16: Effects of noise in the measurements in the LCI inversion.

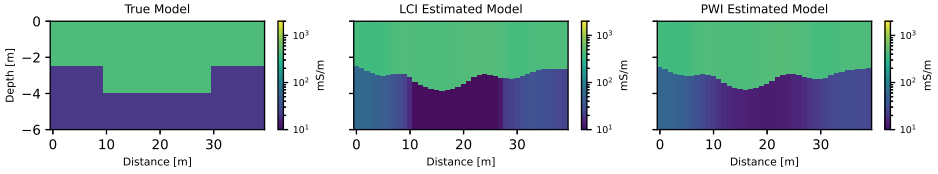


Figure 4.17: Estimation results of the inversion methods for a complex geological distribution.

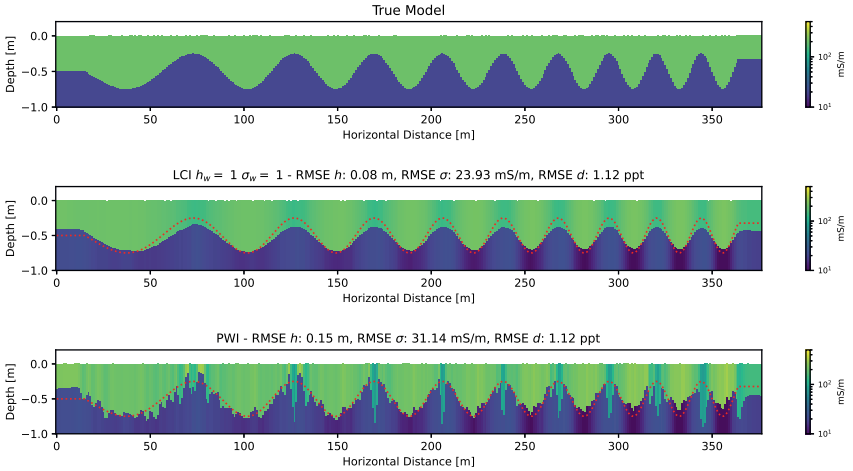


Figure 4.18: Results of inversion methods for an increasing dip of the second interface. Top: True model. Middle: LCI estimated model. Bottom: PWI estimated model. The dotted red line indicates the true position of the interface. RMSE values of the estimated model parameters is presented.

in the inversion forward function, as in this case. The data fit between the true measurements and the estimation responses are presented in the Supplementary Material (see Carrizo Mascarell et al., 2025). We can see how the measurements are increasingly different to the true 3D measurements. However, the difference between the 1D forward response of the model and the 3D measurements is even larger. Meaning the inversion methods try to fit the 3D data, jeopardizing the accuracy of the estimations. These numerical examples assumed an earth model without topography, with an air-surface interface at $z = 0$, and the instrument lying parallel above the air-surface interface at a height $h_a = 0.3$ m.

EXAMPLE 3. INCREASING DIP OF THE AIR-SUBSURFACE INTERFACE

To understand the effects of the dipping air-surface interface, we pose an instrument positioning case (Case (c) in Figure 4.2) where we assume that the instrument is always parallel to the surface, with a height $h_a = 0.3$ m from the interface. The geometry of the instrument changes as we follow the topography while measuring, as in Figure 4.19. We designed a numerical example shown in Figure 4.21, in which the topography variations increase laterally. It is important to stress that the topography's maximum height is quite small (50 cm) and the figure aspect is exaggerated (~ 300:2), the maximum dips are 4°. The measurements are simulated using 3D forward modelling. In Figure 4.20, we illustrate the positioning of the rigid boom in the simulated model.

The results from PWI and LCI methods shown in Figure 4.21 present increasingly worse estimations with increasing topography dip. We infer that this is due to the increasing pitch angle in the instrument geometry, and that the air-surface interface is not parallel to the rigid boom, violating the assumptions of the 1D forward model. Therefore, the 1D forward function used in the inversion methods is not able to accurately represent

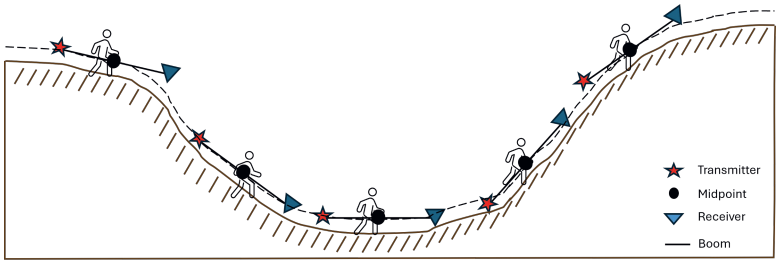


Figure 4.19: Scheme of data acquisition with topography. The midpoint is positioned 0.3 m above the air-subsurface interface. The instrument pitch follows the dip of the slope.

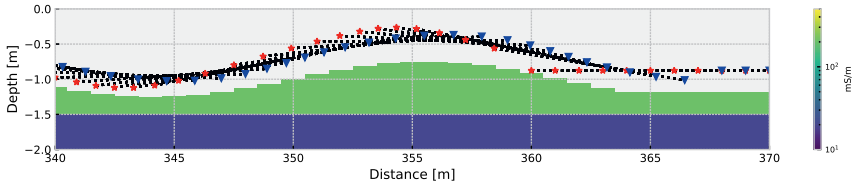


Figure 4.20: Rigid boom position for positions at distance X: 340-370 m. Red star: transmitter position. Blue triangle: receiver position at 8 m offset. Dotted line: rigid boom. The midpoint of the boom is located 0.3 m above the air-surface interface. The instrument pitch angle is tangent to the slope. Due to the increasingly undulating topography and rigidity of the boom, there will be a larger vertical air-surface interface distance from the transmitter or receiver coil in some positions.

the true model measurements. This is also shown by the inversion responses compared to the true measurements in the Supplementary Material (see Carrizo Mascarell et al., 2025). These results suggest that these gentle topography variations negatively impact the estimations when assuming an instrument parallel to the air-surface interface and a horizontally layered earth in the inversion methods.

EXAMPLE 4. CHANNEL FEATURE

In this numerical example, we present a 3D model of a 2-layered earth with a channel feature. The measurements were simulated using the 3D forward modeler previously mentioned. The model contains the channel feature in the upper layer along with channel bars at each side and river plains, with an electrical conductivity of 50 mS/m, 30 mS/m and 10 mS/m, respectively. The bottom layer electrical conductivity is 100 mS/m. In Figure 4.22, a map representation of the model parameters (σ_1, σ_2, h_1) of the channel is presented, as well as the results of the LCI and PWI estimations. The maps show that PWI and LCI estimations are very similar in all parameters. The results of the estimations in cross-section Y = 10 m is presented in Figure 4.23. The resulting estimations show alike results for LCI and PWI inversion methodologies for the different cross-sections, presented in the Supplementary Material (Carrizo Mascarell et al. (2025)). The higher inaccuracies are located in the transitions from channel bars to river plains, due to the effect in the measurements to lateral changes in the model parameters, which are also clear in the misfit between the 1D and 3D responses in these positions (see Supplemen-

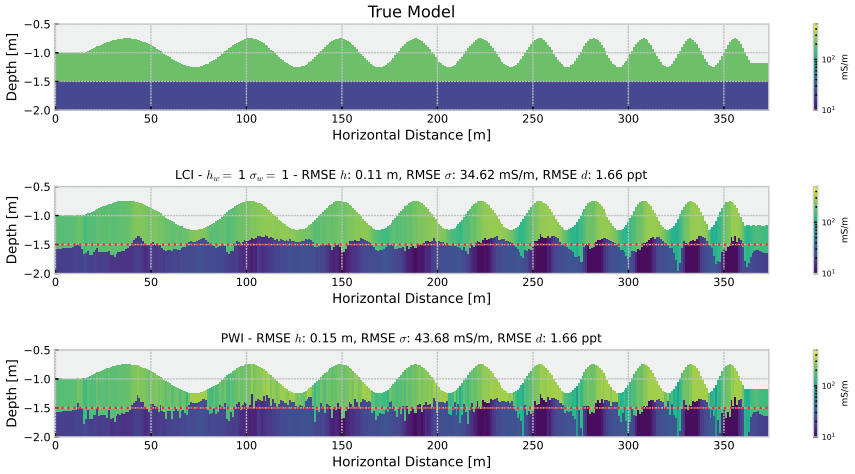


Figure 4.21: Results of inversion methods for an increasing dip of the air-subsurface interface. Top: True model. Middle: LCI estimated model. Bottom: PWI estimated model. RMSE values of the estimated model parameters σ and h, and the response d are presented.

tary Material (Carrizo Mascarell et al., 2025)). The fit between the LCI and PWI estimated and true response is below 10% error.

EXAMPLE 5. CHANNEL FEATURE WITH TOPOGRAPHY

This example presents the previous 3D channel feature in a soft valley topography, which is presented in Figure 4.24. The computed measurements were obtained using 3D forward modelling assuming the instrument positioning parallel to the air-subsurface interface (as in Case (c)). The results of the PWI and LCI estimated models are presented in Figures 4.25 and 4.26. In the maps and cross-section of the estimated models, it is clear that both PWI and LCI methods provide similar results for the model parameters. Both inversion methodologies are significantly affected by the topography effects in the measurements. The breakdown of the estimations with increasing topography is observed in the worsening of the estimated models from crossline Y = 10 m to crossline Y = 30 m, due to the topography valley becoming narrower in that direction, and thus, larger dips. Moreover, comparing the responses misfits, it is clear that in the Y=30 m crossline, the difference between 1D forward-modeled and 3D forward-modeled responses increases largely (see Supplementary Material (Carrizo Mascarell et al., 2025)). Neither the PWI or the LCI methods correspond accurately to the true responses.

CASE STUDY: ACKERDIJKSE PLASSEN

We applied both inversion methods for FDEM data acquired in the natural monument Ackerdijkse Plassen, The Netherlands (see Figure 2.10). This area shows a sandy channel deposit feature embedded in peat-silt plains in satellite images and nearby borehole data. In this case, we used only the HCP and VCP coil geometries in the methodology. For offsets up to 4 m, the *in-phase* values are considered less accurate according to the

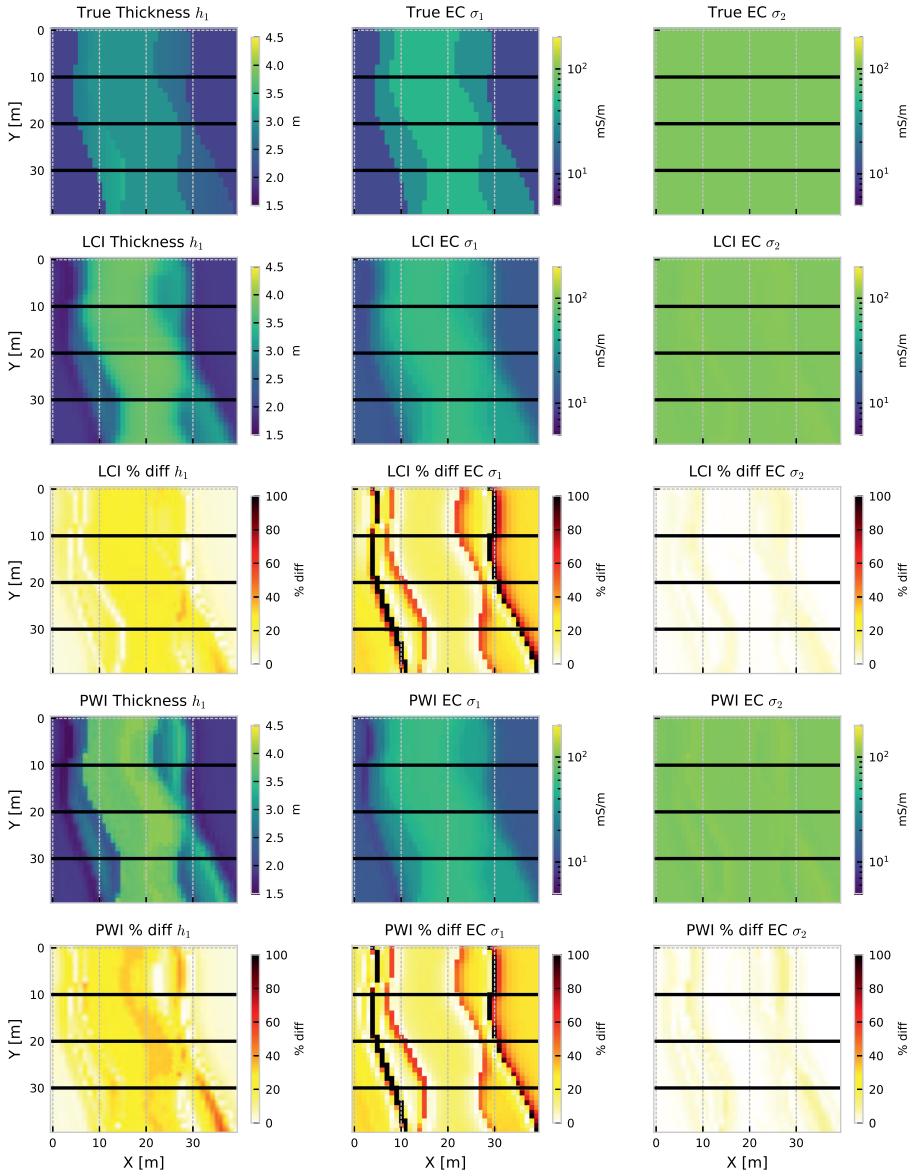


Figure 4.22: Maps of model parameters in Channel example. Top row: True model parameters. Second and fourth row: Maps of the LCI and PW estimated model parameters. Third and fifth row: Maps of the difference percentage between true and estimated models. The position of cross sections is indicated with black lines.

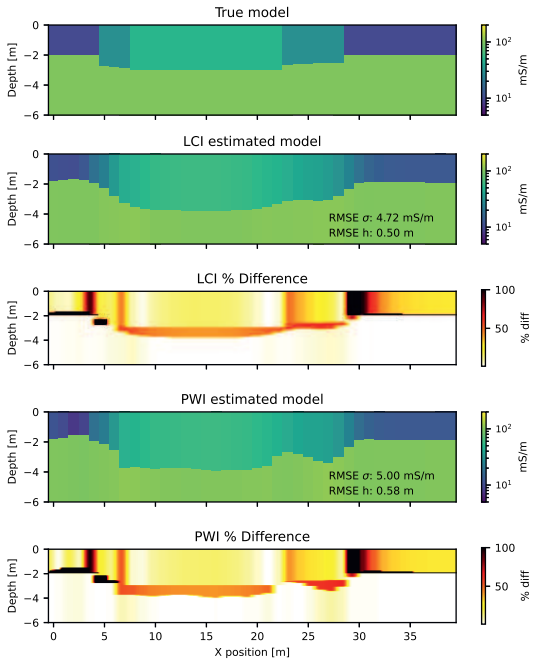


Figure 4.23: Inversion results at crossline Y = 10 m from channel feature example. Top row: True model. Second and fourth row: LCI and PWI estimated models. Third and fifth row: difference percentage between true and estimated model.

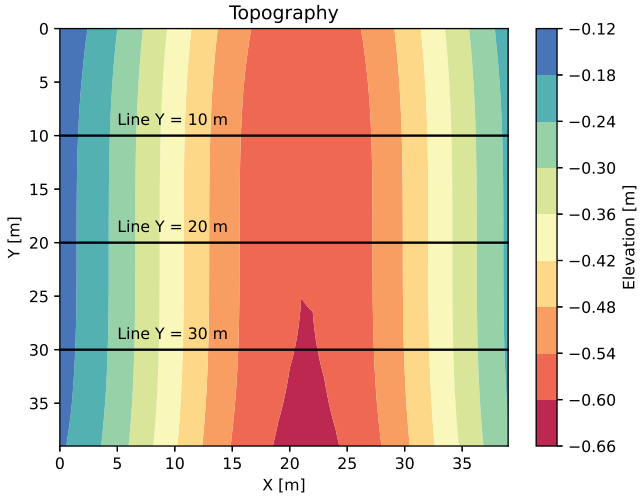


Figure 4.24: Topography map of a valley for the numerical example of a 3D Channel.

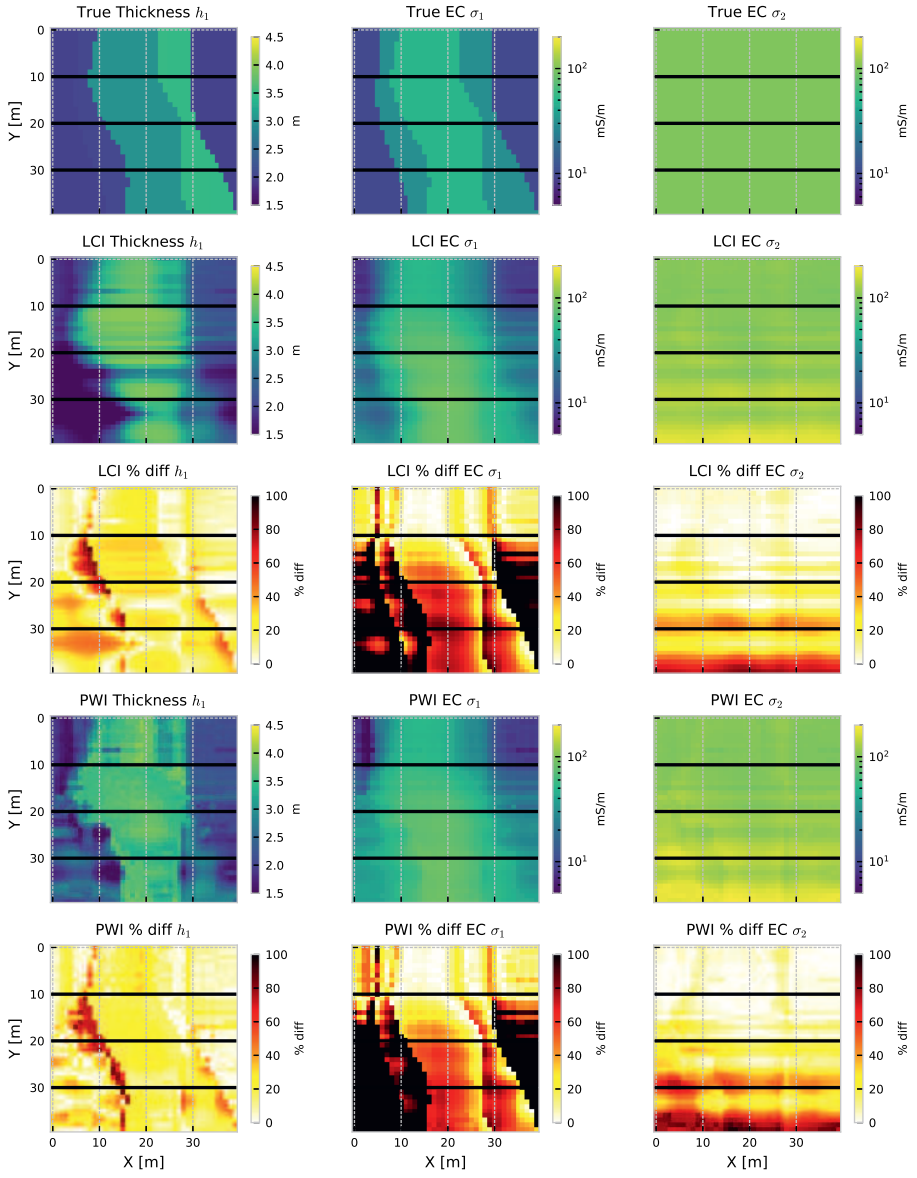
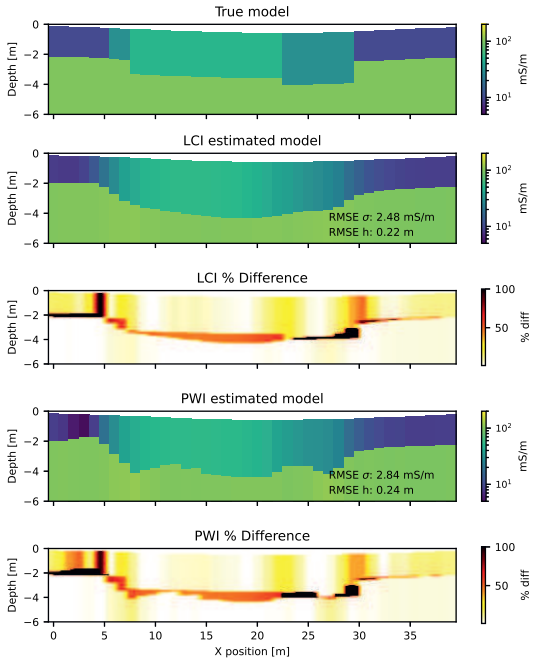
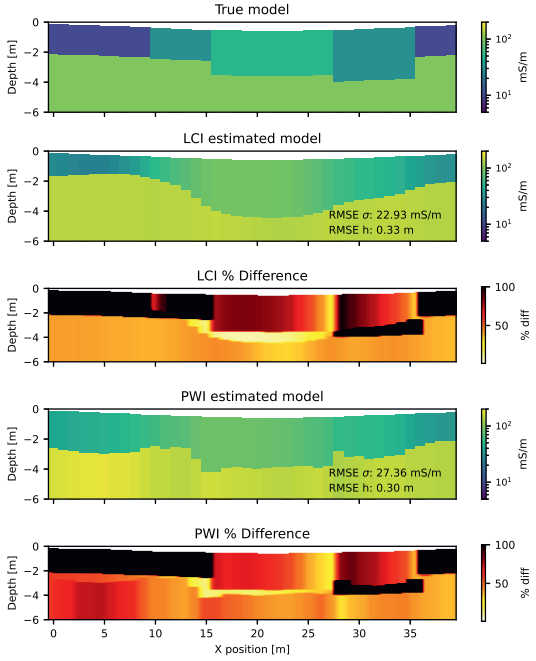


Figure 4.25: Maps of model parameters for the 3D channel example with topography. The position of the cross-sections is indicated with a black line.



(a) Cross-section at Y=10 m.



(b) Cross-section at Y=30 m.

Figure 4.26: Inversion results at two cross-sections for a 3D channel feature in a valley topography. The cross-section at Y=10 m presents better results than the cross-section at Y=30 m, where the valley is narrower and the dips are larger.

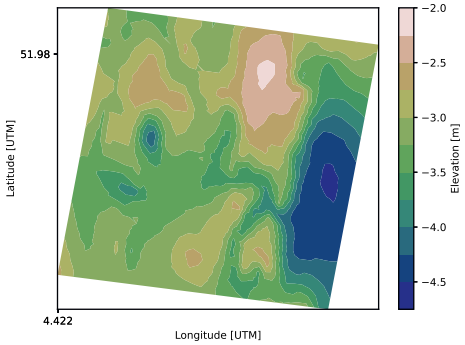


Figure 4.27: Topography map of the field study area in Ackerdijkse Plassen natural monument (see Figure 2.10.

FDEM instrument manufacturer so these were not included in the estimations (Taylor, 2023). The data was acquired holding the rigid-boom parallel to the topography dip, with the midpoint at a fixed height from the air-subsurface. The topography of the area is shown in Figure 4.27.

The acquired data was inverted using the PWI and LCI methodologies. Cross-sections and maps of the estimated models are shown in Figures 4.28 and 4.29. From the cross-section results, we deduce that both inversion methods obtain similar electrical conductivity values of the layers and thickening of a channel feature in the center area of the cross-sections. However, the LCI method presents a smoother estimated model, with transitional changes with respect to the thicknesses and electrical conductivities. We consider that this is an advantage of the LCI method since it provides more stable solutions with respect to the noise present in the data, which creates a laterally inconsistent estimated model in PWI results. In Figures 4.30 and 4.31, the field measurements and the estimated responses are compared. As expected, the 1D forward-modeled responses differ from the true measurements, which were acquired by infringing the assumptions.

The resulting responses reproduce the HCP and VCP, both 2m and 4m coil separation *quadrature* measurements. However they do not reproduce the field measurements in the HCP *quadrature* at 8 m offset coil geometry. It is difficult to determine the reason, which could be due to 3D variations of the electrical conductivity or additional layers not considered in the parameterization of the inverse problem. The *in-phase* responses are reproduced with errors from 10-20%. We know that some distortions caused by the dipping topography and the instrument pitch are being propagated into the estimation of the model. However, since the distribution of electrical conductivity in the area is not known with certainty it is difficult to quantify the exact influence of breaking the 1D forward modelling asummptions in this case.

4.5. DISCUSSION OF RESULTS

In section 4.3, we presented several examples where the assumptions of the 1D forward function are violated. Cases (b) and (c) show that the pitch angle of the instrument and topographical variations can notably affect the measurements in both *quadrature* and

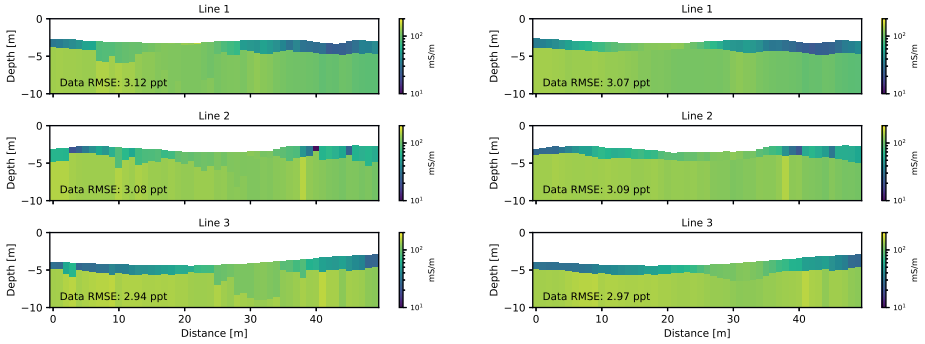


Figure 4.28: Left: Cross-sections of the models estimated with PWI. Right: Cross-sections of the models estimated with LCI. RMSE values of the estimated responses are presented. The positions of these cross-sections are shown in Figure 2.10.

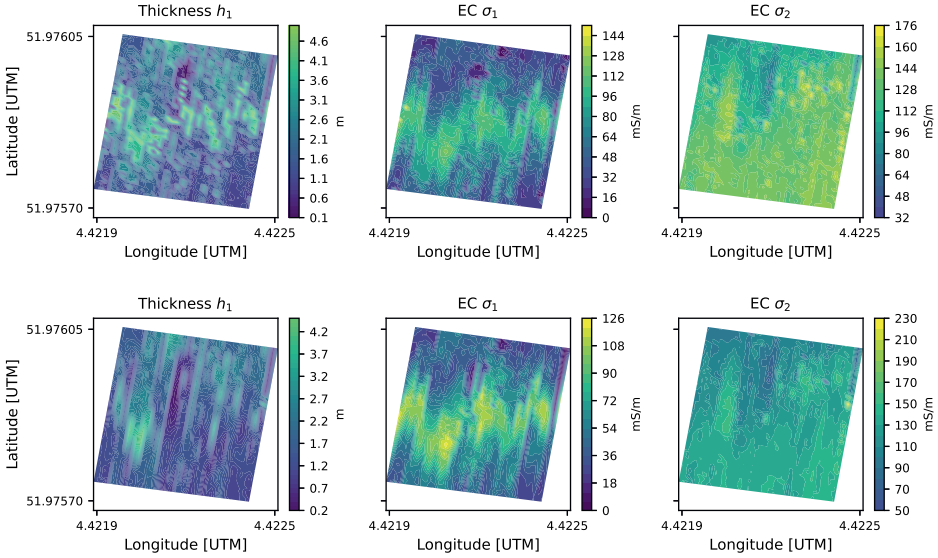


Figure 4.29: Top: Maps of model parameters estimated with PWI. Bottom: Maps of model parameters estimated with LCI. The results show similar estimations overall with both inversion methods.

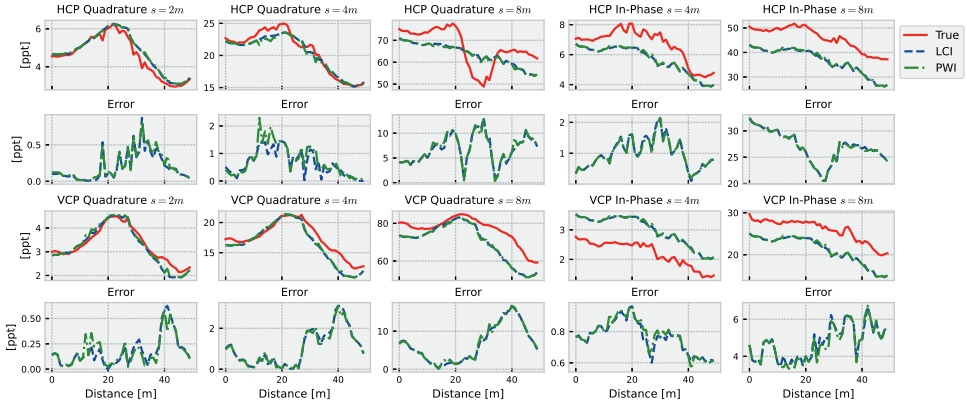


Figure 4.30: Data fit of the inversion results of Line 1 in Figure 4.28. Red line: Field measurements. Blue dashed line: LCI response. Green dashed line: PWI response.

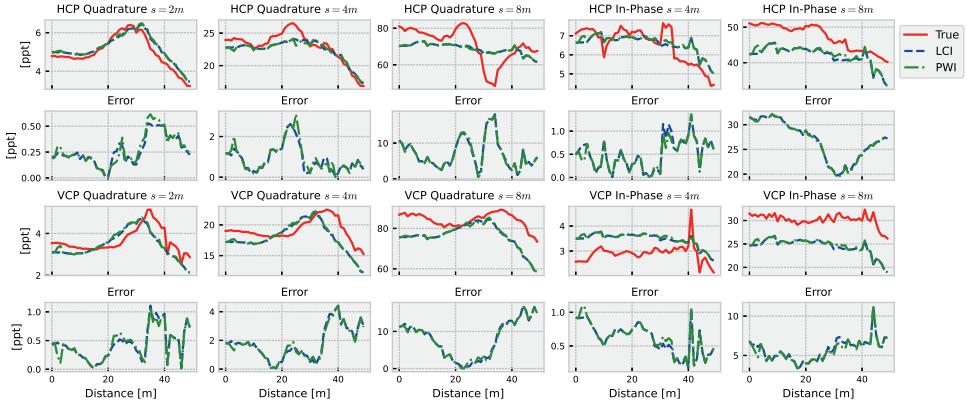


Figure 4.31: Data fit of the inversion results of Line 3 in Figure 4.28. Red line: Field measurements. Blue dashed line: LCI response. Green dashed line: PWI response.

in-phase components, particularly in the VCP *quadrature* and PRP *in-phase* parts. Furthermore, case (d) showed that the dip of the second interface also impacts the measurements, especially the VCP and PRP *in-phase* parts. In cases (c) and (d), it is clear from Figures 4.4, 4.5 and 4.6, that the *in-phase* component is the most affected by the breakdown of the 1D forward function.

To determine how far these measurement distortions affect the model estimations, we applied the PWI and LCI methods to several numerical examples shown in section 4.4. Although the results of case (d) show large distortions in the *in-phase* measurements for all the model contrasts, the estimation results of both PWI and LCI methods in example 1 are sufficient to solve 2-layered earth models accurately. This is true when measurements are acquired without topography, the assumption of instrument positioning parallel to the air-surface interface holds, and the second interface dip is not greater than 7.5°. This is also clear in example 2, where with increasing dip of the second interface, the inversion results worsen. The LCI methodology presents little to no advantage with respect to estimation accuracy. In Figure 4.18, the results show that both PWI and LCI are affected by the effects of 2D lateral variability. While the PWI can overall estimate the position of the first layer thickness, the results also present spurious estimations. On the other hand, while LCI does not resolve properly the first layer thickness, it provides smooth and more stable electrical conductivity estimations.

From the results in Figure 4.3, we observe that in a data acquisition scheme where the instrument is held horizontally, a dipping air-subsurface interface at an angle greater than 2° can distort the measurements in all coil configurations and components. This is also demonstrated by both the results of PWI and LCI in example 3 (Figure 4.21), where the inversion results worsen with increasing undulation of the air-subsurface interface. The PWI results show poor first-layer thickness estimations, even with slight topography variations, and worsening in the electrical conductivities as the dip increases. Moreover, LCI provides a better first-layer thickness estimation but, like PWI, exhibits declining accuracy in electrical conductivity values with increasing dip.

Examples 4 and 5, which include a 3D channel feature, also illustrate very clearly the effect of a dip in the topography. In example 4, where there is no topography influence, the PWI and LCI estimations and responses did not diverge significantly from the true values. The largest errors were only present where there were lateral conductivity variations. However, in example 5, imposing on the model a very soft topography made the measurements diverge significantly, causing poor results of the model estimations. Comparing all the geometry cases and their error propagation in the numerical examples, we consider that case (c) shows the largest impact. The breakdown of both assumptions creates distortions larger than 10% with only 2° dip in all the coil configuration *in-phase* measurements and in the VCP *quadrature* measurement, which increased with the resistivity of the halfspace.

The resulting estimations of the case study are quite similar for both PWI and LCI methods in terms of electrical conductivity values. In both, the channel feature can be observed in the first layer. The thickness of the first layer varies smoothly in the LCI results. We presume that the spiky nature of the thickness of the first layer for the PWI estimated model can result from noise in the data. We consider that LCI can be used to obtain smoother estimations of the model parameters when noise is present in the data,

which is very common in field cases. Nonetheless, we must be careful with the geological setting where this algorithm is applied since LCI assumes that lateral variations of the parameters are smooth.

In this field case study, it is not possible to determine whether the discrepancies between the PWI and LCI responses and the true measurements arise from topographic variations or from other factors, such as noise. It is also likely that the imposed 2-layer model parameterization does not accurately represent the complexity of a three-dimensional Earth. Consequently, we cannot quantify the influence of topography and pitch angle on the measurements, nor assess the extent to which these factors affected the model estimations. Even so, the numerical examples showed that there must be errors in the estimations due to the presence of topography and holding the instrument parallel to the dipping ground surface. Both PWI and LCI estimations are likely not reproducing the true distribution, partly due to the measurement distortions.

This analysis demonstrates that while both PWI and LCI can provide reasonable estimations, under ideal acquisition conditions, their accuracy decreases significantly when measurements are affected by topography, pitch angle, or subsurface complexity. Relying on 1D forward functions in the presence of 3D effects not only amplifies errors in the estimations but also increases the potential non-uniqueness of the inversion problem. These observations highlight the importance of accounting for acquisition geometry and geological complexity when interpreting inversion results. Future work should focus on integrating topographic and orientation corrections directly into the inversion process or developing approaches that introduce the acquisition and geological geometry.

4.6. CONCLUSIONS

The analysis demonstrates that deviations from the 1D forward modelling assumptions, particularly instrument tilt, topographic undulations, and layer dips, can significantly distort frequency domain electromagnetic induction measurements, with the severity increasing as these factors become more pronounced. These deviations are propagated into the inversion results. Both piecewise and laterally constrained inversion methods can produce accurate results for flat topography, gentle slope 2-layered earth models, but their performance deteriorates in the presence of topography (larger than 2°) or drastic lateral conductivity variations. Piecewise inversion tends to estimate first-layer thickness more precisely but suffers from spurious or spiky outputs in the presence of measurement distortions or noise. On the other hand, laterally constrained inversion produces smoother and more stable conductivity estimates, especially in noisy data, although with reduced thickness accuracy. Neither method fully compensates for strong 2D/3D effects, and the reliability of both depends heavily on the geological setting and acquisition conditions. Therefore, care must be taken to assess the assumptions considered before applying these inversion approaches to real-world surveys. It is possible that for strongly 3D varying geological settings, topography/pitch-angle corrections or a 2D/3D inversion methodology should be used. The findings show the importance of developing realistic yet computationally efficient forward modelling and inversion methods that can account for complex acquisition conditions in frequency-domain electromagnetic induction surveys.

DATA AVAILABILITY

The codes and data used in this chapter is available via Zenodo (Link).

BIBLIOGRAPHY

Alumbaugh, D. L., & Newman, G. A. (2000). Image appraisal for 2-D and 3-D electromagnetic inversion. *Geophysics*, *65*(5), 1455–1467. https://doi.org/10.1190/1.1444834

Auken, E., Christiansen, A. V., Jacobsen, B. H., Foged, N., & Sorensen, K. I. (2005). Piecewise 1D laterally constrained inversion of resistivity data. *Geophysical Prospecting*, *53*(4), 497–506. https://doi.org/10.1111/j.1365-2478.2005.00486.x

Auken, E., & Christiansen, A. V. (2004). Layered and laterally constrained 2D inversion of resistivity data. *Geophysics*, *69*(3), 752–761. https://doi.org/10.1190/1.1759461

Bai, P., Vignoli, G., & Hansen, T. M. (2021). 1D stochastic inversion of airborne time-domain electromagnetic data with realistic prior and accounting for the forward modeling error. *Remote Sensing*, *13*(19). https://doi.org/10.3390/rs13193881

Carrizo Mascarell, M., Werthmüller, D., & Slob, E. (2025). Supplementary material: Additional results. https://doi.org/10.5281/zenodo.17670207

Christiansen, A., Pedersen, J., Auken, E., Søe, N., Holst, M., & Kristiansen, S. (2016). Improved Geoarchaeological Mapping with Electromagnetic Induction Instruments from Dedicated Processing and Inversion. *Remote Sensing*, *8*(12), 1022. https://doi.org/10.3390/rs8121022

Constable, S., Parker, R., & Constable, C. (1987). Occam's inversion: A practical algorithm for generating smooth models from electromagnetic sounding data. *Geophysics*, *52*(3), 289–300. https://doi.org/10.1190/1.1442303

Deleersnyder, W., Dudal, D., & Hermans, T. (2022). Novel airborne EM image appraisal tool for imperfect forward modeling. *Remote Sensing*, *14*(22). https://doi.org/10.3390/rs14225757

Günther, T., Rücker, C., & Spitzer, K. (2006). Three-dimensional modelling and inversion of dc resistivity data incorporating topography — II. Inversion. *Geophysical Journal International*, *166*(2), 506–517. https://doi.org/10.1111/j.1365-246X.2006.03011.x

Heagy, L. J., Cockett, R., Kang, S., Rosenkjaer, G. K., & Oldenburg, D. W. (2017). A framework for simulation and inversion in electromagnetics. *Computers and Geosciences*, *107*, 1–19. https://doi.org/10.1016/j.cageo.2017.06.018

Kiyan, D., Rath, V., Muller, M. R., Ture, M. D., & Hodgson, J. (2022). 1-D inversion of frequency-domain airborne electromagnetic data using the open-source aempy toolbox. *Journal of Applied Geophysics*, *198*, 104562. https://doi.org/10.1016/j.jappgeo.2022.104562

Klose, T., Guillemoteau, J., Vignoli, G., & Tronicke, J. (2022). Laterally constrained inversion (LCI) of multi-configuration EMI data with tunable sharpness. *Journal of Applied Geophysics*, *196*, 104519. https://doi.org/10.1016/j.jappgeo.2021.104519

Ley-Cooper, A. Y., Macnae, J., & Viezzoli, A. (2010). Breaks in lithology: Interpretation problems when handling 2D structures with a 1D approximation. *Geophysics*, *75*(4), WA179–WA188. https://doi.org/10.1190/1.3483101

McLachlan, P., Blanchy, G., & Binley, A. (2021). EMagPy: Open-source standalone software for processing, forward modeling and inversion of electromagnetic induction data. *Computers & Geosciences*, *146*, 104561. https://doi.org/https://doi.org/10.1016/j.cageo.2020.104561

Monteiro Santos, F. A. (2004). 1-D laterally constrained inversion of EM34 profiling data. *Journal of Applied Geophysics*, *56*(2), 123–134. https://doi.org/10.1016/j.jappgeo.2004.04.005

Oldenburg, D. W., Heagy, L. J., Kang, S., & Cockett, R. (2020). 3D Electromagnetic modelling and inversion: A case for open source. *Exploration Geophysics*, *51*(1), 25–37. https://doi.org/10.1080/08123985.2019.1580118

Rücker, C., Günther, T., & Wagner, F. M. (2017). pyGIMLi: An open-source library for modelling and inversion in geophysics. *Computers and Geosciences*, *109*, 106–123. https://doi.org/10.1016/j.cageo.2017.07.011

Silic, J., Paterson, R., FitzGerald, D., & Archer, T. Comparing 1D and 2.5D AEM inversions in 3D geological mapping using a new adaptive inversion solver. In: In *14th International Congress of the Brazilian Geophysical Society; EXPOGEF, Rio de Janeiro, Brazil, 3-6 August 2015*. 2015, 184–189. https://doi.org/10.1190/sbgf2015-036

Taylor, R. (2023, April). Website of DualEM manufacturer: EM Induction (accessed on 21/04/2023). Retrieved April 21, 2023, from https://dualem.com/documents/em-induction/

Thalhammer, M. (2022, August). *Imaging of active layer characteristics through quasi-3D inversion of frequency-domain electromagnetic soundings* [Master thesis]. http://resolver.tudelft.nl/uuid:1a311a47-6f15-42c0-86e0-4b7a75ddc2cd

Wait, J. R. (1982, January). Chapter III - Electromagnetic Induction and Loop–Loop Coupling. In J. R. Wait (Ed.), *Geo-Electromagnetism* (pp. 101–139). Academic Press. https://doi.org/10.1016/B978-0-12-730880-7.50007-7

Werthmüller, D. (2017). An open-source full 3D electromagnetic modeler for 1D VTI media in Python: Empymod. *Geophysics*, *82*(6), WB9–WB19. https://doi.org/10.1190/geo2016-0626.1

Werthmüller, D., Mulder, W. A., & Slob, E. C. (2019). Emg3d: A multigrid solver for 3D electromagnetic diffusion. *Journal of Open Source Software*, *4*(39), 1463. https://doi.org/10.21105/joss.01463

Zhang, B., Yin, C., Liu, Y., Ren, X., Baranwal, V. C., & Xiong, B. (2021). 3D Inversion of large-scale frequency-domain airborne electromagnetic data using unstructured local mesh. *Geophysics*, *86*(5), E333–E342. https://doi.org/10.1190/geo2020-0243.1

5

PREDICTING 1D MODELS USING XGBOOST

But still try, for who knows what is possible...

Michael Faraday

The successful inversion of geophysical data has been a major challenge for decades. Conventional geophysical inversion techniques suffer from several limitations including computational cost, non-linearity and non-uniqueness of the inverse problem. Here, a novel approach based on machine learning inversion via gradient boosted decision trees is proposed to instantaneously estimate subsurface electrical conductivity layering from frequency domain electromagnetic induction data. To achieve this, an XGBoosted decision tree was trained on a large synthetic data set generated based on 1D electrical conductivity models. The accuracy of the proposed approach was examined using several synthetic scenarios. Moreover, the trained model was used to find subsurface electrical conductivity models from FDEM data measured along three transects in Ackerdijkse Plassen, The Netherlands. The XGBoost approach directly returns an electrical conductivity distribution from FDEM measurements without requiring prior information or iterations. The proposed strategy simplifies the inversion approach and allows for rapid and accurate estimation of the electrical conductivity of the subsurface from multiconfiguration FDEM data.

This chapter is being prepared for publication.

5.1. INTRODUCTION

In exploration geophysics, the goal is to extract information about the subsurface from geophysical data. Translating geophysical data into useful information usually requires geophysical inverse modelling, resulting in a model of the physical properties of the Earth's subsurface that explains the measured data. The frequency domain electromagnetic (FDEM) method is a non-invasive geophysical method used to image the spatial variability of the electrical conductivity in the subsurface, which reflects the geological features. Hence, it is an effective non-invasive approach for mapping soil properties, groundwater mapping, mineral exploration, saltwater intrusion mapping, etc.

The basic principles of FDEM are well understood from Chapters 1 and 2. As presented in Chapter 3, FDEM data inversion typically provides an estimate of the subsurface properties by iteratively updating and refining an initial subsurface model until an optimal model is obtained. Using the forward model, a response is numerically calculated. The model is considered optimal if the observed and the calculated data agree within some uncertainty bounds. If not, the initial model is adjusted to minimize the error between the calculated and measured response. Model updates are typically performed iteratively using a Gauss-Newton methodology and continue until an acceptable data fit criterion is satisfied or the data fit fails to improve (Tarantola, 2005).

In Chapter 3, the ill-posedness of the FDEM measurements inversion problem was discussed. The success of an iterative optimization of the solution strongly depends on the initial model, since the error space is highly nonlinear. Moreover, the solution is unstable with respect to the presence of noise. An alternative approach is to use machine learning methods to estimate the electrical conductivity models. Machine learning (ML), which is a data-driven approach, has become popular over the past decades and is useful for solving such inverse problems. An advantage of machine learning methods is that they can be implemented without knowledge of physical equations or theories. The challenges of machine learning lie in acquiring enough training data and selecting relevant parameters, which are essential to obtain an accurate model. Moreover, ML can capture complex, nonlinear relationships between observed data and subsurface parameters, which other inversion methodologies may struggle with. ML-based inversion, especially with sufficient training data, avoids the dependence on the initial model choice by learning a direct mapping from data to models. Examples of ML-based inversion applications into electromagnetic induction measurements have been presented in van 't Veen et al. (2022), Moghadas and Christiansen (2020) and Moghadas (2020).

An easy-to-apply ML tool is the Decision Tree (DT), which is a supervised ML technique that performs classification or regression based on observations (Alpaydin, 2014). A DT is a non-parametric supervised learning algorithm, which is utilized for both classification and regression tasks. It has a hierarchical tree structure, which consists of a root node, branches, internal nodes and leaf nodes. The goal is to create a DT model that predicts the value of a target variable by learning simple decision rules inferred from the data features. A tree can be seen as a piecewise constant approximation of the inverse of the forward function (Kuhn and Johnson, 2013). DTs are computationally inexpensive, but they can have limited predictive skill. To improve their performance, DTs are often augmented by ensemble learning methods such as bagging (Breiman, 1996) and boosting (Friedman, 2001).

In this study, we have applied the Extreme Gradient Boosting Decision Tree (XGBoost) as a predictive tool. Developed by T. Chen and Guestrin, 2016, XGBoost is an optimized ensemble algorithm based on the Gradient Boosting Decision Tree (GBDT) framework. This algorithm improves the predictive power and stability of the model by constructing and combining multiple decision trees, and has been widely applied in numerous studies (Tarwidi et al., 2023, J. Chen et al., 2024, Wang et al., 2023, Joshi et al., 2023, Zhang et al., 2024). Additionally, XGBoost introduces regularization terms and a second-order Taylor expansion to optimize the loss function, thus offering advantages such as preventing overfitting and rapid convergence. Therefore, XGBoost can theoretically achieve better predictive performance than classical optimization estimators with less computational resources.

This chapter aims to develop an XGBoost model to predict layered electrical conductivity models from 1D ground-based FDEM measurements. First, we explain the training of the XGBoost model and discuss the feature importance to understand the decision-making process of the model. Secondly, we show the prediction performance of the model with synthetic examples. Finally, we apply the XGBoost model prediction to field measurements and discuss the results.

5.2. METHODOLOGY

GENERATING SYNTHETIC DATA

The synthetic dataset for this study was generated using Equation 2.2 for the instrument configuration described in Figure 2.1. We assumed horizontally layered earth models with logarithmically increasing thickness (see Figure 5.1) until reaching a maximum depth of 9.52 m, considering the decreasing sensitivity of the measurements to depth. Several datasets with increasing number of layers were created and applied to the training and testing workflow explained in the following sections (see Figure 5.2). We stopped increasing layers when the RMSE values of the test dataset started increasing, reaching a maximum of 9 layers for the electrical conductivity model. The 9-th layer represents the remaining of the halfspace. Thus, the model has 9 electrical conductivity parameters,

$$\mathbf{m} = [\sigma_1, \sigma_2, ..., \sigma_9]. \tag{5.1}$$

The data vector corresponding to a model is:

$$\begin{aligned}\mathbf{d} = [&Q_{\text{HCP-2}}, Q_{\text{HCP-4}}, Q_{\text{HCP-8}}, Q_{\text{VCP-2}}, Q_{\text{VCP-4}}, Q_{\text{VCP-8}}, Q_{\text{PRP-2.1}}, Q_{\text{PRP-4.1}}, Q_{\text{PRP-8.1}},\\ &P_{\text{HCP-2}}, P_{\text{HCP-4}}, P_{\text{HCP-8}}, P_{\text{VCP-2}}, P_{\text{VCP-4}}, P_{\text{VCP-8}}, P_{\text{PRP-2.1}}, P_{\text{PRP-4.1}}, P_{\text{PRP-8.1}}],\end{aligned} \tag{5.2}$$

where the subscripts correspond to the coil geometry. The data measurements in $\mathbf{d}$ are transformed into amplitudes and phases of the electromagnetic field.

Here, amplitude $A = \sqrt{Q^2 + P^2}$ and phase $\varphi = \arctan(Q/P)$. Therefore, the data vector $\mathbf{d}$ is transformed to:

$$\begin{aligned}\mathbf{d} = [&A_{\text{HCP-2}}, A_{\text{HCP-4}}, A_{\text{HCP-8}}, A_{\text{VCP-2}}, A_{\text{VCP-4}}, A_{\text{VCP-8}}, A_{\text{PRP-2.1}}, A_{\text{PRP-4.1}}, A_{\text{PRP-8.1}},\\ &\varphi_{\text{HCP-2}}, \varphi_{\text{HCP-4}}, \varphi_{\text{HCP-8}}, \varphi_{\text{VCP-2}}, \varphi_{\text{VCP-4}}, \varphi_{\text{VCP-8}}, \varphi_{\text{PRP-2.1}}, \varphi_{\text{PRP-4.1}}, \varphi_{\text{PRP-8.1}}].\end{aligned} \tag{5.3}$$

We generated 800,000 data measurements corresponding to randomly chosen 9-layered earth models with a wide range of electrical conductivities, from 1 to 1000 mS/m. We

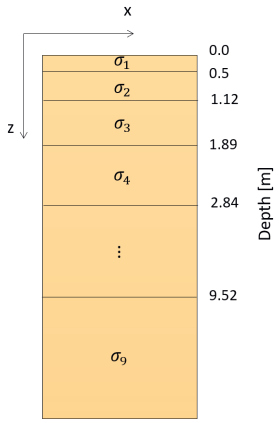


Figure 5.1: 9-Layered earth electrical conductivity model used to train the XGBoost predictor.

tested the training data sets in increasing intervals of 100,000 samples until obtaining no improvement in the validation loss. The final dataset size was 400,000 samples. The electrical conductivity values were chosen randomly. The dataset was subsequently split into training, validation and test subsets using 60, 20 and 20 % of the data, respectively. The training subset is used to train the XGBoost model, while the validation subset is used to evaluate the performance of the XGBoost model during the training procedure. The test subset is applied after training for an unbiased evaluation of the algorithm.

EXTREME GRADIENT BOOSTING (XGBOOST)

As mentioned in the introduction, GBDT, proposed by Friedman (2001), adopts the gradient descent algorithm to minimize the objective function by generating a new tree based on all previous trees. XGBoost is an optimized ensemble tree model based on the GBDT framework, effectively applicable for both classification and regression tasks (T. Chen and Guestrin, 2016). In the next paragraphs, we explain the scheme of a tree ensemble.

For a given data set with n examples and m features, $\mathscr{D} = \{(\mathbf{x}_i, y_i)\}$ $(|\mathscr{D}| = n, \mathbf{x}_i \in \mathbb{R}^m, y_i \in \mathbb{R})$, a tree ensemble model uses K additive functions to predict the output.

$$\hat{y}_i = \phi(\mathbf{x}_i) = \sum_{k=1}^{K} f_k(\mathbf{x}_i), \quad f_k \in \mathscr{F}, \tag{5.4}$$

where $\mathbf{x}_i$ is the input of the tree, y_i and $\hat{y}_i$ are the true and predicted output values of the i_{th} sample, respectively, f_k and K represent the kth tree and the total number of trees in the model, respectively. Consequently, $\mathscr{F} = \{f(\mathbf{x}) = w_{q(\mathbf{x})}\}$ $(q : \mathbb{R}^m \to T, w \in \mathbb{R}^T)$ is the space of regression trees. Here, q represents the structure of each tree that maps an example to the corresponding leaf index. T is the number of leaves in each tree. Each f_k corresponds to an independent tree structure q and leaf weights w.

For regression tasks such as continuous data prediction, the XGBoost algorithm can use the Classification and Regression Tree (CART) scheme (Breiman et al., 1984) as its

base learner to construct its objective function $\mathscr{L}$, which includes a loss function $l(y_i, \hat{y}_i)$ and a regularization term $\Omega(f_k)$, defined as:

$$\mathscr{L} = \sum_{i=1}^{n} l(y_i, \hat{y}_i) + \sum_{k=1}^{K} \Omega(f_k). \tag{5.5}$$

The parameter $\Omega(f_k)$ is defined as:

$$\Omega(f_k) = \zeta T_k + \frac{1}{2}\xi \sum_{j=1}^{T_k} w_{k,j}^2, \tag{5.6}$$

where T_k is the total number of leaf nodes in the kth tree, $w_{k,j}$ represents the weight of the jth leaf node in the kth tree. The parameters ζ and ξ are constants that represent the penalty coefficients for T_k and w, respectively.

Equation 5.5 is solved iteratively with:

$$\mathscr{L}^{(t)} = \sum_{i=1}^{n} l\left(y_i, \hat{y}_i^{(t-1)} + f_t(x_i)\right) + \Omega(f_t) + C, \tag{5.7}$$

where $\hat{y}_i^{(t-1)}$ is the prediction result from the previous iteration, $f_t(x_i)$ represents the residual fitting of $\hat{y}_i^{(t-1)}$ using the tth tree and C is a constant representing the sum of the weights from the first tree to the $(t-1)$th tree. The loss function in the equation can be approximated using a second-order Taylor expansion,

$$\tilde{\mathscr{L}}^{(t)} \cong \sum_{i=1}^{n} \left[l\left(y_i, \hat{y}_i^{(t-1)} + g_i f_t(x_i) + \frac{1}{2} h_i f_t^2(x_i)\right)\right] + \Omega(f_t), \tag{5.8}$$

where g_i and h_i represent the first and second derivatives of the loss function. If the constant term C is omitted and the regularization term $\Omega(f_t)$ expanded, then a simplified objective function can be obtained,

$$\begin{aligned} \tilde{\mathscr{L}}^{(t)} &= \sum_{i=1}^{n} \left[g_i f_t(x_i) + \frac{1}{2} h_i f_t^2(x_i)\right] + \zeta T_t + \frac{1}{2}\xi \sum_{j=1}^{T_t} w_{t,j}^2 \\ &= \sum_{j=1}^{T_t} \left[\left(\sum_{i \epsilon I_j} g_i \right) w_{t,j} + \frac{1}{2} \left(\sum_{i \epsilon I_j} h_i + \xi \right) w_{t,j}^2 \right] + \zeta T_t, \end{aligned} \tag{5.9}$$

where $I_j = \{i | q(\mathbf{x}_i) = j\}$ is the instance set of leaf j. Then, by taking the derivative of the objective function with respect to $w_{t,j}$ and making it equal to 0, we obtain the optimal weight $w_{t,j}^*$ as:

$$w_{t,j}^* = -\frac{\sum_{i \epsilon I_j} g_i}{\sum_{i \epsilon I_j} h_i + \xi}. \tag{5.10}$$

Finally, we substitute the optimal weight $w_{t,j}^*$ into Equation 5.9, providing the optimal objective function:

$$\tilde{\mathscr{L}}^{(t)*} = -\frac{1}{2} \sum_{j=1}^{T_t} \frac{\left(\sum_{i \epsilon I_j} g_i\right)^2}{\sum_{i \epsilon I_j} h_i + \xi} + \zeta T_t, \tag{5.11}$$

The * superscript indicates the tree structure with the best prediction score.

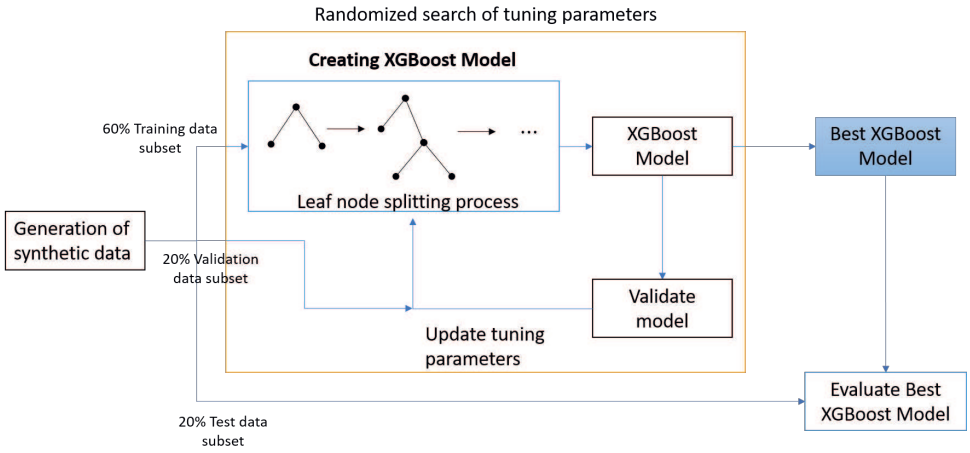


Figure 5.2: Workflow for training, validation and testing of the XGBoost model.

5

WORKFLOW

We illustrate the training and prediction workflow in Figure 5.2. Initially, we split the synthetic data into training, validation, and test subsets. The proposed workflow uses noise-free measurements for the training. The hyperparameters of the XGBoost model were chosen using a hyperparameter tuning process, the random search, as proposed by Bergstra and Bengio (2012). In the random search, a number of hyperparameter combinations are tested, and cross-validated with slices of the training data subset. The different predictor scores are compared. The score is obtained from the RMSE values of each predictor using the validation set, which are calculated as described in Equation 2.6. The random search indicates the hyperparameters for the predictor with the best score. Then, we train an XGBoost model with the hyperparameters obtained from the random search. We apply an early stopping approach to avoid overfitting the data by stopping the training procedure when the loss does not improve in 50 consecutive learning rounds. The best XGBoost model is then evaluated with the test data subset. Finally, we use the best XGBoost model chosen by the workflow to estimate the electrical conductivity models in the synthetic examples.

5.3. RESULTS AND DISCUSSION

After training and validating the XGBoost model, we present the results in the training and test subsets. In Figure 5.3, the parameters of the true versus predicted model are presented for the test subset. It is clear from the RMSE values that, in general, the shallow layers are better predicted than the deeper layers, except for the 9th layer, which constitutes the rest of the halfspace. This makes sense if we consider the decreasing sensitivity of the measurements with depth. Moreover, we also observe that from σ_4 and deeper layers, for smaller conductivity values (left bottom of the subfigures), the values are overestimated. In contrast, for larger conductivity values (top right of the subfigures), the values are underestimated. This problem arises from the rapidly decreasing sensitivity of

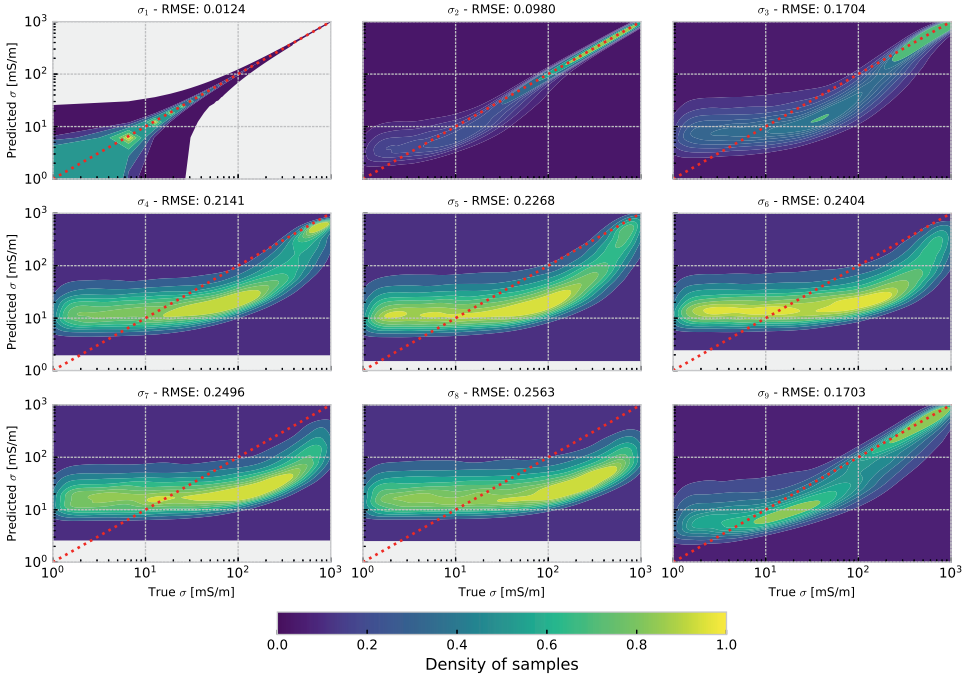


Figure 5.3: True vs. Predicted electrical conductivity model parameters. The NRMSE value of all predictions for each parameter is given. The red line represents a perfect prediction.

electromagnetic induction measurements with depth. As a result, deep conductivities are weakly constrained by the data. The machine learning model, therefore, produces predictions that regress toward the mean conductivity of the training data, leading to overestimation of low values and underestimation of high values at depth. The error distribution is also shown in Figure 5.4, where histograms of the error frequency above and below 10 mS/m are shown. It is clear that for conductivities larger than 10 mS/m, the error spreads to higher predictions. While for conductivities below 10 mS/m the error spreads to smaller predictions.

In Figure 5.5, we present the importance of each feature, or data parameter, in the prediction of each model parameter as pie charts. In the shallowest layer (σ_1) the most important feature belongs to the VCP configuration, which makes sense since this configuration is sensitive to shallow depths (as demonstrated in Figures 2.4 and 2.5). In layers σ_2 and σ_3, the offset configuration of PRP 2.1 m is of greater importance. The PRP and HCP largest offset configurations start to present more influence in the prediction from σ_6 onwards. This clearly illustrates how the physical phenomenon is learned by the XGBoost algorithm, since the largest offsets are the most sensitive to deeper depths. This Figure also shows how the combination of the different configurations and measurement components all influence the prediction.

In Figures 5.6 and 5.7, we present the results of the XGBoost prediction of the electrical conductivity for 10 random earth models from the training and test subsets, re-

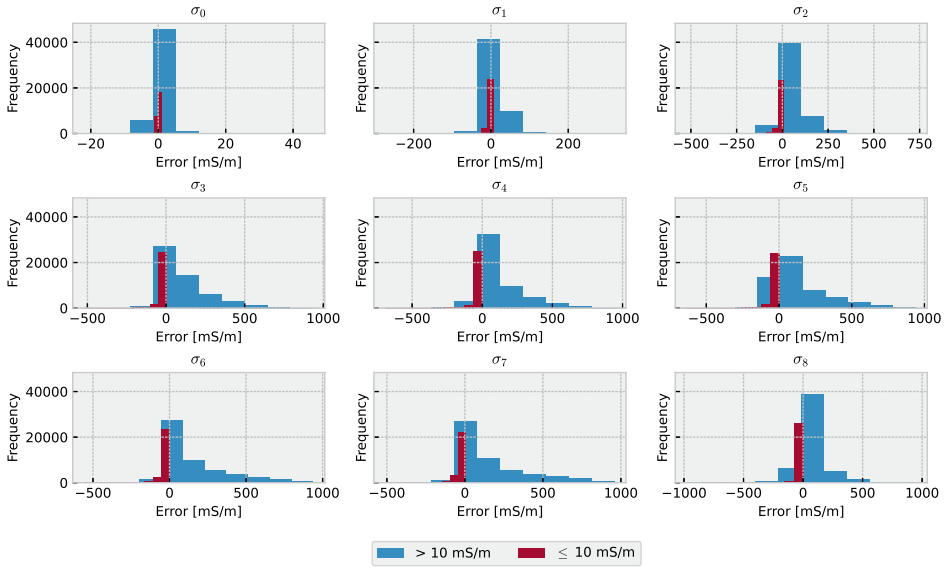


Figure 5.4: Error frequency histograms. In blue, errors for conductivity values below 10 mS/m. In red, errors for conductivity values larger than 10 mS/m.

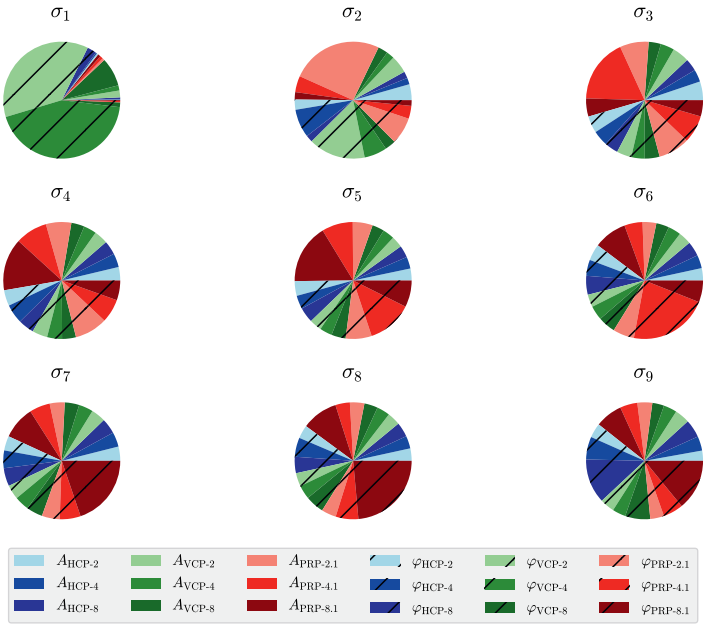


Figure 5.5: Feature importance for each model parameter. The lighter colors belong to small offsets. The darkest colors belong to larger offsets. The hatching represents the phase component of the measurement.

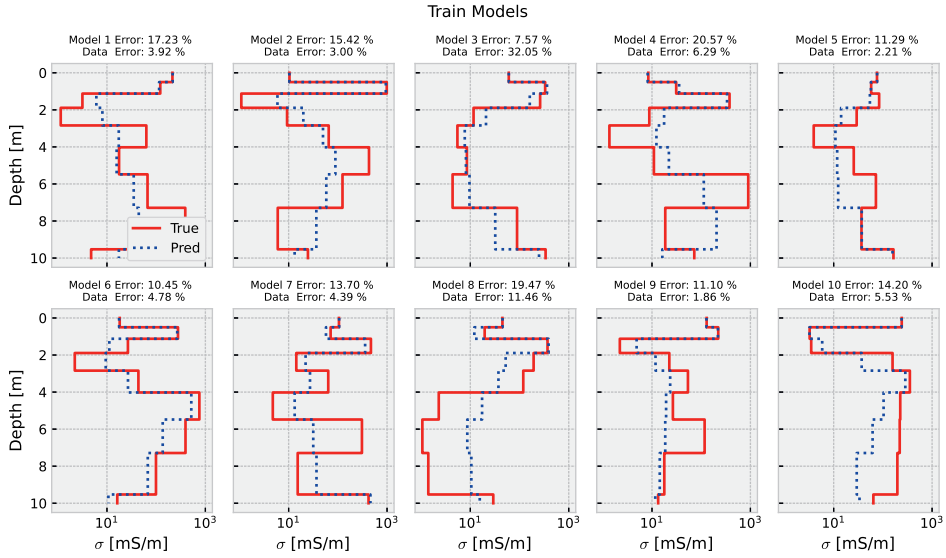


Figure 5.6: XGBoost prediction results in training models. The error values are given for the model prediction and their corresponding data measurements.

spectively. The training earth models are learned by the XGBoost model, therefore the predictions have a mean data error of ≈ 5%. The models are not perfectly learned, since there is regularization in the process to avoid overfitting. In the test models case, the XGBoost model has not seen these samples previously. For this case the predictions overall reproduces the general trend of the conductivity distribution, with a mean data error of ≈ 10%. It is clear for both the training and test earth models that the predictions worsen with depth, especially for low conductivity layers.

NUMERICAL EXAMPLES

We performed an estimation using the XGBoost predictor for two 3-layered transects illustrated in Figures 5.8 and 5.9, for a middle conductive body and a middle resistive body, respectively. We tested the prediction for three cases: noise-free, 5% and 10% normally distributed noise in the measurements. The resulting predicted models follow the general trend of the electrical conductivity distribution of the true models. In both subsurface models, the predictor is able to obtain the true middle layer geometry. Although the boundaries of the layers are not so clearly defined, the XGBoost prediction is closer to the true model than the results of the Gauss-Newton optimization presented in Chapter 3 subfigures 3.8 and 3.9. In Figures 5.10 and 5.11, the data fit of the true and predicted models is shown for the noise-free case.

Moreover, we used the predicted estimations as initial models in a Gauss-Newton optimization scheme (see Chapter 3, section 3.3). The results of these estimations are also shown in Figures 5.8 and 5.9. In XGBoost + GN, the resulting estimations have a better data fit than with XGBoost only, since the optimization tries to obtain a model

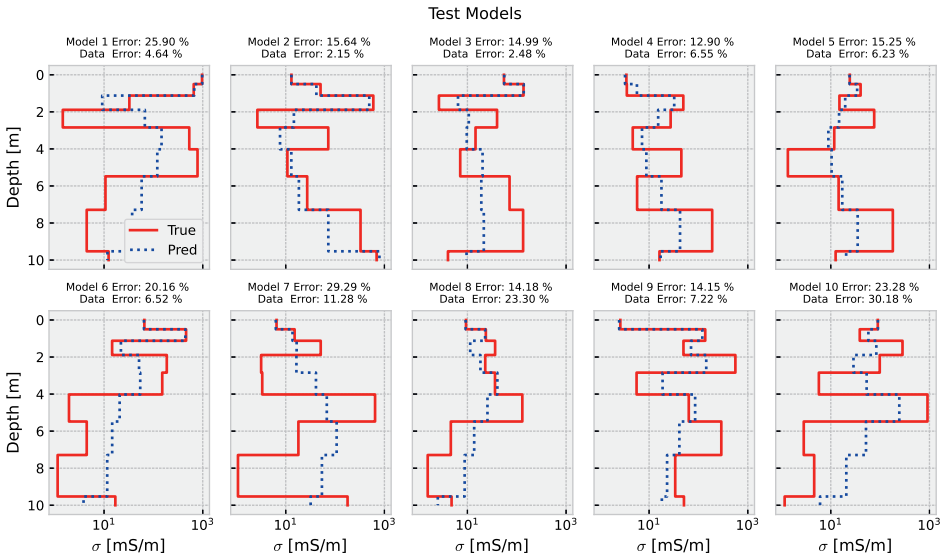


Figure 5.7: XGBoost prediction results in test models. The error values are given for the model prediction and their corresponding data measurements.

that explains the data within a certain tolerance. However, the model is less accurate than the XGBoost predictions, in both cases. The data fit of these estimations is also defined in Figures 5.10 and 5.11 for the noise-free case. Both the XGBoost and XGBoost + GN results are similarly affected by increasing levels of noise in the measurements.

In both the numerical examples of the middle conductive and the middle resistive body, using the Gauss-Newton optimization to improve the XGBoost prediction results increases the overall conductivity of the subsurface to better explain the measurements. This can be explained as a larger sensitivity of the measurements to the conductive parts of the subsurface, bypassing the resistive parts. The advantage of using the XGBoost algorithm lies in the fact that the prediction model has also learned the relationship between the measurements to resistive parts of the subsurface, as illustrated by these results.

An additional advantage of the XGBoost predictor over a Gauss-Newton optimization is the ability to make decisions and identify the most important variables (data parameters) and their complex interactions to make a prediction. This is shown in the feature importance plots (see Figure 5.5), where several data variables are given a greater influence in the prediction of a given model variable. This is important since the FDEM instrument provides measurements from different coil geometries, which are not sensitive to the same volumes of the subsurface.

FIELD CASE APPLICATION

We applied the XGBoost prediction methodology to the FDEM measurements obtained in Ackerdijkse Plassen location in the Netherlands (Figure 2.10). We used the workflow

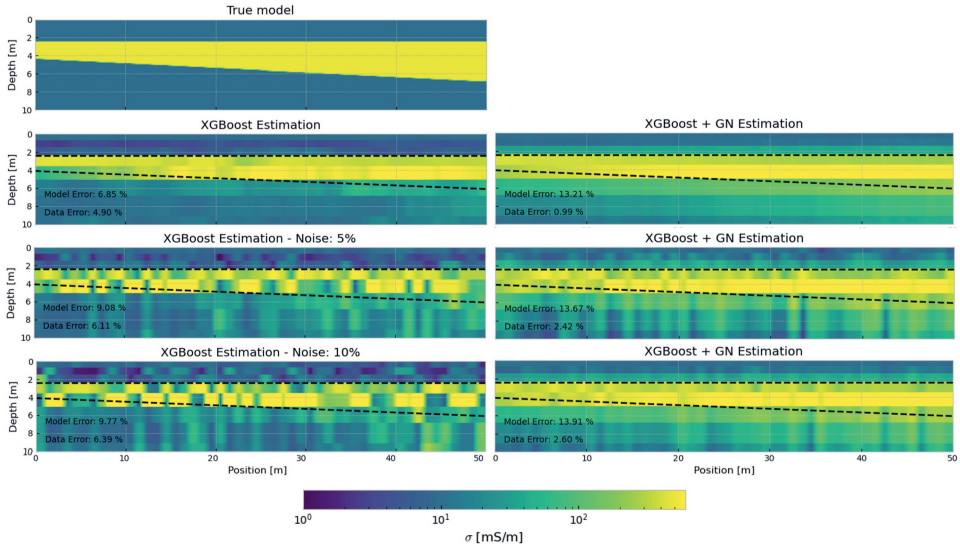


Figure 5.8: Numerical example: Middle conductive body. Top: True model. Second row: XGBoost (left) and XGBoost + GN (right) estimated models. Third row: 5% noise case for XGBoost (left) and XGBoost + GN (right) estimated models. Fourth row: 10% noise case for XGBoost (left) and XGBoost + GN (right) estimated models. True positions of the boundaries are shown in black dashed lines.

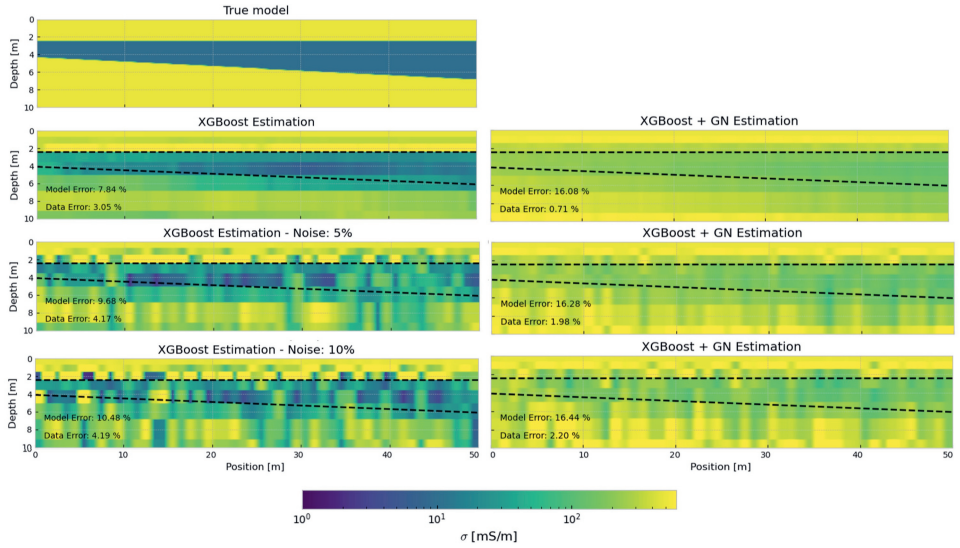


Figure 5.9: Numerical example: Middle resistive body earth model. Top: True model. Second row: XGBoost (left) and XGBoost + GN (right) estimated models. Third row: 5% noise case for XGBoost (left) and XGBoost + GN (right) estimated models. Fourth row: 10% noise case for XGBoost (left) and XGBoost + GN (right) estimated models. The true positions of the layer boundaries are illustrated in black dashed lines.

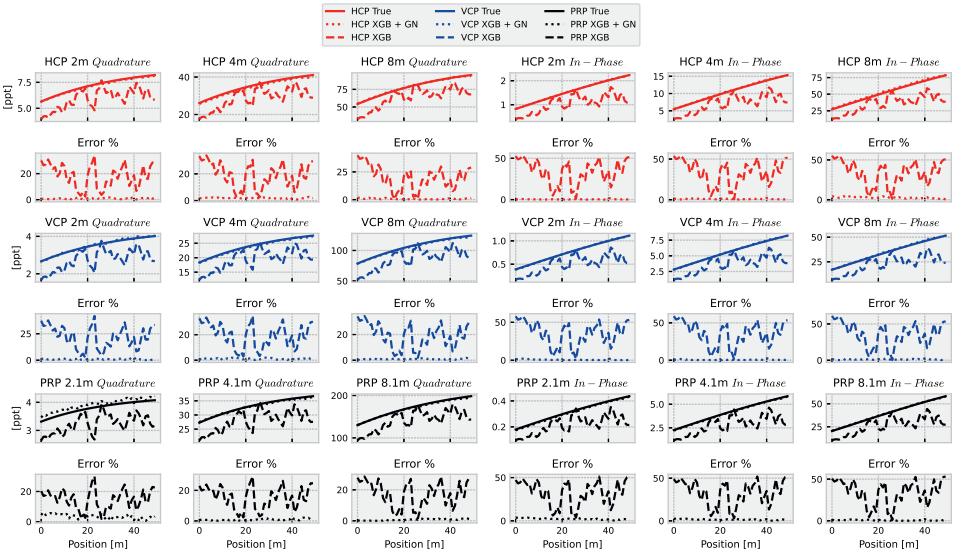


Figure 5.10: Data fit of true and simulated measurements for the estimated models. Middle conductive body case.

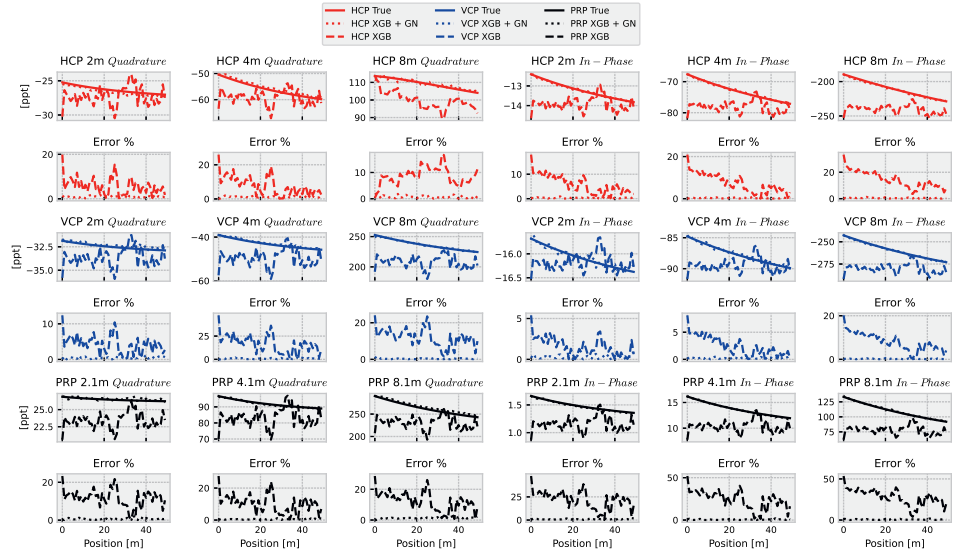


Figure 5.11: Data fit of true and simulated measurements for the estimated models. Middle resistive body case.

presented in Figure 5.2 to choose the hyperparameters, train, validate and test the algorithm as mentioned in the previous sections. We acquired measurements using only the HCP and VCP coil configurations, and used offsets larger than 2 meters as suggested by the manufacturer (Taylor, 2023). We present the results of the predictions for three subsurface trajects (indicated in Figure 2.10), using both XGBoost and XGBoost + GN prediction methods (see Figure 5.12). The datafit of the predicted responses is shown in Figure 5.13.

The results of XGBoost and XGBoost + GN differ greatly. In the XGBoost predicted trajects we observe a resistive layer between 5.5 - 8 m depth, with a conductivity of approximately 20 - 50 mS/m, that is not present in the XGBoost + GN prediction. We deduce that, as we observed in the synthetic case, the Gauss-Newton optimization increases the conductivity of the subsurface to better explain the measurements. However, this does not necessarily mean that the XGBoost + GN estimation is closer to reality. As it was displayed in the synthetic case, the XGBoost algorithm manages to better describe the resistive bodies between larger conductivity layers. We believe the machine learning algorithm, since learning from previous models, can learn the relationship between the measurements and resistive bodies. However, the Gauss-Newton optimization is driven by the sensitivity of the measurements to conductivity in the subsurface, and therefore, while improving the data fit, resistive features might be lost.

We already know from previous chapters that Gauss-Newton optimization alone is not sufficient to predict 1D subsurface models with more than 3 layers. The XGBoost algorithm, although predicting with limitations (due to underestimating conductivities larger than 10 mS/m and overestimating conductivities under 10 mS/m with depth), still provide us with an approach that predicts the trend of the distribution of electrical conductivity in the subsurface for a 1D earth with 9 layers. A further combination of XGBoost with the Gauss-Newton minimization improves the data fit, but might not improve the model prediction.

5.4. CONCLUSIONS

This study proposes a novel approach for 1D inversion of FDEM data using extreme gradient boosted regression tree algorithms (XGBoost). The recent availability of fast and easy 1D electromagnetic modellers allowed us to perform a large number of FDEM forward models necessary to train a machine learning algorithm to predict the 1D distribution of electrical conductivity of the subsurface. An XGBoost model was trained on a sufficiently large amount of subsurface models to be able to generalize to unseen data. To construct a highly accurate XGBoost model, hyperparameter tuning has been performed using the grid search method.

The 1D numerical examples demonstrated that the trained predictor allows for accurate subsurface characterization for models that lie within the training conductivity range. Compared with the existing conventional inversion techniques, the proposed approach offers several key advantages. This technique estimated earth models from FDEM data in a few milliseconds without any iterations. Moreover, the trained algorithm returns the subsurface conductivity distribution without using any initial model. As a consequence, this approach does not suffer from the non-uniqueness issue that is typically encountered using classical inversion techniques.

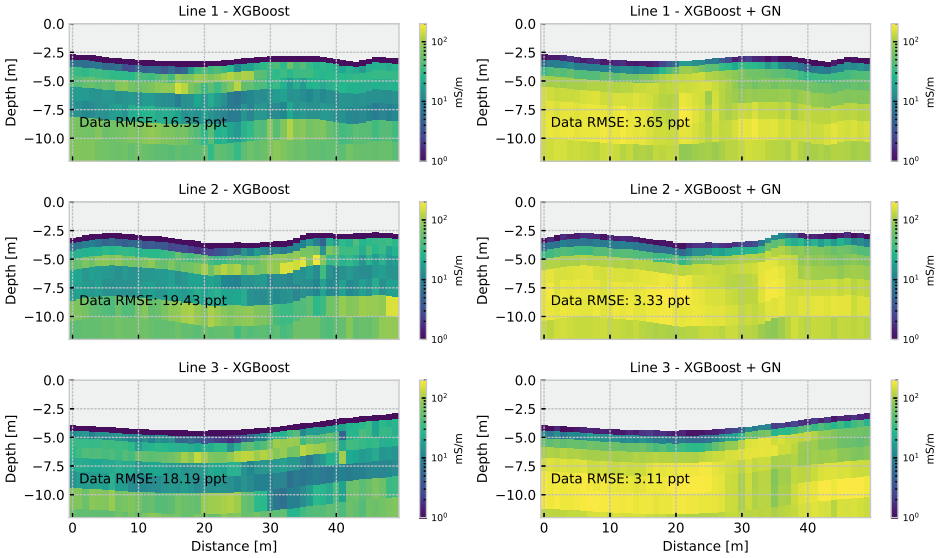


Figure 5.12: Field lines predicted using XGBoost algorithm (left) and XGBoost + GN (right).

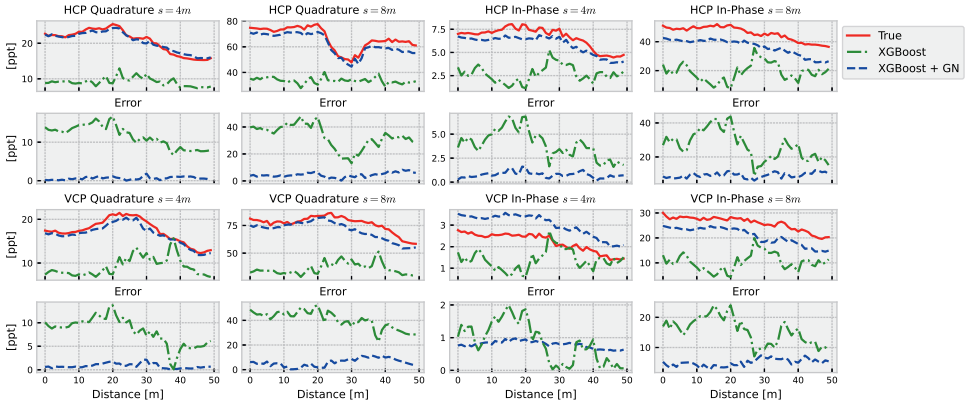


Figure 5.13: Data fit for Line 1. We observe that, similarly to the numerical cases, the XGBoost + GN response has lower error than the XGBoost predicted model response.

The comparison between the machine learning predictions and subsequent Gauss-Newton optimization demonstrates the inherent non-uniqueness of FDEM inversion. While Gauss–Newton optimization further reduces data misfit, it tends to suppress resistive features that are weakly constrained by the measurements. In contrast, the machine learning approach preserves such features by using learned subsurface correlations to the measurements. This indicates that improved data fit does not necessarily correspond to improved model fidelity, particularly at depth.

This study illustrates how a machine learning algorithm can be trained successfully to obtain predictions of electrical conductivity models from FDEM measurements in a computationally efficient manner. The results demonstrate that XGBoost models can be a valuable tool to predict the electrical conductivity distribution of the subsurface.

DATA AVAILABILITY

The codes and data used in this chapter is available via Zenodo (Link).

BIBLIOGRAPHY

Alpaydin, E. (2014). Decision trees. In *Introduction to machine learning* (pp. 213–238). MIT Press. http://ieeexplore.ieee.org/document/6284943

Bergstra, J., & Bengio, Y. (2012). Random search for hyper-parameter optimization. *J. Mach. Learn. Res.*, *13*, 281–305. https://doi.org/10.5555/2188385.2188395

Breiman, L. (1996). Bagging predictors. *Machine Learning*, *24*, 123–140. https://doi.org/10.1007/BF00058655

Breiman, L., Friedman, J., Olshen, R., & Stone, C. (1984). *Classification and regression trees (1st ed.)* Chapman; Hall/CRC. https://doi.org/10.1201/9781315139470

Chen, J., You, J., Wei, J., Dai, Z., & Zhang, G. (2024). Interpreting XGBoost predictions for shear-wave velocity using shap: Insights into gas hydrate morphology and saturation. *Fuel*, *364*, 131145. https://doi.org/10.1016/j.fuel.2024.131145

Chen, T., & Guestrin, C. (2016). XGBoost: A scalable tree boosting system. *Proceedings of the 22nd ACM SIGKDD International Conference on Knowledge Discovery and Data Mining*, 785–794. https://doi.org/10.1145/2939672.2939785

Friedman, J. H. (2001). Greedy function approximation: A gradient boosting machine. *Annals of Statistics*, *29*, 1189–1232. https://api.semanticscholar.org/CorpusID:39450643

Joshi, A., Vishnu, C., Mohan, C. K., & Raman, B. (2023). Application of XGBoost model for early prediction of earthquake magnitude from waveform data. *Journal of Earth System Science*, *133*. https://doi.org/10.1007/s12040-023-02210-1

Kuhn, M., & Johnson, K. (2013). Regression trees and rule-based models. In *Applied predictive modeling* (pp. 173–220). Springer New York. https://doi.org/10.1007/978-1-4614-6849-3_8

Moghadas, D. (2020). One-dimensional deep learning inversion of electromagnetic induction data using convolutional neural network. *Geophysical Journal International*, *222*(1), 247–259. https://doi.org/10.1093/gji/ggaa161

Moghadas, D., & Christiansen, A. V. (2020). Soil electrical conductivity imaging using a neural network-based forward solver: Applied to large-scale Bayesian electromagnetic inversion. *Journal of Applied Geophysics*, *176*, 104012. https://doi.org/10.1016/j.jappgeo.2020.104012

Tarantola, A. (2005). *Inverse Problem Theory and Methods for Model Parameter Estimation*. Society for Industrial; Applied Mathematics. https://doi.org/10.1137/1.9780898717921

Tarwidi, D., Pudjaprasetya, S. R., Adytia, D., & Apri, M. (2023). An optimized XGBoost-based machine learning method for predicting wave run-up on a sloping beach. *MethodsX*, *10*, 102119. https://doi.org/10.1016/j.mex.2023.102119

Taylor, R. (2023, April). Website of DualEM manufacturer: EM Induction (accessed on 21/04/2023). Retrieved April 21, 2023, from https://dualem.com/documents/em-induction/

van 't Veen, K. M., Ferré, T. P. A., Iversen, B. V., & Børgesen, C. D. (2022). Using machine learning to predict optimal electromagnetic induction instrument configurations for characterizing the shallow subsurface. *Hydrology and Earth System Sciences*, *26*(1), 55–70. https://doi.org/10.5194/hess-26-55-2022

Wang, T., Bian, Y., Zhang, Y., & Hou, X. (2023). Classification of earthquakes, explosions and mining-induced earthquakes based on XGBoost algorithm. *Computers Geosciences*, *170*, 105242. https://doi.org/10.1016/j.cageo.2022.105242

Zhang, J., Wang, R., Jia, A., & Feng, N. (2024). Optimization and application of XGBoost logging prediction model for porosity and permeability based on K-means method. *Applied Sciences*, *14*(10). https://doi.org/10.3390/app14103956

6

Conclusions and Recommendations

One never notices what has been done;
one can only see what remains to be done.

Marie Skłodowska-Curie

This thesis discusses methods to improve the accuracy, efficiency, and reliability of estimations of electrical conductivity distributions in the subsurface from frequency-domain electromagnetic induction (FDEM) measurements, by analyzing the information contained in the measurements, the performance of inversion methods and carefully analyzing their limitations.

The results of the study show that the measurements are sensitive to the distribution of electrical conductivity in all three dimensions. The relationships are highly non-linear and the inversion problem is already not well posed for a simple 3-layered 1D model. The ill-posedness of the inversion problem limits the estimation possibilities for cases where there is no additional information of the subsurface. Many of the inversion methods used currently in the geophysical industry combine different geophysical methods to avoid this limitation. However, there are instances where only non-invasive FDEM methods can be used and we provide insights based on cases using only these measurements.

A method using machine learning algorithms is proposed. The advantage of using a machine learning method corresponds, in this case, to the ability of learning the complex non-linear relationships between the measurements and the subsurface model, also providing larger importance to the more sensitive loop-loop configurations. Moreover, the trained algorithm does not require initial information of the subsurface. In this chapter, we discuss the main findings of this thesis.

6.1. CONCLUSIONS

In Chapter 2, we used a semi-analytical FDEM modeller to calculate in-phase and quadrature components for horizontally layered earth models. We calculated the sensitivity of the FDEM measurements to changes in the conductivity of the earth. This analysis demonstrated that both both quadrature and in-phase components contain essential and complementary sensitivity to subsurface conductivity, demonstrating the importance of using the full complex measurement in the inversion of these measurements. We also demonstrated that a near real-time estimation of two-layered models can be obtained using a global search inversion scheme. This global search inversion method outperforms using low induction number approximations, which fail even under low induction number conditions.

In Chapter 3, we demonstrated that for two-layered 1D earth models, the inverse problem is well-posed when both in-phase and quadrature components are used, enabling stable and unique solutions with Gauss–Newton inversion. In contrast, the three-layered problem exhibits non-uniqueness, flat misfit regions, and numerous local minima, making the inverse problem fundamentally ill-posed with the acquisition configuration studied. Moreover, the inversion problem is also unstable in the presence of noise. Neither Gauss–Newton nor global search reliably resolves three-layered structures, particularly for resistive middle layers, confirming that for this instrument configuration, FDEM data alone is insufficient without strong prior information or alternative measurement setups.

In Chapter 4, we analyze systematically how instrument tilt, topography, dipping layers, and lateral conductivity contrasts introduce significant distortions in FDEM measurements with respect to a 1D layered earth model response. Consequently, these distortions propagate into the subsurface estimations for inversion methods that use internally 1D forward modellers. Both piecewise 1D and laterally constrained inversion schemes perform well only under near-ideal 1D conditions (flat ground, small dips, gentle conductivity variations). Piecewise 1D inversion overall better resolves first-layer thickness but is highly sensitive to distortions and produces spurious oscillations. Laterally constrained inversion is more stable and robust against noise, but at the cost of thickness accuracy. However, neither method adequately compensates for significant 2D/3D geological effects, confirming that proper assessment of the 1D assumption is essential before applying these inversion methods.

In Chapter 5, we propose a machine learning XGBoost based inversion strategy, which successfully maps FDEM data to 1D electrical conductivity profiles. We make use of the advantage of the XGBoost algorithm to handle non-linearly related measurements and complex interactions of the different loop-loop configurations. This algorithm, once it is trained on a sufficiently broad set of synthetic data generated using 1D modelling, provides estimations in milliseconds, requires no initial model and avoids the iterative and non-unique characteristics of the optimization inversion approach. The XGBoost predictor was tested with numerical 3-layered models, proving better results than the Gauss-Newton approach, even in noise presence. This demonstrates that advanced machine-learning methods can overcome limitations inherent to traditional inversion, particularly for speed and non-uniqueness issues. Although their performance depends on the representativeness of the training dataset and the sensitivity of the measurements

to the subsurface parameters.

The results of this thesis show that the full use of data (in-phase + quadrature) provides more complete subsurface information for reliable inversion. However, as we demonstrated, the FDEM inversion problem is already ill-posed for 1D 3-layered earth models, requiring prior information. Assuming we have prior information of the subsurface, the model complexity and geometry of the instrument with respect to topography conditions strongly control the FDEM measurements. Therefore, the assumptions with respect to these factors must be carefully considered, since they impact the performance of FDEM inversion. Machine learning offers a new pathway for robust and rapid conductivity estimation, provided that training data are representative of the problem we are determined to resolve.

6.2. RECOMMENDATIONS

The FDEM geophysical method shows great potential as a tool for fast and non-invasive estimation of the electrical conductivity of the subsurface. As we demonstrated, it is quite sensitive to changes in the distribution of the conductivity in depth as well as spatially. To better harness the potential of this method, we put forward these recommendations:

METHODOLOGY

Both quadrature and in-phase components of the measurement should be included in the inversion workflows for improved sensitivity and solution uniqueness. Additional efforts should be given from instrument developers to provide accurate in-phase measurements. An alternative would be to provide for both amplitude and phase.

Moreover, the combination of multi-frequency, multi-offset and multi-elevation configurations should be investigated. It has been mentioned in previous studies that multi-frequency and multi-offset instruments have sensitivity to different volumes of the subsurface (Blanchy et al., 2024). The combination of complementary sensitivities might add information to better constrain the inversion problem.

For estimations with multi-layered models, with three-layered or more, when using optimization inversion approaches it is necessary to incorporate prior geological constraints or consider additional frequencies, coil separations, or survey geometries, to better constrain the solution.

Before applying inversion methodologies, it is recommended to evaluate the validity of the survey design assumptions, especially for topography, layer dip, and lateral conductivity variations. For surveys in environments with moderate or strong 3D electrical conductivity variations, one should consider topography 2D/3D forward modelling, or 2D/3D inversion techniques.

Expand machine-learning-based inversion by increasing the range and diversity of training models, incorporating noise and realistic measurement distortions into the training data, evaluating model generalization on varied geological settings.

NOISE

In this thesis, the results of including noise to the inversion problem showed a large impact for inversion estimations. Moreover, we demonstrated with synthetic examples the instability of the inversion problem to noise even in the two-layered 1D case. It is important to consider the large uncertainty of the results when the measurements contain noise. Advanced signal processing techniques, statistical filtering, and machine learning approaches could be explored for noise reduction and pattern recognition.

6.3. FUTURE RESEARCH

This thesis provides insights into several areas where additional research could help mitigate the challenges associated with FDEM forward modelling and inversion. Firstly, there is a clear need for the development of more efficient 2D and 3D FDEM forward modelling algorithms. Although 1D assumptions have enabled fast, cost-effective, and practical surveys, they are often inadequate in areas characterized by complex geology or highly heterogeneous near-surface environments. In such settings, lateral variations in conductivity can significantly distort the electromagnetic response, leading to biased or oversimplified inversion results. Future work should therefore prioritize the development of computationally efficient 3D forward solvers that balance accuracy with speed, potentially through numerical optimization, adaptive meshing, or high-performance computing strategies. Making robust 3D modelling tools more accessible will be essential for integrating them into routine inversion workflows and expanding their applicability in both research and industry contexts.

Secondly, further investigation is required to better understand and exploit the information content of multi-frequency and multi-offset FDEM systems. These systems provide complementary sensitivity to different depths and spatial scales, offering the potential to better constrain multi-layer conductivity models. However, the tradeoffs between model parameters, the impact of noise, and the optimal configuration of frequencies and coil separations can be explored further. Future research should focus on systematic sensitivity analyses, resolution studies, and uncertainty quantification frameworks to determine how acquisition design influences model reliability. Improved strategies for joint inversion of multi-configuration datasets may significantly enhance the robustness and interpretability of subsurface models.

Thirdly, the usefulness and limitations of correction methods for topographic variations and sensor tilting effects in FDEM measurements warrant more comprehensive investigation. In real world surveys, deviations from ideal instrument geometry can introduce systematic errors that propagate into inversion results. Future studies should evaluate these correction approaches through synthetic modelling and controlled field experiments, with the aim of establishing best practice guidelines and survey strategies that explicitly account for 3D effects and measurement uncertainties.

Finally, extending machine learning–based inversion approaches to 2D or pseudo-3D frameworks represents a promising research direction. While current implementations often rely on 1D assumptions, incorporating lateral variability into data-driven inversion models could substantially improve performance in complex environments. This will require the generation of large training datasets and mechanisms to ensure physical consistency and generalization beyond synthetic training scenarios. Success-

fully integrating machine learning with advanced forward modelling could ultimately provide faster, more flexible inversion tools capable of handling realistic geological complexity.

BIBLIOGRAPHY

Blanchy, G., McLachlan, P., Mary, B., Censini, M., Boaga, J., & Cassiani, G. (2024). Comparison of multi-coil and multi-frequency frequency domain electromagnetic induction instruments [Publisher: Frontiers]. *Frontiers in Soil Science*, *4*. https://doi.org/10.3389/fsoil.2024.1239497

ACKNOWLEDGEMENTS

This dissertation was carried out within the *WarmingUP Innovation Plan* project (grant number TEUE819001), funded by the Rijksdienst voor Ondernemend Nederland (RVO). The project aims to build a solid knowledge base for sustainable, collective heating systems, making them reliable, environmentally responsible, and affordable.

Although this thesis presents the results of my PhD research, it reflects only one part of the long journey toward completing my doctorate. Without the help and support of many friends, colleagues, mentors, and family members, reaching this milestone would not have been possible.

First and foremost, I would like to express my heartfelt gratitude to my supervisors.

To **Evert Slob**, thank you for your unwavering support throughout the entire doctoral process. I have learned so much from you over these years, and I truly enjoyed your guidance. Thank you for your advice on research, professional development, and life beyond academia; for your encouragement throughout the project; and for helping me maintain the motivation needed to bring this work to completion. I deeply admire your natural leadership, and I hope others will have the privilege of learning so much from you in the future.

I am also grateful to **Dieter Werthmüller** for your continuous support in developing this project. Your meticulous attention to detail and creative perspective greatly strengthened this work. Thank you for sharing your knowledge of electromagnetics and coding. I am happy for everything you have achieved so far in your academic career, and I wish you continued success and exciting discoveries in the geosciences.

My sincere thanks also go to **Guy Drijkoningen**, whose guidance, especially during our annual meetings, provided direction and purpose throughout the development of this dissertation. I truly appreciate your advice and your insightful perspective on decision-making and motivation. Thank you as well for your attention and support. I wish you continued joy and success in research and supervision.

I would also like to thank **Valentina Socco** for inviting me to collaborate at Politecnico di Torino. Although the stay was short, your input was valuable and greatly appreciated. My thanks as well to **Karim Karimpour** for his support and motivation during my first year.

My research was carried out within the **Applied Geophysics and Petrophysics (AGP)** section at TU Delft. I would like to thank all the professors, postdocs, students, and staff in the section, many of you contributed in different ways. A special highlight for me was the collaboration with the field technicians, without whom this work would not have been possible: **Jens van den Berg**, **Roland Klasen**, and **Jelle Kampf**. My sincere thanks also to **Paula Rulff** for creating the EM meetings, which provided a space for sharing our work and fostering collaboration in the EM discipline. These meetings motivated me greatly during my final year.

My time at the university was made so enjoyable thanks to the friends and colleagues in the AGP and AG groups. I want to especially thank **Liliana** and **Zhenja**, whose coffee breaks always gave me a smile. To my colleagues on the **DOGS board—Aukje, David, Entela, Eddy, and Sverre**—thank you for the cool moments and inviting me to collaborate. To **Mahmoud, Camille, Andrea, Azin, and Parvin**, who began their PhDs in the same year, thank you for sharing the ups and downs of this journey. And to my colleagues and friends **Aleks, Amin, Aydin, Billy, Boris, Cocho, Ellie, Faezeh, Fan, Hamed, Ilshat, Jasper(s), Jesse, Jingming, Johno, Marat, Menno, Milad, Nazife, Samantha, Selvi, Sepideh, Shihao, and Valeria**, thank you for the good times and sharing your company with me.

I am also grateful to the wonderful people who made my life in the Netherlands much brighter: **Florencia, Christian, Nilgun, Rutger, Renzo, Jonas, and Diana**. From home and from other parts of the world, I received the support of dear friends—**Claudia, Jose, Daniela, Isabella, Clara, Alberto, Anibal and Rafa**. My infinite thanks for your care, encouragement, and true friendship.

Finally, to my family, whose support has been priceless. My endless thanks to **Rigo** for his immense support, encouragement, and faith even from the moment that we talked about moving to The Netherlands. Your love has been the engine through this entire journey. I want to thank my closest family—**Mami, Tia Charo, and Carlos**—for your infinite love and unwavering support. This accomplishment is for you. To all the people who helped me in one way or another, I thank you from the bottom of my heart.

LIST OF SYMBOLS AND ABBREVIATIONS

SYMBOLS

Boldface type indicates vector quantities.

Symbol	Description	Units
$\mathbf{E}$	Electric field strength	V/m
$\mathbf{B}$	Magnetic flux density	T
$\mathbf{H}$	Magnetic field strength	A/m
$\mathbf{J}_e$	Electric current density	A/m^2
$\mathbf{J}_m$	Magnetic current density	V/m^2
$\mathbf{D}$	Electric displacement	C/m^2
I	Electric current	A
t	Time	s
ω	Angular frequency	rad/s
f	Frequency	s^{-1}
ϵ	Dielectric constant	F/m
μ	Magnetic permeability	H/m
φ	Phase	
σ	Electrical conductivity	S/m
ΔV	Voltage	V
R	Resistance	ohm
L	Inductance	H
$\mathbf{H}^{\mathrm{p}}$	Primary magnetic field	A/m
$\mathbf{H}^{\mathrm{s}}$	Secondary magnetic field	A/m
$\mathbf{P}$	In-phase	-
$\mathbf{Q}$	Quadrature	-
σ_a	Apparent electrical conductivity	S/m
β	Induction number	-
s	Loop - loop separation	m
δ	Skin depth	m
μ_0	Magnetic permeability of free space	H/m
λ	Hankel transform integral parameter	-
J_0	Bessel function of zeroth order	-
J_1	Bessel function of the first order	-
a	Elevation from the surface	m
R_0	Reflection coefficient	-

Z	Mutual impedance ratio	-
h	Thickness of layer	m
RS	Relative sensitivity	-
b	normalized depth	-
γ_n	Vertical wavenumber	m^{-1}
ϵ_0	Vacuum permittivity	$F\,m^{-1}$
$\mathbf{m}$	Model vector	
$\mathbf{m}_0$	Initial model vector	
$\mathbf{d}$	Data vector	
$\mathbf{J}$	Jacobian matrix	
$\mathbf{C}_d$	Data weighting matrix	
$\mathbf{C}_m$	Model weighting matrix	
$\Phi_\mathbf{m}$	Objective function	
$\mathscr{F}(\mathbf{m})$	Forward operator	
α	Regularization term	
ε	Error fraction	
$\mathbf{I}$	Identity matrix	
$\mathbf{N}$	Diagonal matrix of random values	
A	Amplitude	
$\mathscr{D}$	Data set	
$\mathbf{x}$	Tree input	
y	Tree output	
K	Number of tree ensembles	
$\mathscr{L}$	Objective function	

ABREVIATIONS

EMI	Electromagnetic induction
TDEM	Time domain electromagnetic induction
FDEM	Frequency domain electromagnetic induction
VLF	Very low frequency
GPR	Ground penetrating radar
ERT	Electrical resistivity tomography
MT	Magnetotellurics
GPS	Global positioning system
IP	In-phase
Q	Quadrature or Out-of-phase
PWI	Picewise 1D inversion
LCI	Laterally constrained inversion
HCP	Horizontal coplanar
VCP	Vertical coplanar
PRP	Perpendicular
GS	Global Search
GN	Gauss-Newton inversion
RMSE	Root-mean squared error
NRMSE	Normalized root-mean squared error
ML	Machine learning
DT	Decision Trees
XGBoost	Extreme gradient boosting decision tree
GBDT	Gradient boosting decision tree
CART	Classification and regression trees

CURRICULUM VITÆ

Maria Eugenia CARRIZO MASCARELL

20-04-1986 Born in Merida, Venezuela.

EDUCATION

2001-2003 High School
Liceo Experimental Fray Juan Ramos de Lora
Merida, Venezuela

2004-2009 B.Sc. Geological Engineering
Universidad de Los Andes (ULA)
Merida, Venezuela

2018-2020 M.Sc. Applied Geophysics
Delft University of Technology, Delft, The Netherlands
Eidgenössische Technische Hocschule (ETH), Zürich, Switzerland
Rheinisch-Westfälische Technische Hogeschool (RWTH), Aachen, Germany

2020-2025 Ph.D. Applied Geophysics
Delft University of Technology, Delft, The Netherlands

AWARDS

2019 SEG / Total Excellence Scholarship in Geophysics
2011 Fundación Carolina scholarship for postgraduate studies

List of Publications

Journal Papers

2. **M. Carrizo Mascarell, D. Werthmüller, E. Slob**, *Impact of non-1D Earth on FDEM measurements and the performance of PWI and LCI Inversions*, Journal of Applied Geophysics **2026**, 106130 (247)

1. **M. Carrizo Mascarell, D. Werthmüller, E. Slob**, *Estimation of electrical conductivity models using multi-coil rigid-boom electromagnetic induction measurements*, Computers & Geosciences **2024**, 105732 (193).

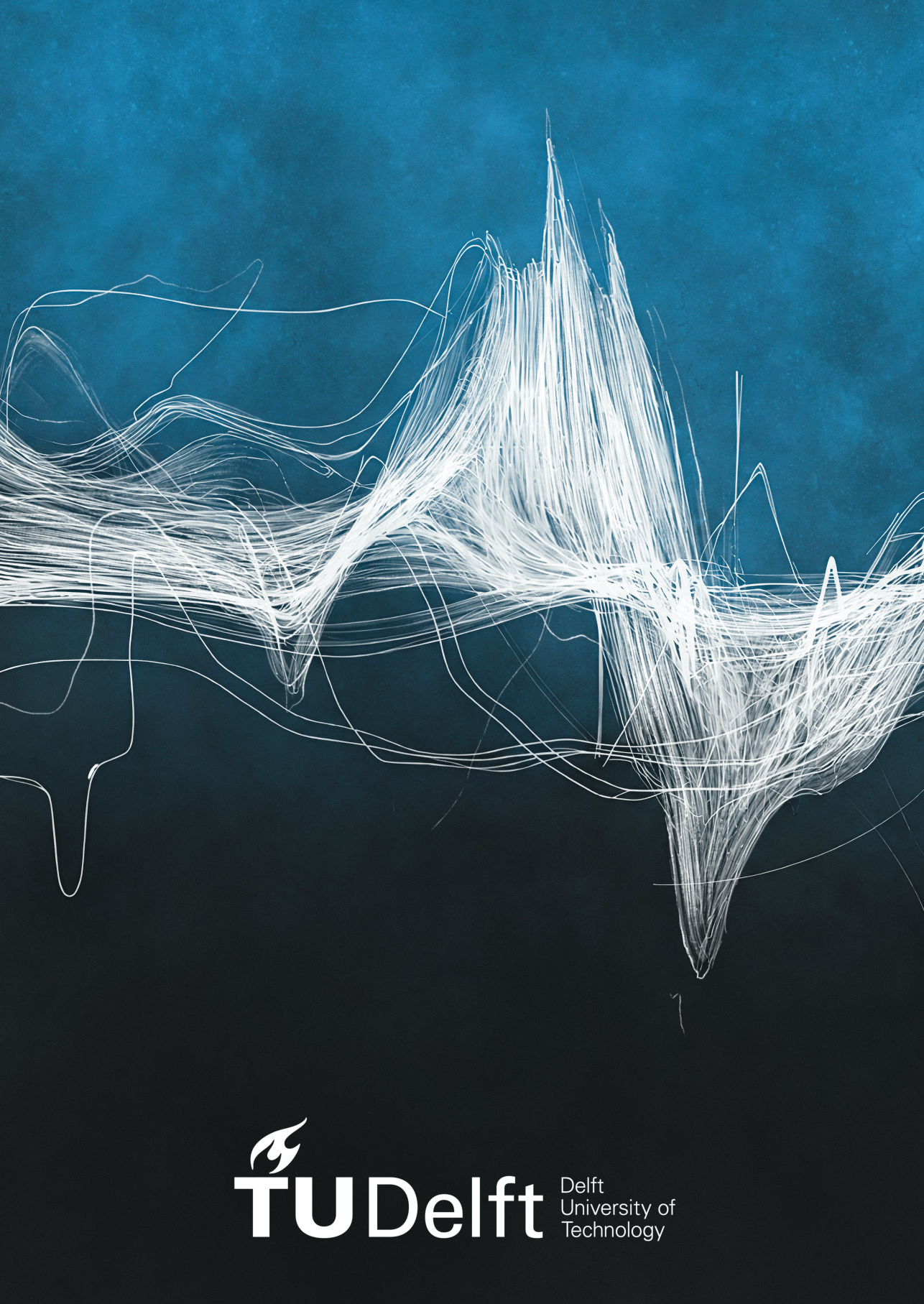
Conference Papers

4. **M. Carrizo Mascarell, F. Riakhi, E. Slob, D. Werthmüller and B. Van Breukelen** *Integrating electromagnetic induction measurements and electrical resistivity tomography to monitor rainwater lenses in Dutch polders*, NSG 2024 30th European Meeting of Environmental and Engineering Geophysics, **2024**, 1-5 (2023)

3. **M. Carrizo Mascarell, D. Werthmüller, E. Slob**, *Global search inversion for electromagnetic induction data using layered models*, NSG2023 29th European Meeting of Environmental and Engineering Geophysics **2023**, 1-5 (2023).

2. **M. Carrizo Mascarell, D. Rovetta, D. Colombo and E. Turkoglu**, *Moment Tensor Prediction from Borehole Microseismic Data with Machine Learning*, 82nd EAGE Annual Conference & Exhibition **2021**, 1-5 (2021).

1. **M. La Cruz, V. Sifontes, I. Rivas, M. Carrizo Mascarell**, *Workflow for an improved seismic acoustic characterization of reservoirs*, SPE WVPS 3er South American Oil and Gas Congress **SPE-WVS-480** (2015).



TU Delft
Delft University of Technology